

ELECTROANALYSIS OF ORGANO-CHALCOGENIC PEROVSKITE NANOMATERIALS



by

Moleko Samuel Mkehlane

BSc Honours Chemistry

A mini-thesis submitted in partial fulfilment of the requirement for the degree of

Magister Scientiae in Nanoscience

In the

**Faculty of Science, University of the Western Cape,
Bellville, Cape Town, South Africa**

Supervisor: Prof Emmanuel Iwuoha

February, 2017

Abstract

Organometallic halide perovskite solar cells have developed as one of the most promising contenders for the production of solar cells. The generic perovskite (PS) structure ABX_3 allows manufacturing a broad range of PS materials by simple modification of building blocks A, B, and X (A = organic group, B = metal, and X = halide). The preparation of a series of solution-processed solar cells based on methylammonium (MA) lead halide derivatives, $CH_3NH_3PbX_3$ (X=Cl, Br, and I) has been reported. These solar cells showed tunable optical properties depending on the nature and ratio of the halides employed. The photovoltaic performance of perovskite solar cells is dependent on the absorption of the light spectrum. The photovoltaic performance can be improved by widening the light absorption towards the near infrared spectrum. A panchromatic material that absorbs all the light from the ultra-visible to near infrared of the solar spectrum is an ideal photoactive layer. The optimal bandgap for single junction solar cells is known to be 1.1 and 1.4 eV. However, the bandgaps of methylammonium lead trihalide perovskites are beyond this range, and this inspired the realization of the lower bandgap perovskites. A maximum theoretical efficiency for optimum performance in a heterojunction device is over 30%, feasible by harvesting the ultraviolet to near infrared photons up to 1.1 eV, and the current organolead halide perovskites materials do not meet these standards. In this study, the least electronegative chalcogenide anions; S (2.58) and Se (2.55), were exploited to narrow the bandgap of the triiodide perovskite $CH_3NH_3PbI_3$ material. New mixed ions perovskites (organo-chalcogenic perovskites); $CH_3NH_3PbI_2S$ and $CH_3NH_3PbI_2Se$, were prepared and characterized. Polycrystalline $CH_3NH_3PbI_3$ particles with particle size of 129.7 nm and hexagonal morphology were confirmed by HR-TEM-EDS technique. The successful incorporation of the chalcogenide anions into the triiodide perovskite structure was confirmed by cyclic voltammetry (CV) scans at cathodic peaks 0.20V and 0.068V for S^{2-} and Se^{2-} , respectively. The electronic properties of all the materials were probed by Ultraviolet-visible (UV-vis) spectroscopy and photoluminescence (PL) spectroscopy. The incorporation of chalcogenide anions into the structure of the triiodide perovskite material resulted in the narrowing of the optical bandgap from 3.40 eV ($CH_3NH_3PbI_3$) to 2.7 eV for materials doped with S ($CH_3NH_3I_2S$), and from 3.40 eV to 2.30 eV for materials doped with Se ($CH_3NH_3PbI_2Se$), respectively, following the anticipated trend $E_g (CH_3NH_3PbI_3) > E_g (CH_3NH_3PbI_2S) > E_g$

($\text{CH}_3\text{NH}_3\text{PbI}_2\text{Se}$). However, the obtained bandgap 3.40 eV for $\text{CH}_3\text{NH}_3\text{PbI}_3$ is bigger than the one reported in literature 1.57 eV for $\text{CH}_3\text{NH}_3\text{PbI}_3$ due to the fact that in this project the UV-vis and PL measurements were carried out with perovskite solution (perovskite precursor) and not with annealed perovskite thin films (polycrystalline perovskite crystals). Nevertheless, spectroscopy studies (UV-vis and PL) in this project demonstrated that S and Se are potential candidates for bandgap narrowing of the current triiodide perovskite $\text{CH}_3\text{NH}_3\text{PbI}_3$ material for application in single-junction solar cells. Electrochemistry studies were also conducted to probe the electronic properties of perovskites under investigation. The incorporation of chalcogenide anions (S and Se) into the structure of triiodide perovskites resulted with an expected decrease in the energy of HOMOs from 3.89 eV ($\text{CH}_3\text{NH}_3\text{PbI}_3$) to 3.68 eV for S doped perovskite ($\text{CH}_3\text{NH}_3\text{PbI}_2\text{S}$) and from 3.6 eV to 3.56 eV for Se doped perovskite ($\text{CH}_3\text{NH}_3\text{PbI}_2\text{Se}$) due to the less electronegativity of chalcogenide anions. Again, an expected increase in energy of the LUMOs was also observed from 4.75 eV ($\text{CH}_3\text{NH}_3\text{PbI}_3$) to 4.96 eV for S doped perovskite ($\text{CH}_3\text{NH}_3\text{PbI}_2\text{S}$) and from 4.75 eV to 5.08 eV for Se doped perovskite ($\text{CH}_3\text{NH}_3\text{PbI}_2\text{Se}$) due to less electronegativity of the chalcogenide anions. The electrochemical bandgaps obtained were lesser than the optical bandgaps and this could be attributed to fast electrochemical reactions which causes the peaks to shift to less extreme potentials. A decrease in the energy of the HOMOs (valence band) implied that lesser energy will be required to knock out the electrons from the valence band to the conduction band (LUMOs) to create photocurrent/electrical current, making organo-chalcogenic perovskites potential candidates for solar cell application.

Declaration

I hereby declare that the matter embodied in this study “*Electroanalysis of organo-chalcogenic perovskite nanomaterials*” is the results of all investigations carried out by me under the supervision of Prof Emmanuel Iwuoha, in the Chemistry Department at University of the Western Cape, South Africa, and that it has not been submitted elsewhere for the award of any degree or diploma. In keeping with the general practice in reporting scientific observations, due acknowledgement has been made whenever the work described is based on the findings of other investigators.

Moleko Samuel Mkehlane

February, 2017

Signed.....



Dedication

This work is dedicated to my family; *Mamokgothunyana Merriam Kopamotse (mother)*, *Tlhoriso Joel Mkehlane (father)*, *Nthabiseng Evelyn Mkehlane (sister)*, *Moratehi Petrus Mkehlane (brother)* and *Realeboga Mkehlane (niece)* for their moral support, love, prayers and all they have provided for me to achieve this milestone.



UNIVERSITY *of the*
WESTERN CAPE

Acknowledgements

First and foremost I would like to thank the Almighty God of Mount-Zion for giving me the strength and wisdom to complete this project. Lord I thank you; I could not have made it on my own.

I would like to express my sincere gratitude to my supervisor *Prof Emmanuel Iwuoha* for the opportunity he has granted me to pursue my life goals and make my dreams come true. I would like to thank him for his guidance, encouragement and support throughout the study. Thank you very much.

I would like to thank my mentor *Dr Miliua Masikini* for his support, guidance, immeasurable help and significant inputs during difficult times. This project couldn't have been a success without you. Thank you very much.

Special thanks to everyone in the Sensor Lab family for making Sensor Lab a pleasant environment for learning. It was fun and inspiring working with you guys. God bless each and every one of you who was willing to help.

I am grateful for the financial support from National Nanosciences Postgraduate Teaching and Training Platform (NNPTT).

I would like to extend my sincere gratitude to my family, my mother (*Mamokgothunyana Merriam Kopamotse*), my father (*Tlhoriso Joel Mkehlane*), my little sister (*Nthabiseng Evelyn Mkehlane*), my older brother (*Moratehi Petrus Mkehlane*) and my niece (*Realeboga Mkehlane*), for their support, understanding, patience, prayers, encouragements, and care when I needed them most. Thank you very much and may the Almighty God of Mount-Zion continue to bless you abundantly in every aspect of your lives and keep you safe at all times.

Academic Outputs

Conference attended:

- Moleko Samuel Mkehlane and Emmanuel Iwuoha, Electroanalysis of Chalcogenic Perovskite nanomaterials, BALEWARE 2016 Conference on Sustainable Energy and Clean Water (11th – 13th December 2016) that took place at The Nelson Mandela African Institution of Science and Technology (NMAIST) in Arusha, Tanzania. Poster Presentation.



Table of Contents

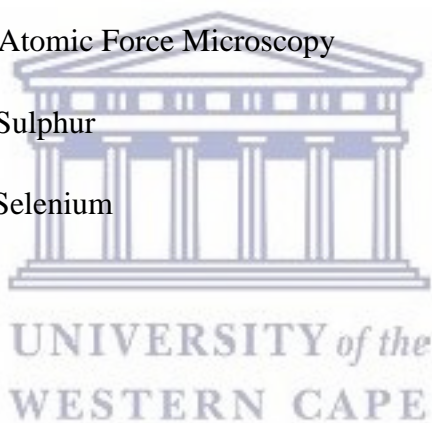
Title page	i
Abstract	ii
Declaration	iv
Dedication	v
Acknowledgements	vi
Academic Outputs	vii
Table of Contents	viii
Acronyms and Abbreviations	xi
Keywords	xii
List of Figures	xiii
List of Tables	xvii
	
CHAPTER 1	1
1.1. BACKGROUND ANMOTIVATION.....	1
1.1.1. Introduction.....	1
1.1.2. Significance of Perovskites.....	3
1.2. PROBLEM STATEMENT.....	5
1.3. MOTIVATION/RATIONALE.....	6
1.4. AIM AND OBJECTIVES.....	7
1.5. LAYOUT OF THE THESIS.....	8
BIBLIOGRAPHY.....	9

CHAPTER 2	15
2. BANDGAP ENGINEERING OF ORGANOMETALLIC HALIDE PEROVSKITES FOR SINGLE-JUNCTION SOLAR CELLS.....	15
2.1. INTRODUCTION.....	15
2.2. INTRINSIC PROPERTIES OF ORGANOMETALLIC HALIDE PEROVSKITES.....	17
2.2.1. Crystal structure of organometallic halide perovskites.....	17
2.2.2. Electronic structure.....	19
2.3. PHOTOPHYSICAL MECHANISMS IN CH ₃ NH ₃ PbI ₃ THIN FILMS.....	20
2.3.1. Morphology and luminescent properties of organometallic halide perovskite thin films.....	22
2.4. PREPARATION METHODS OF ORGANOMETALLIC HALIDE PEROVSKITE THIN FILMS.....	27
2.5. BAND GAP ENGINEERING.....	27
2.5.1. Organic Cation (A) modification.....	29
2.5.2. Metal (B) modification.....	37
2.5.3. Halide (X) mixing.....	45
2.5.4. Band gap engineering of lead halide perovskites using a sequential deposition process for planar heterojunction solar cells.....	47
2.5.5. Bandgap engineering by heterovalent doping of perovskite materials with Bi ³⁺ , Au ³⁺ , and In ³⁺	49
2.5.6. Bandgap engineering by incorporation of chalcogenide anions (S & Se) into standard perovskite structure to prepare new mixed ions perovskites CH ₃ NH ₃ PbI ₂ S and CH ₃ NH ₃ PbI ₂ Se for application in single-junction solar cells.....	51
BIBLIOGRAPHY.....	53
CHAPTER 3	81
3.1. INTRODUCTION.....	81
3.2. REAGENTS.....	81

3.3. EXPERIMENTAL AND PROCEDURE.....	82
3.3.1. Synthesis of standard perovskite nanomaterials.....	82
3.3.2. Incorporation of chalcogenide anions to form new mixed ions perovskites, $\text{CH}_3\text{NH}_3\text{PbI}_2\text{S}$ and $\text{CH}_3\text{NH}_3\text{PbI}_2\text{Se}$	83
3.4. MATERIALS CHARACTERIZATION TECHNIQUES AND INSTRUMENTATION.....	84
3.4.1. High-Resolution Transmission Electron Microscopy (HR-TEM).....	84
3.4.2. Energy Dispersive x-ray Spectroscopy.....	85
3.4.3. Ultra-violet Visible (UV-vis) spectroscopy.....	86
3.4.4. Photoluminescence (PL) spectroscopy.....	88
3.4.5. Electrochemical characterization by Cyclic Voltammetry (CV).....	89
BIBLIOGRAPHY.....	93
CHAPTER 4	95
4.1. INTRODUCTION.....	95
4.2. EXPERIMENTAL RESULTS AND DISCUSSION.....	95
4.2.1. High-Resolution Transmission Electron Microscopy (HR-TEM).....	95
4.2.2. Energy Dispersive x-ray spectroscopy (EDS).....	98
4.2.3. Spectroscopic studies by Ultra-violet (UV-vis) spectroscopy.....	99
4.2.4. Spectroscopic studies by Photoluminescence (PL) spectroscopy.....	104
4.2.5. Electrochemical characterization by Cyclic Voltammetry (CV).....	106
BIBLIOGRAPHY.....	112
CHAPTER 5	114
5.1. CONCLUSIVE SUMMARY.....	114
5.2. RECOMMENDATIONS AND SUGGESTED FUTURE WORK.....	116

Acronyms and abbreviations

UV-vis	Ultraviolet-visible
PL	Photoluminescence
CV	Cyclic Voltammetry
HR-TEM	High-Resolution Tunnelling Electron Microscopy
HR-SEM	High-Resolution Scanning Electron Microscopy
CCD	Charge Coupled Device
XRD	X-ray Diffraction
AFM	Atomic Force Microscopy
S	Sulphur
Se	Selenium



Keywords

Triiodide perovskite

Organo-chalcogenic perovskites

Chalcogenides

Electronegativity

Optical bandgap

Electrochemical bandgap

Highest Occupied Molecular Orbital

Lowest Occupied Molecular Orbital

Electron-hole pairs

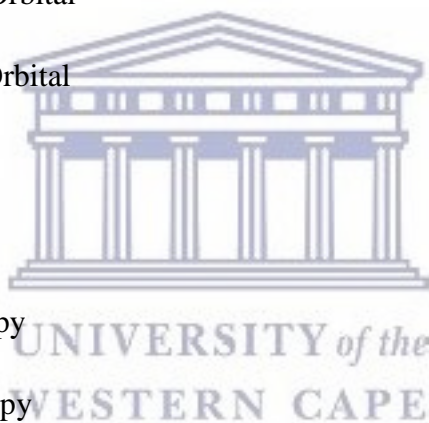
Single-junction solar cells

Ultra-violet visible spectroscopy

Photoluminescence spectroscopy

Cyclic voltammetry

Thin films



List of Figures

- Figure 2.1* Unit cell of basic ABX_3 perovskite structure. The BX_6 corner-sharing octahedral are evidenced. Adapted with permission from Ref. [67]..... 17
- Figure 2.2* Bonding diagram of (a) $[PbI_6]^{4-}$ cluster (0 – D), (b) $CH_3NH_3PbI_3$ – (3 – D) and (b) $(CH_4H_9NH_3)_2PbI_4$ (2 – D) at the top of the valence band and at the bottom of the conduction band. Adapted with permission from Ref. [81]..... 20
- Figure 2.3* (a – d) Top view SEM images of $MAPbI_3$ formed using (a) $[MAI] = 0.063M$, $T = 25^\circ C$; (b) $[MAI] = 0.045 M$, $T = 25^\circ C$; (c) $[MAI] = 0.031 M$, $T = 25^\circ C$; (d) $[MAI] = 0.045 M$, $T = 70^\circ C$. Scale bars are $2 \mu m$. (e) (top) Spectral positions of the UV-vis absorption band edge and cw.PL peak position and (bottom) PL lifetime as functions of the crystallite size. (f) Representative τ_r PL dynamics for three different $MAPbI_3$ crystal sizes and PL dynamics of Cl doped $MAPbI_3$ spin coated on a glass substrate. The pump wavelength was 700 nm, and the initial excitation density was $\sim 4 \times 10^{16} cm^{-3}$. Adapted with permission from Ref. [118]..... 24
- Figure 2.4* (a) Normalized PL quantum yield (calculated as the ratio of the integrated PL spectrum to the incident power) for the sample shown in Figure 2.3a. (b) PL lifetime as a function of the excitation density for $MAPbI_3$ samples with small (black circles) and large (red squares) crystallites. Dashed lines represents the curves obtained fitting the data to eq 1. The inset shows the PL lifetime as a function of initial excitation density for Meso- $MAPbI_3$ at room temperature (black triangles), 220 K (red circles), and 150 K (green squares). The error bars refer to the 95% confidence intervals of the fitted parameter values. Adapted with permission from Ref.[118]..... 26
- Figure 2.5* UV-Vis spectra for the $APbI_3$ perovskites formed, where A is caesium (Cs), methylammonium (MA) or formamidinium (FA). Adapted with permission from Ref. [150]..... 31
- Figure 2.6* Tunability of the $FAPbI_yBr_{3-y}$ perovskite system. (a) UV-Vis absorbance of the $FAPbI_yBr_{3-y}$ perovskites with varying y , measured in an integrating sphere. (b) Corresponding

steady-state photoluminescence spectra for the same films. Adapted with permission from Ref. [150]..... 32

Figure 2.7 (a) Light harvesting spectra of the different perovskite films recorded in integrating sphere. Note the 20 nm red shift of the absorbance onset for $(\text{CH}_3\text{NH}_3)_{0.8}\text{-(HNCHNH}_3)_{0.2}\text{PbI}_3$ as compared to $(\text{CH}_3\text{NH}_3)\text{PbI}_3$. As the formamidinium concentration was increased, the absorbance of the film decreased, while no change in the bandgap was discernible. (b) Normalized emission of $(\text{CH}_3\text{NH}_3)_x\text{-(HNCHNH}_3)_{1-x}\text{PbI}_3$ ($x = 0, 0.2, 0.4, 0.6, 0.8, 1$). The emission is shifted further into the red and broadened as x is decreased. Adapted with permission from Ref. [173]..... 35

Figure 2.8 (a) An absorption spectra of the $\text{CH}_3\text{NH}_3\text{SnI}_{3-x}\text{Br}_x$ ($x = 0, 1, 2, 3$) perovskites. (b) Schematic energy level diagram of $\text{CH}_3\text{NH}_3\text{SnI}_{3-x}\text{Br}_x$, with TiO_2 and spiro-OMeTAD HTM. The Valence band maxima E_{CB} of the methylammonium tin halides were extracted from UPS measurements under high vacuum. Adapted with permission from Ref. [185]..... 40

Figure 2.9 Absorption spectra and schematic energy level diagram of the $\text{CH}_3\text{NH}_3\text{Sn}_{1-x}\text{Pb}_x\text{I}_3$ solid solution perovskites. (a) Electronic absorption spectra and (b) schematic energy level diagram of the $\text{CH}_3\text{NH}_3\text{Sn}_{1-x}\text{Pb}_x\text{I}_3$ solid solution perovskites. The valence band maximum (E_{CB}) of the hybrid methylammonium tin/lead triiodide were extracted from UPS measurements under high vacuum. Adapted with permission from Ref. [204]..... 44

Figure 2.10 (a) Picture of $\text{MAPb}(\text{Br}_x\text{I}_{1-x})_{3-y}\text{Cl}_y$, ($0 \leq x \leq 1$) devices with different Br/I molar ratios grown on mesoporous TiO_2 substrates after sample characterization. (Yellow parts in some samples indicate degradation). (b) Absorption spectra of the samples (absorption tail observed at long wavelengths is due to the mesoporous layer light scattering). (c) The energy bandgap extracted from the absorption measurements depending on the percentage of the Br. Adapted with permission from Ref. [221]..... 46

Figure 2.11 UV-Vis absorption spectra of the mixed halide lead perovskite $(\text{MAPb}(\text{I}_{1-x}\text{Br}_x)_3$ ($0 \leq x \leq 1$) films formed via a sequential deposition process. The numbers 1 – 7 correspond to the mixed lead halide perovskite films with different halide (iodide/bromide) compositions. The inset shows the photograph of mixed lead halide nanocomposite perovskite films on FTO substrates. Adapted with permission from Ref. [223]..... 48

Figure 2.12 (a) Steady-state absorption spectra of MAPbBr_3 crystals with various Bi%. Inset: corresponding Tauc plots. (b) Bandgap narrowing as a function of Bi concentration in

the crystal. (c) Bandgap alignment of MAPbBr ₃ crystals with various Bi%. Adapted with permission from Ref. [224].....	50
<i>Figure 3.1</i> Schematic outline of TEM. Adapted with permission from Ref. [6].....	85
<i>Figure 3.2</i> Schematic for the UV-visible spectrophotometer. Adapted with permission from Ref. [9].....	87
<i>Figure 3.3</i> Outline presentation of photoluminescence spectroscopy. Adapted with permission from Ref. [12].....	89
<i>Figure 3.4</i> Diagram showing energy level and light harvesting of an organic solar cell. Adapted with permission from Ref. [13].....	91
<i>Figure 3.5</i> Diagram showing energy level and light harvesting of organic solar cell. Adapted with permission from Ref. [19].....	92
<i>Figure 4.1</i> TEM micrograph of standard perovskite CH ₃ NH ₃ PbI ₃ nanoparticles.....	96
<i>Figure 4.2</i> Particle size distribution of standard perovskite CH ₃ NH ₃ PbI ₃ material.....	96
<i>Figure 4.3</i> TEM micrograph of standard perovskite CH ₃ NH ₃ PbI ₃ at higher magnifications (a) – (b) and (c) is the selected area electron diffraction (SAED) patterns.....	98
<i>Figure 4.4</i> EDS spectrum for the elemental composition of the standard perovskite CH ₃ NH ₃ PbI ₃ materials on the Cu grid.....	99
<i>Figure 4.5</i> Absorption spectrum and optical bandgap of P3OT. Adapted with permission from Ref [2].....	100
<i>Figure 4.6</i> UV-vis spectra of standard perovskite CH ₃ NH ₃ PbI ₃ nanomaterials.....	100
<i>Figure 4.7</i> UV-vis spectra of mixed perovskite CH ₃ NH ₃ PbI ₂ S nanomaterials.....	101
<i>Figure 4.8</i> UV-vis spectra of mixed ions perovskite CH ₃ NH ₃ PbI ₂ Se nanomaterials....	102
<i>Figure 4.9</i> PL spectrum of standard perovskite CH ₃ NH ₃ PbI ₃	104
<i>Figure 4.10</i> PL spectrum of mixed ions perovskite CH ₃ NH ₃ PbI ₂ S.....	104
<i>Figure 4.11</i> PL spectrum of the mixed ions perovskite CH ₃ NH ₃ PbI ₂ Se.....	105
<i>Figure 4.12</i> CV of Bare GCE in 0.1 M LiClO ₄ at 50 mv/s.....	106

<i>Figure 4.13</i> CV of standard perovskite $\text{CH}_3\text{NH}_3\text{PbI}_3$ in 0.1M LiClO_4 at 50 mv/s.....	107
<i>Figure 4.14</i> CV of mixed ions perovskite $\text{CH}_3\text{NH}_3\text{PbI}_2\text{S}$ in 0.1M LiClO_4 at 50 mv/s...	108
<i>Figure 4.15</i> CV of mixed ions perovskite $\text{CH}_3\text{NH}_3\text{PbI}_2\text{Se}$ in 0.1M LiClO_4 at 50 mv/s...	109



List of Tables

Table 2.1 Estimation of the cation Radii in ABX_3 ($B = Pb^{2+}$ and $X = Cl^-, Br^-,$ or I^-).....	18
Table 2.2 Exciton binding energies E_b of the 3-D $CH_3NH_3PbI_3$ and $CH_3NH_3PbI_{3-x}Cl_x$ perovskites and selected low-dimension perovskites.....	22
Table 4.1 Calculated optical bandgaps of the perovskite materials.....	102
Table 4.2 Photoluminescence emissions of organolead perovskite materials.....	105
Table 4.3 Calculated electrochemical bandgaps of the perovskite compounds.....	110



UNIVERSITY *of the*
WESTERN CAPE

CHAPTER 1

Introduction

1.1 BACKGROUND AND MOTIVATION

1.1.1 Introduction

Energy from the sun, an endless producer of photons with a wide range of wavelengths, remains to be a potential source of green (clean) energy. Conversion of energy via photovoltaic (PV) process is considered to be the ideal process that satisfies the requirement for the demand of clean energy [1]. It has been estimated by the International Energy Agency's technology that by 2050, about ~11% of all global electricity will be produced by photovoltaic technology, avoiding 2.3 gigatonnes of CO₂ emissions per annum [2]. By taking these forecasts into consideration, photovoltaic devices have gained significant attention from research communities in the past decades. Researchers believe that solar cells, which are the basic building block of photovoltaics, are approaching to revolutionize the photovoltaic technology by providing sustainable and efficient energy through profitable methods.

There are many ways to harness the solar energy. PV segment that converts solar energy directly into electricity could be one of the examples, and a solar thermal collector that converts solar energy directly into heat, such as for domestic hot water and or room heating [3]. Thus, finding ways to realize PV as reliable, cheap, and durable avenues for power generation is of research interest to the research community. The 14th element on the periodic table known as Silicon is vital for PV materials in today's world. Nonetheless, a need for novel materials and methodologies that provides improved outputs and efficiencies are still in demand [4].

Silicon solar cell, classified as first generation of the solar cells, was discovered back in 1953 by Gerald Pearson, Daryl Chapin, and Calvin Fuller at AT&T Bell Labs [5]. At present, they range on the efficiency chart at 25% [6]. The application of polycrystalline silicon, thin films, and compound semiconductors emerged in the age of second-generation solar cells,

which penetrated the PV market in 1981 [7]. At present, second-generation solar cells are at the highest range of efficiency chart, at 45% [8]. Organic solar cells paved a way for a third trend of PV technology, in early 2000, which offers advantages of cost-effectiveness, flexibility, and ease of fabrication. Although solar cells based on silicon continue to lead over thin-film technologies and are soaring owing to impressive efficiencies and enhanced lifetimes, however, researchers still need to unpack the organic prospects of solar cells. Consequently, discovering flexible, cheaper, mass producible and lightweight organic solar cells has been a high demand on scientists in the past decade. Developing PV cells from materials that can be processed as easily as plastics is one of the possible alternatives to solve this problem. In supplement of this demand, Dr. Alan Heeger was awarded a Nobel Prize in Chemistry in recognition of his work on conducting polymers which has conclusively paved a new era in the arena of organic electronics, organic photovoltaics (OPVs), and organic/flexible displays [9]. This has resultantly led to the flexible third-generation solar cells, which are organic, dye sensitized, and polymer.

Plastic based solar cells or organic solar cells (OSC) are developing multidisciplinary field of research that comprises theoretical, experimental, and design challenges dealing with carbon based materials and other organic compounds [10]. It is a product of polymer solar cells that integrates a conductive organic polymer for light absorption, exciton dissociation, and charge transport to generate electricity [11]. Single conducting polymer based OPVs can attain efficiencies $>7\%$ [12] and still exhibiting the potential to improve this. They differ from the well-known silicon and other inorganic material based solar cells because they are inexpensive and can be fabricated through low-cost solution processing techniques, such as spin-coating, brush painting, and sprays coating [4]. Desired film thickness of a few hundred nanometers and efficiencies of 4 to 5% are attained from these solution-processing techniques. OSCs has wide multi-layered architectures which help in executing the photon trapping, electrons and holes generation processes, and transportation of charges to the corresponding cathodes and anodes. The use of tandem architectures was later reported as an effective way to improve polymer solar cell efficiency. A broader part of solar radiation spectrum is exploited and the thermalization loss of photon energy is minimized with this method. Power conversion efficiencies of $>10\%$ in tandem solar cells was reported by Yang Yang [13]. The highest efficiency of 12 (Ref. 14) and 10% [15], have recently been claimed by Heliatek and Mitsubishi Chemicals. Dye-sensitized solar cells (DSSCs), also known as another kind of device, have gained unparalleled growth in recent years owing to their ease of

fabrication and higher tunable optical properties. A record efficiency of 13% has recently been attained with DSSC with porphyrin sensitizers without sacrificing stability [16]. The commercialization of OSCs and DSSCs has been hindered by key drawbacks which include efficiency, durability, and stability.

A new solar cell material known as perovskites emerged in 2009 to revolutionize photovoltaics and currently exhibits outstanding potential and prospects with power conversion efficiency of 19.7% [17] in the laboratory. Solar cells based on perovskites have been estimated to offer sustainable and efficient power through profitable means and methods. The frontrunners in the efforts to double the efficiency of these materials in less than a year [18-21] includes several groups such as Henry Snaith from Oxford University, Andrew Rappe at University of Pennsylvania, Sang Hyeok Park at South Korean Institute KRICT, Michael Gratzel from EPFL, and Yang Yang from UCLA. The perovskite devices are at maximum optimization point and are anticipated to achieve power conversion efficiency of 50% in the near future [22]. Perovskites devices are also known for their panchromatic absorption property, wide direct bandgaps with higher carrier charge transportations [23], and profitable means of fabrication.

1.1.2 Significance of perovskites

In 1839 a German mineralogist known as Gustav Rose discovered calcium titanate (CaTiO_3), a mineral which was named after a Russian mineralogist, Lew A. Perovski. Moreover, all compounds with the same stoichiometry as ABX_3 and with the same nomenclature to CaTiO_3 are identified as perovskites. Muller and Roy unambiguously clarified the indistinctness of terminology of the structural family and mineral [24]. The indistinctness was addressed by suggesting that the original mineral composition would be placed in square brackets. Hence, $[\text{CaTiO}_3]$ stands for the structure of perovskite but not the chemical composition CaTiO_3 .

The building blocks A, B, and X in the crystal structure of perovskite are arranged in an octahedral symmetry and are usually represented as larger rare earth metal cation, a smaller metal cation, and anions (O^{2-} , Cl^- , Br^- , I^- , or in few instances S^{2-}), respectively. For an ideal (cubic) perovskite structure, the large A cations are in 12 coordinates and the smaller B cations occupy octahedral holes which are formed by large X anions. Different perovskite materials such as CaTiO_3 , MgSiO_3 , SrFeO_3 , BaTiO_3 , LiNbO_3 , SrZrO_3 , and nonoxide KMgF_3

exist. These perovskites can produce an incredibly wide array of phases with a multitude of functionalities that include dielectric [25,26], ferroelectric [27-30], magnetoresistive [28], thermoelectric [31], electro-optic [32], semiconducting [33], conducting [28,34], and superconducting [29,35]. By cutting 3-D perovskite into one layer thick slice along $\langle 100 \rangle$ [36] direction, a two-dimensional layered organic-inorganic perovskite structure was derived from the three-dimensional (3-D) ABX_3 structure. The replacement of an inorganic A cation in a basic cubic perovskite structure by a suitable organic cation is known from the first principle study to provide a material of a superior scope with a wide-ranging selection of properties [37]. The structure-property relationship in organic-inorganic hybrid perovskite materials was explored by David B. Mitzi by replacing A with a cationic organic molecule, B with an inorganic post-transition metal, and X with halides, such as methylammonium tin iodide ($CH_3NH_3SnI_3$) and methylammonium lead iodide ($CH_3NH_3PbI_3$) [29]. These materials, organometallic halide perovskite materials, are brought about for diverse thin-film devices, such as solar cells [38,39], thin-film transistors [40], and light-emitting diodes [38,40]. Perovskites of nomenclature with a methylammonium ($CH_3NH_3^+$) organic cation and inorganic metal halide octahedra's (SnI_2 , PbI_2) form hybrid perovskites with changing physical, optical, mechanical, and electrical properties. Strong intermolecular hydrogen bonds between the amino and halide group ions exist in the organometallic perovskite, while the weak Vander Waals exists amid the organic cations. The best metal cations for the functioning of organic-inorganic framework are the divalent transition metal ions (such as Cu^{2+} , Ni^{2+} , Co^{2+} , Fe^{2+} , Mn^{2+} , Pd^{2+} , Sn^{2+} , Pb^{2+} , etc.). The transition metals belonging to group 14 (including Sn^{2+} and Pb^{2+}) attracted more interest owing to their excellent optoelectronic properties and potential for low-temperature device fabrication [20,34,42]. Sn^{2+} and Pb^{2+} are the most primarily used metal cations with melting points of 505 and 600 K, respectively. These cations (Sn^{2+} and Pb^{2+}) are usually unreactive, stable at room temperature, and abundant in the Earth's crust. The absorption of perovskite structures is improved by employment of the least electronegative anions for strong absorptions over wide bandgaps. Moreover, a bandgap can be decreased by lowering the Pauling electronegativity between the metal cation and halide anion. The tuning capabilities of optical absorptions can be enhanced by the replacement of pure halides by mixed halides with changing ratios in the organometallic halide perovskites [36]. Thus, the organometallic halide structures such $AB(Br_xI_{1-x})_3Cl_y$ have developed.

1.2 PROBLEM STATEMENT

The shortage of energy and pollution of the environment are the two primary challenges faced by the society today. Sunlight has turned out to be the most reliable and sustainable supply of green (clean) energy and this makes the exploitation of solar energy an ideal approach in addressing both energy and environment problems, in comparison to the traditional fossil energy such as coal, oil, and natural gas. A photovoltaic device (solar cell) is a device that converts solar irradiation directly into electricity by exploiting the photovoltaic effect exhibited by semiconductors. Solar cell technology signifies a great potential but still remains to be a big challenge in research to harvest solar energy. In spite of the significant performance attained by traditional photovoltaics such as silicon solar cell with power conversion efficiency up to 25% [42], CdTe solar cell with power conversion efficiency of 19.6% [43], and CIGS solar cell with power conversion efficiency of 20.3% [44], their applications are restricted by their high cost fabrication processes, or by the scarcity of their resources in nature, and even by some toxic elements. Therefore, new solar cells consisting of materials that are environmentally friendly and earth abundant, with profitable processing are presently of great interest in both research and industry [45].

Hybrid organometallic halide perovskite solar cells have emerged as remarkably efficient and cheap technology [46]. Methylammonium lead trihalide perovskite material has been utilized in solar cells and has attained power conversion efficiency up to over 15% [47,48]. This semiconductor material is solution-processable and has a bandgap of approximately 1.55 eV. The photovoltaic performance of perovskite solar cells is dependent on the absorption of the light spectrum. The current organolead halide perovskite materials shows a poor absorption at 780 nm attributed to its limited bandgap of 1.5 eV [47,49,50,51]. The photovoltaic performance can be improved by widening the light absorption to the near infrared spectrum. An ideal photo active layer material should be panchromatic, meaning it should absorb all the light from ultra violet visible to near infrared spectrum. A maximum theoretical efficiency for optimum performance in a heterojunction device is over 30%, feasible by harvesting the ultraviolet to near infrared photons up to 1.1 eV [52], and the current perovskite materials do not meet these standards.

1.3 MOTIVATION OR RATIONALE

Solar energy (solar power) is known as the world's richest energy supply. About 1.5×10^{18} kW h of solar energy from sunlight is consumed every year. The known reserves of oil, coal, and natural gas are worth 1.75×10^{15} kW h, 1.4×10^{15} kW h, 5.5×10^{15} kW h, respectively, in contrast to solar power. Therefore, sunlight provides more than a hundred times the energy of the world's known fossil fuel reserves ever year. An indefinite energy supply would be generated by harnessing solar power [53]. However, the challenge has always been converting the solar energy. Solar cells (photovoltaic cells) are the potential candidates for the convention of sunlight directly into electricity in an efficient and profitable way. Reduction of cost for solar energy is essential for solar energy to become competitive candidates with fossil fuels and to penetrate and occupy a significant share of electricity market. This goal can be reached either by the reduction of cost of solar cells or by improving their power conversion efficiencies.

Silicon solar cells with power conversion efficiencies close to 20% are currently dominating the photovoltaic market. Organic photovoltaics (OPVs) dye sensitized solar cells (DSCs) and quantum dots solar cells (QDSCs) which are known as alternative "third generation" technologies are fabricated via solution based processes such as blade coating, screen printing and spraying. These photovoltaics carry the potential for inexpensive solar power while allowing the use of alternative substrates. However, the power conversion efficiencies of these solar cells still lag behind traditional solar cells. The efficiency of the solar cells is a critical factor on which the levelized cost of energy depends on, which allows for the comparison of a number of electricity generation resources [54]. Therefore the cost of solar cells primarily depends on the PCE.

Hybrid organometallic halide perovskite solar cells have been the most remarkable development in the arena of photovoltaics and are best potential candidates to satisfy the demands for high efficiencies while allowing for inexpensive solution based fabrication. The PCEs of stable solid state solar cells based on $\text{CH}_3\text{NH}_3\text{PbI}_3$ perovskite have already surpassed 15% transcending every other solution-processed solar cells technology. It has been shown by early pioneering work [55,56] in the field of organometallic halides that this group of materials can behave as low dimensional electronic systems with tunable properties, which allows for the development of new perovskite solar cell materials in addition to $\text{CH}_3\text{NH}_3\text{PbI}_3$.

1.4 AIM AND OBJECTIVES OF THE STUDY

The chief aim of this study is to redshift the absorption onset of the current triiodide perovskite $\text{CH}_3\text{NH}_3\text{PbI}_3$ nanomaterials beyond 780 nm (narrow bandgap below 1.5 eV). This will be done by incorporating chalcogenide anions (S & Se) into the structure of the triiodide perovskite to synthesise new perovskite nanomaterials with mixed ions (organo-chalcogenic perovskites); $\text{CH}_3\text{NH}_3\text{PbI}_2\text{S}$ & $\text{CH}_3\text{NH}_3\text{PbI}_2\text{Se}$. The aim of the study will be achieved by the following objectives (in sequence).

1. Synthesise the triiodide perovskite $\text{CH}_3\text{NH}_3\text{PbI}_3$ nanomaterials.
2. Incorporate the bivalent chalcogenide ions (S^{2-} , Se^{2-}) into the structure of the triiodide perovskite $\text{CH}_3\text{NH}_3\text{PbI}_3$ to prepare new mixed-ions (organo-chalcogenic) perovskites $\text{CH}_3\text{NH}_3\text{PbI}_2\text{S}$ and $\text{CH}_3\text{NH}_3\text{PbI}_2\text{Se}$ nanomaterials.
3. Interrogate the microscopic properties of the triiodide perovskite $\text{CH}_3\text{NH}_3\text{PbI}_3$ nanomaterials by High-Resolution Transmission Electron Spectroscopy (HR-TEM), determine the particle size and confirm the elemental composition by Energy Dispersive x-ray Spectroscopy (EDS).
4. Determine the optical bandgaps of all perovskites nanomaterials by Ultraviolet-visible (UV-vis) spectroscopy and Photoluminescence (PL) spectroscopy.
5. Determine the electrochemical behaviour and electrochemical bandgaps of all perovskite nanomaterials by Cyclic Voltammetry (CV).

1.5 LAYOUT OF THE THESIS

This section gives a layout of the five chapters discussed in this mini-thesis.

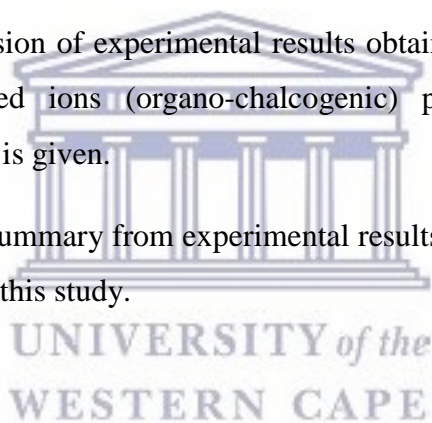
Chapter 1. In this chapter, the background on the photovoltaic (solar cell) technologies including the significance of perovskites, problem statement, motivation, aims & objectives of the study are discussed.

Chapter 2. A detailed literature review of organometallic halide perovskite materials focusing on their intrinsic properties, fundamental photophysics and preparation methods is discussed. The work done on bandgap engineering (modulation) of organometallic perovskite materials for application in single-junction solar cells is also discussed.

Chapter 3. This chapter gives the experimental details (including reagents and procedure followed) and a discussion of the characterization techniques used in this study.

Chapter 4. A detailed discussion of experimental results obtained from triiodide perovskite $\text{CH}_3\text{NH}_3\text{PbI}_3$ and new mixed ions (organo-chalcogenic) perovskite $\text{CH}_3\text{NH}_3\text{PbI}_2\text{S}$ & $\text{CH}_3\text{NH}_3\text{PbI}_2\text{Se}$ nanomaterials is given.

Chapter 5. Gives a conclusive summary from experimental results as well as recommendations and suggested future work for this study.



BIBLIOGRAPHY

- [1] S. Kazim et al., Perovskite as light harvester: a game changer in photovoltaics, *Angewandte Chemie International Edition in English*. **53**(11), 2812–2824 (2014).
- [2] P. Frankl, Technology roadmap: solar photovoltaic energy, 11 May 2010, <http://www.iea.org/publications/freepublications/publication/technology-roadmap-solar-photovoltaicenergy---foldout.html> (18 November 2016).
- [3] S. A. Kalogirou, Solar thermal collectors and applications, *Progress in Energy and Combustion Science*. **30**(3), 231–295 (2004).
- [4] A. K. Chilvery et al., A versatile technique for the fabrication of PEDOT: PSS films for organic solar cells, *Energy Science and Technology*. **4**(2), 6–11 (2012).
- [5] S.-S. Sun and N. S. Sariciftci, *Organic Photovoltaics*, p. 640, CRC Press, T&F Group, London (2005).
- [6] NREL Cell Efficiencies, *efficiency_chart*, (2012).
- [7] M. A. Green, Crystalline and thin-film silicon solar cells: state of the art and future potential, *Solar Energy*. **74**(3), 181–192 (2003).
- [8] M. A. Green et al., Solar cell efficiency tables, *Progress in Photovoltaics: Research and Applications*. **20**, 12–20(2012).
- [9] H. Shirakawa et al., Synthesis of electrically conducting organic polymers: halogen derivatives of polyacetylene, (CH)_x, *Journal of the Chemical Society, Chemical Communications*. **16**, 578 (1977).
- [10] M. Pagliaro, R. Ciriminna, and G. Palmisano, Flexible solar cells, *Sustainable Chemistry*. **1**(11), 880–891 (2008).

- [11] A. C. Mayer et al., Polymer-based solar cells, *Materials Today*. **10**(11), 28–33 (2007).
- [12] G. Li, R. Zhu, and Y. Yang, Polymer solar cells, *Nature Photonics* **6**, 153–161 (2012).
- [13] J. You et al., A polymer tandem solar cell with 10.6% power conversion efficiency, *Nature Communications*. **4**, 1446 (2013).
- [14] Heliatek, Heliatek press release, 2013, <http://www.heliatek.com/?lang=en> (18 November 2016).
- [15] M. C. Scharber and N. S. Sariciftci, Efficiency of bulk-heterojunction organic solar cells, *Progress in Polymer Science*. **38**(12), 1929–1940 (2013).
- [16] P. Simon et al., Dye-sensitized solar cells with 13% efficiency achieved through the molecular engineering of porphyrin sensitizers, *Nature Chemistry*. **6**, 242–247 (2014).
- [17] H. Zhou et al., Interface engineering of highly efficient perovskite solar cells, *Science*. **345**(6196), 542–546 (2014).
- [18] M. Liu, M. B. Johnston, and H. J. Snaith, Efficient planar heterojunction perovskite solar cells by vapour deposition, *Nature*. **501**(7467), 395–398 (2013).
- [19] I. Grinberg et al., Perovskite oxides for visible-light-absorbing ferroelectric and photovoltaic materials, *Nature*. **503**(7477), 509–517 (2013).
- [20] P. Gao, M. Grätzel, and M. K. Nazeeruddin, Organohalide lead perovskites for photovoltaic applications, *Energy and Environmental Science*. **7**(8), 2448–2463 (2014).
- [21] J. You et al., Perovskite solar cells with high efficiency and flexibility, *ACS Nano* **8**(2), 1674–1680 (2014).
- [22] B. Bulkin, Perovskites: the future of solar power?, in *Guardian*, p. 1, <http://www.theguardian.com/sustainable-business/perovskites-future-solar-power> (18 November 2014).

- [23] H. J. Snaith, Perovskites: the emergence of a new era for low-cost, high-efficiency solar cells, *The Journal of Physical Chemistry Letters*. **4**, 3623–3630 (2013).
- [24] O. Muller and R. Roy, The major ternary structural families, in *Cryst. Chem. Non-Metallic Mater.*, Springer-Verlag, Berlin, Heidelberg (1974).
- [25] E. J. Juarez-Perez et al., Photoinduced giant dielectric constant in lead halide perovskite solar cells, *The Journal of Physical Chemistry Letters*. **5**(13), 2390–2394 (2014).
- [26] A. K. Batra et al., Simulation of energy harvesting from roads via pyroelectricity, *Journal of Photonics for Energy*. **1**(1), 014001 (2011).
- [27] A. A. Bokov and Z. G. Ye, Recent progress in relaxor ferroelectrics with perovskite structure, *Journal of Materials Science*. **41**(1), 31–52 (2006).
- [28] M. A. Loi and J. C. Hummelen, Hybrid solar cells: perovskites under the Sun, *Nature Materials*. **12**(12), 1087–1089 (2013).
- [29] D. B. Mitzi, Synthesis, structure, and properties of organic-inorganic perovskites and related materials, in *Progress in Inorganic Chemistry*, K. D. Karlin, Ed., p. 121, John Wiley & Sons, West Sussex, England, New York (1999).
- [30] J. M. Frost et al., Atomistic origins of high-performance in hybrid halide perovskite solar cells, *Nano Letters*. **14**(5), 2584–2590 (2014).
- [31] Y. Takahashi et al., Charge transport in tin-iodide perovskite: origin of high conductivity, *Dalton Transactions*. **40**(20), 5563–5568 (2011).
- [32] A. Bhalla, R. Guo, and R. Roy, The perovskite structure—a review of its role in ceramic science and technology, *Materials Research Innovations*. **4**(1), 3–26 (2000).
- [33] C. C. Stoumpos, C. D. Malliakas, and M. G. Kanatzidis, Semiconducting tin and lead iodide perovskites with organic cations: phase transitions, high mobilities, and near-infrared photoluminescent properties, *Inorganic Chemistry*. **52**(15), 9019–9038 (2013).

[34] D. B. Mitzi et al., Conducting tin halides with a layered organic-based perovskite structure, *Nature*. **369**, 467–469 (1994).

[35] H.-S. Kim, S. H. Im, and N.-G. Park, Organolead halide perovskite: new horizons in solar cell research, *The Journal of Physical Chemistry C*. **118**(11), 5615–5625 (2014).

[36] J. L. Knutson, J. D. Martin, and D. B. Mitzi, Tuning the band gap in hybrid tin iodide perovskite semiconductors using structural templating, *Inorganic Chemistry*. **44**(13), 4699–4705 (2005).

[37] R. S. Roth, Classification of perovskite and other AB₃ type compounds, *Journal of Research of the National Bureau of Standards*. (1934). **58**(2), 75–88 (1957).

[38] D. B. Mitzi, Templating and structural engineering in organic-inorganic perovskites, *Journal of the Chemical Society, Dalton Transactions*. **1**(1), 1–12 (2001).

[39] A. Kojima et al., Organometal halide perovskites as visible-light sensitizers for photovoltaic cells, *Journal of the American Chemistry Society*. **131**(17), 6050–6051 (2009).

[40] D. B. Mitzi, K. Chondroudis, and C. R. Kagan, Organic-inorganic electronics, *IBM Journal of Research and Development*. **45**(1), 29–45 (2001).

[41] I. B. Koutselas, L. Ducasse, and G. C. Papavassiliou, Electronic properties of three- and low-dimensional semiconducting materials with Pb halide and Sn halide units, *Journal of Physics: Condensed Matter*. **8**, 1217–1227 (1996).

[42] M. A. Green, The path to 25 % silicon solar cell efficiency: history of silicon cell evolution, *Progress in Photovoltaics*. **17**, 183–189 (2009).

[43] M. A. Green, K. Emery, Y. Hishikawa et al., Solar cell efficiency tables (version 42). *Progress in Photovoltaics: Research and Applications*. **21**, 827–837 (2013).

[44] P. Jackson, D. Hariskos, E. Lotter et al., New world record efficiency for Cu(In, Ga)Se₂ thin-film solar cells beyond 20 %, *Progress in Photovoltaics*. **19**, 894–897 (2013).

[45] N. S. Lewis, Toward cost-effective solar energy use, *Science*. **315**, 798–801 (2007).

[46] H. J. Snaith, Perovskites: The Emergence of a New Era for Low-Cost, High-Efficiency solar cells, *The Journal of Physical Chemistry Letters*. **4**, 3623–3630 (2013).

[47] M. Liu, M. B. Johnston and H. J. Snaith, Efficient planar heterojunction perovskite solar cells by vapour deposition, *Nature*. **501**, 395–398 (2013).

[48] J. Burschka, N. Pellet, S.-J. Moon, R. Humphry-Baker, P. Gao, M. K. Nazeeruddin and M. Grätzel, Sequential deposition as a route to high-performance perovskite-sensitized solar cells, *Nature*. **499**, 316–319 (2013).

[46] H. J. Snaith, Perovskites: The Emergence of a New Era for Low-Cost, High-Efficiency solar cells, *The Journal of Physical Chemistry*. **4**, 3623–3630 (2013).

[47] M. Liu, M. B. Johnston and H. J. Snaith, Efficient planar heterojunction perovskite solar cells by vapour deposition, *Nature*. **501**, 395–398 (2013).

[48] J. Burschka, N. Pellet, S.-J. Moon, R. Humphry-Baker, P. Gao, M. K. Nazeeruddin and M. Grätzel, Sequential deposition as a route to high-performance perovskite-sensitized solar cells, *Nature*. **499**, 316–319 (2013).

[49] H. S. Kim, C. R. Lee, J. H. Im, K. B. Lee, T. Moehl, A. Marchioro, S. J. Moon, R. Humphry-Baker, J. H. Yum, J. E. Moser, M. Grätzel, N. G. Park, Lead iodide perovskite sensitized all-solid-state submicron thin film mesoscopic solar cells with efficiency exceeding 9%, *Scientific Reports*. **2**, 591 (2012).

[50] J. Burschka, N. Pellet, S. J. Moon, R. Humphry-Baker, P. Gao, M. K. Nazeeruddin and M. Grätzel, Sequential deposition as a route to high-performance perovskite-sensitized solar cells, *Nature*. **499**, 316 (2013).

[51] M. M. Lee, J. Teuscher, T. Miyasaka, T. N. Murakami and H. J. Snaith, Efficient hybrid solar cells based on meso-superstructured organometal halide perovskites, *Science*, **338**, 643 (2012).

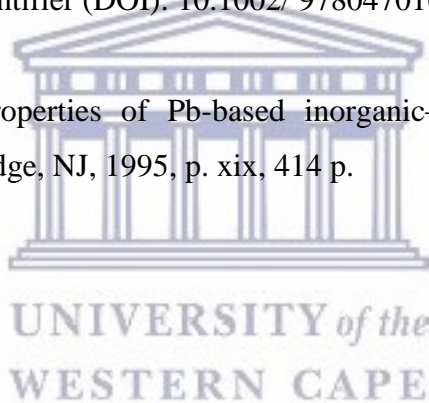
[52] W. Shockley and H.J. Queisser, Detailed Balance Limit of Efficiency of pn junction solar cells. *Journal of Applied Physics*. **32**, 510 (1961).

[53] J. Nelson, *The Physics of Solar Cells*, Imperial College Press, (2003).

[54] X. Wang, J. Byrne, L. Kurdgelashvili and A. Barnett, *Wiley Interdisciplinary Reviews: Energy and Environment*. **1**, 132–151 (2012).

[55] D. B. Mitzi, in *Progress in Inorganic Chemistry*, John Wiley & Sons Incorporated. p. 1–121 (2007), Digital Object Identifier (DOI): 10.1002/9780470166499.chapter 1.

[56] T. Ishihara, *Optical Properties of Pb-based inorganic–organic perovskites*, World Scientific, Singapore, River Edge, NJ, 1995, p. xix, 414 p.



CHAPTER 2

Literature review

2. BAND-GAP ENGINEERING OF ORGANOMETALLIC HALIDE PEROVSKITES FOR SINGLE-JUNCTION SOLAR CELLS

2.1 INTRODUCTION

Solar energy is the most abundant energy source and an alternative for noncarbon-based energy sources i.e fossil fuels and coal, and can be utilised as a solution to serious issues of global warming that results from the evolution of CO₂. Solar cell (photovoltaic cell) technology is effectively used in harvesting sunlight to convert solar energy directly to electrical energy, posing a very interesting photovoltaic research challenge. Single crystalline materials such as silicon and semiconductor compounds have been reported to achieve a good efficiency [1]; however, they suffer from low cost effectiveness and also have the longest payback time of commercial photovoltaic technologies. Although a class of thin film devices based on amorphous silicon, Cu(In, Ga)Se_{2-x}S_x, or CdTe, has emerged to advance their progress in terms of cost per unit area [2-4], the manufacturing processes of inorganic thin-film solar cells requires high temperature and high vacuum-based techniques [5].

In 1991, a breakthrough of dye sensitized solar cells (DSSCs) emerged for potential application in inexpensive, clean, and renewable energy sources [6]. With continuous research efforts in DSSCs, photoelectric conversion efficiencies exceeding 12% were achieved by employing 10 μm mesoporous TiO₂ film sensitized with organic dye and cobalt redox electrolyte [7]. Driven by the demand to simplify the solar cell production and increase the open-circuit voltage and stability of solar cells, solid-state DSSCs have also been investigated, where the liquid electrolyte was replaced by solid hole-transporting materials [e.g., 2,2',7,7'-tetrakis-(N,N-di-p-methoxyphenyl-amine)-9,9'-spirobifluorene (spiro-MeOTAD), poly(3-hexythiophene) (P3HT), polypyrrole, and polyaniline) [8-12]. However,

high carrier recombination rate at various device interfaces has been a setback in solid-state DSSCs [13], resulting in lower photoelectric conversion efficiencies of solid state DSSCs.

Recently, high efficiency solar cells based on organometallic halide perovskite materials ABX_3 ($A = CH_3NH_3$, $B = Pb, Sn$, and $X = F, Cl, Br$) have been extensively explored due to their attractive light-harvesting characteristics [14-44]. These materials have a direct bandgap and exhibit excellent photovoltaic properties, with high extinction coefficient [45,46], carrier mobility [47,48], wide absorption spectrum range and convenient synthesis methods. Therefore they appeal as potential candidates for application in the optoelectronic field. Significant increase in power conversion efficiency of perovskite solar cells from 7.2% to 15.9% was observed in a short period, from August 2012 to December 2013. The resulting high power conversion efficiency was attributed to comparable optical absorption length and charge-carrier diffusion lengths, surpassing the traditional constraints of solution-processed semiconductors [14-44, 49], and resultantly transcending the performance of most other thin film solar cell technologies that have been explored.

The photovoltaic performance of perovskite solar cells is dependent on the absorption of the light spectrum. The current organolead triiodide perovskite $CH_3NH_3PbI_3$ material shows a poor absorption at 780 nm attributed to its limited bandgap of 1.5 eV [50,51,52,53]. The photovoltaic performance can be improved by widening the light absorption to the near infrared spectrum. An ideal photo active layer material should be panchromatic, meaning it should absorb all the light from ultra violet visible to near infrared spectrum. A maximum theoretical efficiency for optimum performance in a heterojunction device is over 30%, feasible by harvesting the ultraviolet to near infrared photons up to 1.1 eV [54]. Nevertheless, preparation of stable low-bandgap perovskites for sunlight conversion to electricity still poses a major challenge [55-57]. Meanwhile, the preparation of lead-free perovskite solar cells maintaining the output performance is still under investigation since the toxicity of Pb element prevents the practical application of these materials in the photovoltaic industry. This chapter reviews the work done on tuning the bandgap (bandgap engineering) of organometallic halide perovskite photovoltaics as a means of improving the device performance of single junction solar cells. A new class of anions known as chalcogenide anions (S & Se) for synthesis of mixed ions (organo-chalcogenic) perovskites is introduced in the end (section 2.5.6) and suggested for better band-gap engineering of organometallic halide perovskite photovoltaics to improve the photovoltaic performance.

2.2 INTRINSIC PROPERTIES OF ORGANOMETALLIC HALIDE PEROVSKITES

2.2.1 Crystal Structure of Organometallic halide perovskites

The composition of the organometallic halide perovskite obeys the general formula ABX_3 for the perovskite structure (see Figure 2.1); where A is the organic group cation (e.g. $A = CH_3NH_3$, $NH_2CH=NH_2$), B is the metal cation (e.g. $B = Sn$, Pb , Ge , Cu), and X is the halide anion (e.g. $X = Cl^-$, Br^- , or I^-). These materials form the PbX_6^{4-} octahedral where the halogen anion X^- is situated in the corner around the $CH_3NH_3^+$. The octahedra PbX_6^{4-} form an extended three-dimensional (3D) network by all-corner-connected type. The organic cation $CH_3NH_3^+$ fills up the hole among the octahedral structures and balances the net charge of the network as a whole [58-60]. The compounds $CH_3NH_3BX_3$ ($B = Sn$, Pb and $X = Cl^-$, Br^- , and I^-) and $NH_2CH=NH_2BX_3$ ($B = Pb$ and $X = I^-$) have been successfully prepared [61-66].

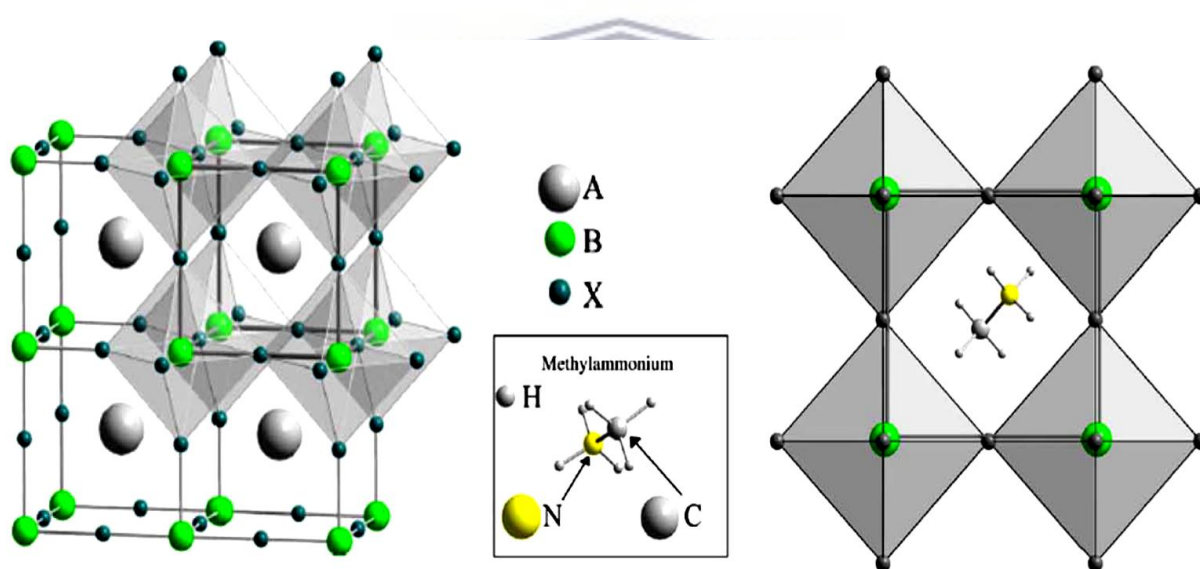


Figure 2.1: Unit cell of basic ABX_3 perovskite structure. The BX_6 corner-sharing octahedral are evidenced. Adapted with permission from Ref. [67].

The formation of perovskite is estimated by Goldschmidt tolerance factor (t), $t = (r_A + r_X) / [\sqrt{2}(r_B + r_X)]$ [68], where r_A , r_B , and r_X are the ionic radii of the ions in the A, B, and X positions of the basic building blocks structure. Generally, the accepted perovskite structure formation and stabilization is in the range $0.76 < t < 1.13$ [69]. It has been debated that the perovskite structures are not stable even in the most preferred range $0.8 < t < 0.9$ [70], indicating that perovskites formability and stability can not only be determined

by the tolerance factor. The octahedral factor (μ), $\mu = r_A/r_X$ [71], thus serves as an additional determining factor for the formation and stabilization of the perovskite structure. For alkali metal halide perovskites, the formability and stability is determined by $t - \mu$ mapping, where the stability is achieved in the ranges $0.813 < t < 1.107$ and the octahedral factor $0.442 < \mu < 0.895$ [71]. Table 1 gives the estimated effective ionic radii r_A in APbX_3 perovskite [72-74], where the A cation radii ranges between ~ 160 pm to ~ 250 pm, which corresponds to one or two C-C (150 pm) or C-N (148 pm) bonds. The tolerance factors for $\text{CH}_3\text{NH}_3\text{PbX}_3$ for $X = \text{Cl}, \text{Br},$ and I , are calculated as 0.85, 0.84, and 0.83, respectively, on the radii of $\text{CH}_3\text{NH}_3^+ = 180$ pm [75], $\text{Pb}^{2+} = 119$ pm, $\text{Cl}^- = 181$ pm, $\text{Br}^- = 196$ pm, and $\text{I}^- = 220$ pm. It was found that the most cubic perovskites has a tolerance factor in the range $0.8 < \mu < 0.9$ [76], indicating that the methylammonium lead halide perovskites have a cubic structure.

Table 1. Estimation of the cation Radii in ABX_3 ($B = \text{Pb}^{2+}$ and $X = \text{Cl}^-, \text{Br}^-$, or I^-)

r_B^a (pm)	r_X^a (pm)	r_A^b (pm)	r_A^b (pm)
		$t = 0.8$	$t = 1.0$
Pb^{2+} ($r_B = 119$)	Cl^- ($r_X = 181$)	158.4	243.3
	Br^- ($r_X = 196$)	160.4	249.5
	I^- ($r_X = 220$)	163.5	259.4

^aEffective ionic radii, for 6 coordination number. ^b $r_A = t \times 2^{1/2} (r_A + r_A) - r_A$.

In contrast to oxide perovskites, the organometallic halide perovskites are much scarce and can only be prepared with a specific combination of elements. The reason for the scarcity of these materials is due to the halide anion ($X^- = \text{Br}^-, \text{Cl}^-, \text{I}^-$) differences in comparison to the oxide (O^{2-}) anion:

(i) their negative charge is so small that it can only balance metals in lower oxidation states, and, (ii) their much large ionic radii hampers their incorporation of small metal ions octahedral coordination geometry. Due to these restrictions, the metal anion B is selected from a few set of elements which includes the alkaline earth metals [77], bivalent rare earth metals [78], and the heavier group 14 elements ($\text{Ge}^{2+}, \text{Sn}^{2+}, \text{Pb}^{2+}$). Remarkably, there are no transitions metals that can adopt the halide perovskite structure, with few notable exceptions

[79]. The above considerations apply for the fluorine anion $X = F^-$, because its small size is able to stabilize the perovskite structure for nearly all the bivalent metal ions. There are only three cations that have been reported to stabilize the perovskite structure in heavy halides, $CH_3NH_3^+$ (MA), $HC(NH_2)_2^+$ (FA), and Cs^+ . Amongst these three cations, Cs^+ is the only elemental cation that is large enough to support the perovskite, whereas for the organic cations, it is not only the size that is crucial but also the net positive charge distribution is important.

2.2.2 Electronic Structure

Different methods have been used to study the electronic and band structures of organometallic halide perovskites. The first method can be traced on the studies done by Koutselas et al. [80] whereby the band structure calculations were used by a semi-empirical method based on the Huckel theory and *ab initio* method based on the theory of Hartree-Fock. The second approach can be traced on the studies done by T. Umebayashi et al. [81] whereby ultraviolet photoelectron spectroscopy and first principles density functional theory (DFT) band calculations were utilized to elucidate the band structure of organometallic halide perovskites. The third method was can be traced in studies done by Chang et al. [82] whereby first principles pseudopotential calculations were employed. It was revealed by DFT calculations for the 3-D $CH_3NH_3PbI_3$ crystals that the valence band maxima consists of the Pb 6p – I 5p σ -antibonding and Pb 6p – I 5p π anti-bonding orbitals, as seen on Figure 2.2 [81].

DFT studies of 3-D perovskies began to become intense owing to the attention raised by perovskite solar cells. The band structure for $CH_3NH_3PbX_3$ in cubic phase and the mixed halide $CH_3NH_3PbI_2X$ ($X = Cl, Br$ and I) in tetragonal phase with neighbouring $CH_3NH_3^+$ counterions were calculated by E. Mosconi together with F. De Angelis and their collaborations [83]. The results revealed that the organic component had a slight effect on the bandgap energy, which is largely determined by $[PbI_4]^{6-}$ network. It was further highlighted by the authors that the nearby matching of their bandgaps (calculated without considering spin-orbit coupling (SOC) effect) with the experimental results was likely to be unexpected. These results corroborated the studies done by T. Baikie et al. [84] and Y. Wang et al. [85] (low-temperature orthorhombic phase). J. Even et al. [28] reported the work done

on the SOC effect on the electronic band structure in 3-D perovskites and it was found that the SOC intensely reduces the energy gap which mainly affects the conduction band.

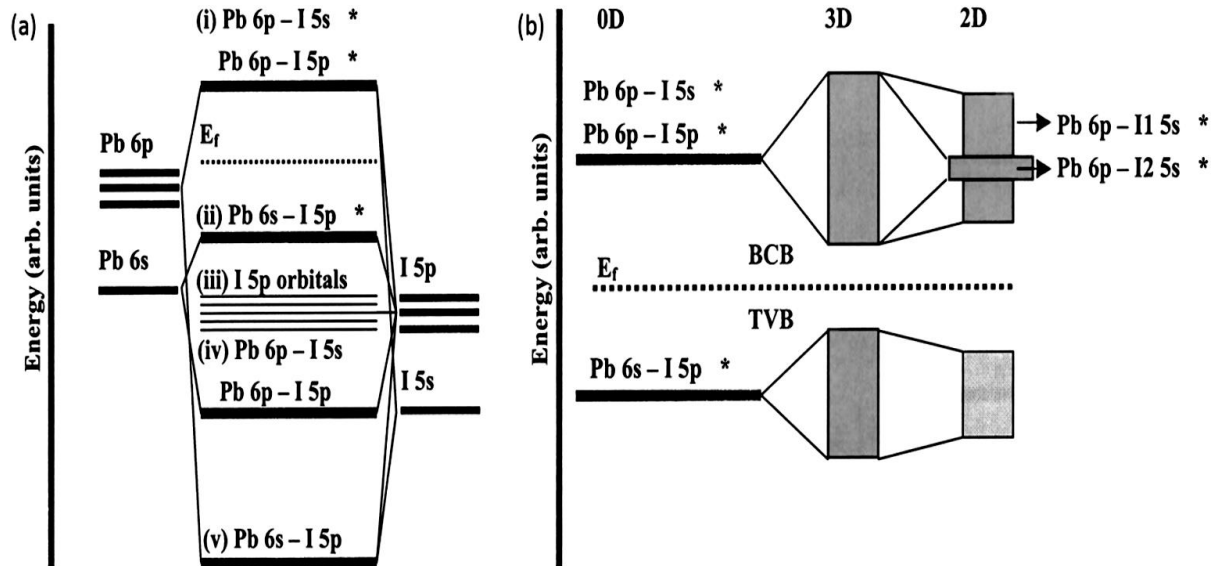
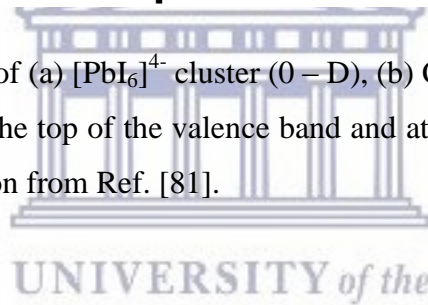


Figure 2.2: Bonding diagram of (a) $[\text{PbI}_6]^{4-}$ cluster (0 – D), (b) $\text{CH}_3\text{NH}_3\text{PbI}_3$ – (3 – D) and (b) $(\text{CH}_4\text{H}_9\text{NH}_3)_2\text{PbI}_4$ (2 – D) at the top of the valence band and at the bottom of the conduction band. Adapted with permission from Ref. [81].



2.3 PHOTOPHYSICAL MECHANISMS IN $\text{CH}_3\text{NH}_3\text{PbI}_3$ THIN FILMS

The photophysics study of organometallic halide perovskites focuses mainly on two properties, which comprises the excitonic properties of layered perovskites such as the optical non-linearity around the excitonic resonances [86] and the exciton-exciton interactions [87]. Exciton and bi-exciton dynamics [88] are investigated using Coherent transient spectroscopy such as wave mixing, while exciton recombination dynamics [84] in 2D perovskites are studied using temperature dependent TRPL spectroscopy. The excited species following photoexcitation could exist as bound electron-hole pairs or as free carriers depending on the exciton binding energy E_b , hence the E_b for $\text{CH}_3\text{NH}_3\text{PbI}_3$ as photovoltaic material has been extensively investigated. The E_b of selected 3-D perovskites with low-dimensional perovskites included for comparison are shown in Table 2. $\text{CH}_3\text{NH}_3\text{PbI}_3$ excitons are expected to be more of the delocalized Wannier-type associated with exciton Bohr radius, $r_B \sim 30 \text{ \AA}$ [80,90]. $\text{CH}_3\text{NH}_3\text{PbBr}_3$ and the mixed halide $\text{CH}_3\text{NH}_3\text{PbI}_{3-x}\text{Cl}_x$ system shows

larger binding energies which are ascribed to more tightly bound nature of the excitons as a result of halogen substitution. For 2-D layered perovskites, in contrast, a Frenkel type for excitons is expected and their larger binding energies are attributed to dielectric modulation between the organic and inorganic layers and the two dimensionality of the inorganic assembly [91]. The exciton binding energies increases in accordance with quantum confinement effects [90] associated with a decreasing dimensionality to 1-D and 0-D.

Electron-hole pairs in perovskites are induced by the absorption of photons. Depending on the exciton binding energy, the carriers that follows could either continue to exist as free carriers or form excitons. The long diffusion lengths in 3-D perovskites rise due to ambiguity of whether these species exist as excitons or free carriers at room temperature. This ambiguity originates from the low exciton binding energies E_b ranging from 19 meV to 50 meV, these values are comparable to room temperature thermal energies of $k_B T \sim 25$ meV. Given the ambiguities and assumptions involved with the determination of the values for E_b based on the approach used (optical absorption [92,93], magneto-absorption [94] and temperature dependent PL [95]), it can be concluded from Table 1 that E_b for $\text{CH}_3\text{NH}_3\text{PbI}_3$ is close (comparable) to the thermal energies of $k_B T \sim 25$ meV at room temperature.

There have be are no reports on studies focusing on the charge dynamics in 3D perovskites until the advent of the 9.7% perovskite solar cells in 2012 [96]. The fundamental photophysical processes that give rise to the high performance of organometallic halide perovskites still lacks a lot despite the soaring progressing in organometallic halide perovskite solar cells.

Table 2. Exciton binding energies E_b of the 3-D $\text{CH}_3\text{NH}_3\text{PbI}_3$ and $\text{CH}_3\text{NH}_3\text{PbI}_{3-x}\text{Cl}_x$ perovskites and selected low-dimension perovskites.

Compound	Dimensionality	E_b (meV)	Method
$\text{CH}_3\text{NH}_3\text{PbI}_3$	3D	30	Optical absorption [80]
		37	Magneto-absorption [97]
		45	Temperature dependent PL [98]
		50	Magneto-absorption [94]
		19 ± 3	Temperature dependent PL [99]
$\text{CH}_3\text{NH}_3\text{PbBr}_3$	3D	76	Magneto-absorption [94]
		150	Optical absorption [80]
$\text{CH}_3\text{NH}_3\text{PbI}_{3-x}\text{Cl}_x$	3D	98	Temperature dependent PL [100]
$(\text{C}_9\text{H}_{19}\text{NH}_3)_2\text{PbI}_4$	2D	≥ 330	Temperature dependent PL [98]
$(\text{NH}_2\text{C}(\text{I})=\text{NH}_2)_3\text{PbI}_5$	1D	≥ 410	Optical absorption [80]
$(\text{CH}_3\text{NH}_3)_4\text{PbI}_6 \cdot 2\text{H}_2\text{O}$	0D	545	Optical Absorption [80]

2.3.1 Morphology and Luminescent properties of Organometallic Halide perovskite thin films

Organometallic halide perovskites have revolutionized the photovoltaic industry, and appealed as new viable materials for light emitting devices, providing easy methods towards solution-processable and tunable electrically pumped lasers [101-103,104]. This has increased an interest in seeking for the insight of the optical properties of these materials. It has been demonstrated by the recent work that the photoluminescence (PL) decay in $\text{CH}_3\text{NH}_3\text{PbI}_3$ (MAPbI_3) can be explained by simple rate equations involving carrier trapping and electron-hole radiative recombination. According to Yamada et al [105], Stranks et al. [106], and Saba et al. [107], the PL dynamics are dependent on nongeminate electron-hole recombination process [108], and possibly on nonradiative de-excitation paths as well. Therefore, a bimolecular intrinsic radiative recombination coefficient ($B_{\text{rad}} = R_{\text{rad}}/n_i^2$, where R_{rad} is the radiative rate and n_i is the intrinsic carrier concentration) and a nonradiative monomolecular trapping rate (A), i.e., $dn/dt = -An - B_{\text{rad}}n^2$ has to be taken into account to satisfactorily model the temporal evolution of the excited carrier population $n(t)$. Charge-

trapping pathways dominates at low excitation densities and results in limited PL quantum efficiency, whereas at high excitation densities the charge-trapping pathways are completely filled resulting in radiative recombination processes yielding high PL efficiency. This explains well the dependence of PL quantum efficiency on excitation density [101,106].

A remarkable long PL lifetime reaching up to hundreds of nanoseconds associated with photocarrier diffusion lengths of micrometers [109] was found for Cl-doped MAPbI₃. The long PL lifetime was attributed to the incorporation of Cl⁻ ions within the perovskite unit cell. Nevertheless, recent studies have indicated the major role played by chlorine-based precursor in the crystallization process of the hybrid perovskite. It was shown that Cl ion cannot be quantitatively determined in the unit cell implying that it is expelled from the flat films during the fabrication process. However, Cl content controls the crystallization dynamics and produces larger crystals with anisotropic shapes [110]. This phenomenon highlights the importance of exploring the relationship between the structural and optoelectronic properties of the self-assembled materials. During the fabrication process, organometallic halide perovskites are usually deposited as polycrystalline thin films with morphologies that depend on the crystallite growth conditions [111,112].

The influence of morphology of the MAPbI₃ thin films, from a molecular to a mesoscopic level, on the luminescent properties was investigated with the samples shown on Figure 2.3a-d. The samples were fabricated using the two-step sequential deposition technique [113,114], resulting with crystallite dimensions ranging from <250 nm to >2 μm. It was observed that as the polycrystallite size grows, the optical absorption edge shifted to longer wavelengths accompanied with PL peak position. The results for time-resolved PL (tr-PL) as a function of crystallite size, showed that, for the smallest crystallite size (<250 nm), a lifetime of 2 ns was obtained, and increased to lifetime greater than 100 ns with largest crystallite size (>1 μm), as shown in Figure 2.3e. The lifetime value for larger crystallites (>100 μm) approached value that have been reported for MAPbI₃ samples doped with Cl [109,115], as shown in Figure 2.3f. These results show that the PL lifetime of MAPbX₃ materials is critically dependent on the specific morphology of the sample and therefore the employed fabrication protocol [109,112,115-117]. It is intuitively concluded that the nonradiative channels are enhanced with the increase in the polycrystallinity. This can be clarified and explained well by specifically excluding any nonradiative bimolecular mechanisms such as surface recombination. The dependence of the normalized PL yield [107] on excitation density is shown on Figure 2.3a for sample with the smallest crystallite size, more likely to have a high

degree of surface defects. An increase in efficiency is observed with an increase in excitation density, therefore rationalizing the major role of radiative recombination in the bimolecular recombination process also in the small crystallites. The density-dependent nonradiative processes become more apparent and dominate at excitation density beyond 10^{17} cm^{-3} , resulting in a decrease in PL yield. This behaviour was modelled by Saba et al. [107] in accordance to Auger-like mechanisms proportional to n^3 . Lower threshold is presented by small crystallites for such nonradiative mechanisms in comparison to larger crystallites and Cl-doped MAPbI₃ [107]. This may be attributed to a high degree of defect densities in smaller crystallites [99].

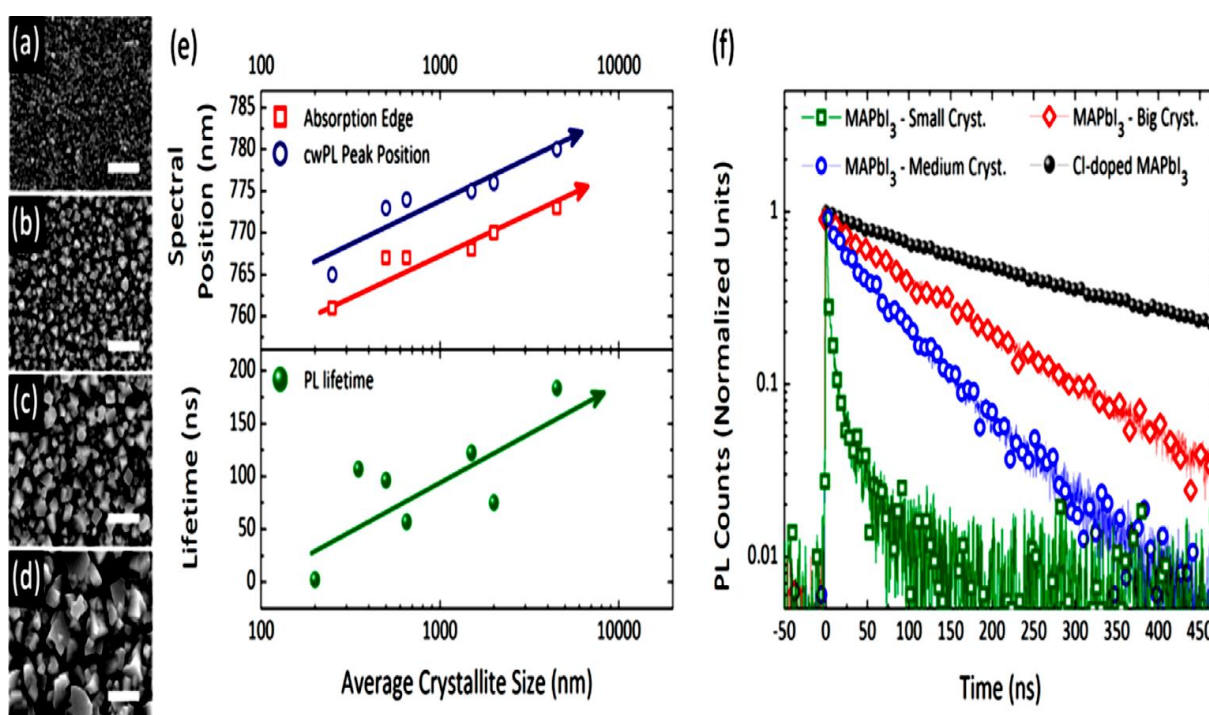


Figure 2.3: (a – d) Top view SEM images of MAPbI₃ formed using (a) [MAI] = 0.063 M, $T = 25^\circ\text{C}$; (b) [MAI] = 0.045 M, $T = 25^\circ\text{C}$; (c) [MAI] = 0.031 M, $T = 25^\circ\text{C}$; (d) [MAI] = 0.045 M, $T = 70^\circ\text{C}$. Scale bars are 2 μm. (e) (top) Spectral positions of the UV-vis absorption band edge and cw.PL peak position and (bottom) PL lifetime as functions of the crystallite size. (f) Representative tr PL dynamics for three different MAPbI₃ crystal sizes and PL dynamics of Cl doped MAPbI₃ spin coated on a glass substrate. The pump wavelength was 700 nm, and the initial excitation density was $\sim 4 \times 10^{16} \text{ cm}^{-3}$. Adapted with permission from Ref. [118].

The dependence of the PL lifetimes on the excitation density is shown Figure 2.4b. Two representative samples studied in Figure 2.4a, MAPbI₃ with <250 nm crystallite and with >1µm crystallite, which correspond to the samples in Figure 2.3 a, d, respectively, were chosen. In this structure, the PL lifetime dependence on the initial excitation density (n_0) can be written as [105,119]

$$\tau_{PL} = (A + B_{rad}n_0)^{-1} \quad (1)$$

The intrinsic bimolecular radiative recombination coefficient of the samples was estimated by fitting equation 1 to the experimental data, for both samples. Larger crystallites were found to exhibit a lower recombination coefficient, $B_{rad} = (0.62 \pm 0.06) \times 10^{-9} s^{-1} cm^3$, respectively to the smaller ones, $B_{rad} = (3.7 \pm 0.2) \times 10^{-9} s^{-1} cm^3$. Indeed larger crystallites resulted in longer PL lifetimes. As the crystallite dimension decreases, it must be noted that the monomolecular trapping rate is slightly affected, decreasing from $1.3 \times 10^7 s^{-1}$ to $0.72 \times 10^7 s^{-1}$. Nevertheless, this rate is very sensitive to the adopted protocol for sample production [105, 119,120]. It may be related with localized defects in the crystals and therefore depends significantly on the imperfect control of the sample fabrication.

The correlation between E_g and B_{rad} is shown by reduction in B_{rad} accompanied by a redshift of the band edge from 1.63 eV for small crystallites to 1.61 eV for larger crystallites as shown in Figure 2.4b. The sample temperature was also lowered and the intensity dependent PL measurements also confirmed this observation. The optical bandgap of the MAPbX₃ was observed to shift to lower energies as a result of lattice stress (Varshni shift [121]) as the temperature of the temperature is lowered. This was observed for MAPbI₃ film deposited by employing the two-step procedure on a 1µm thick Al₂O₃ mesoporous scaffold. The purpose of the scaffold was to confine the crystal structure to a nanoscale smaller than 50 nm [110], permitting the exclusion of excitonic effects even at lower temperatures [122]. A PL lifetime of about 2 ns was observed when the sample was excited with a density similar to the one used to obtain PL decay shown in Figure 2.3f ($\sim 6 \times 10^6 cm^{-3}$).

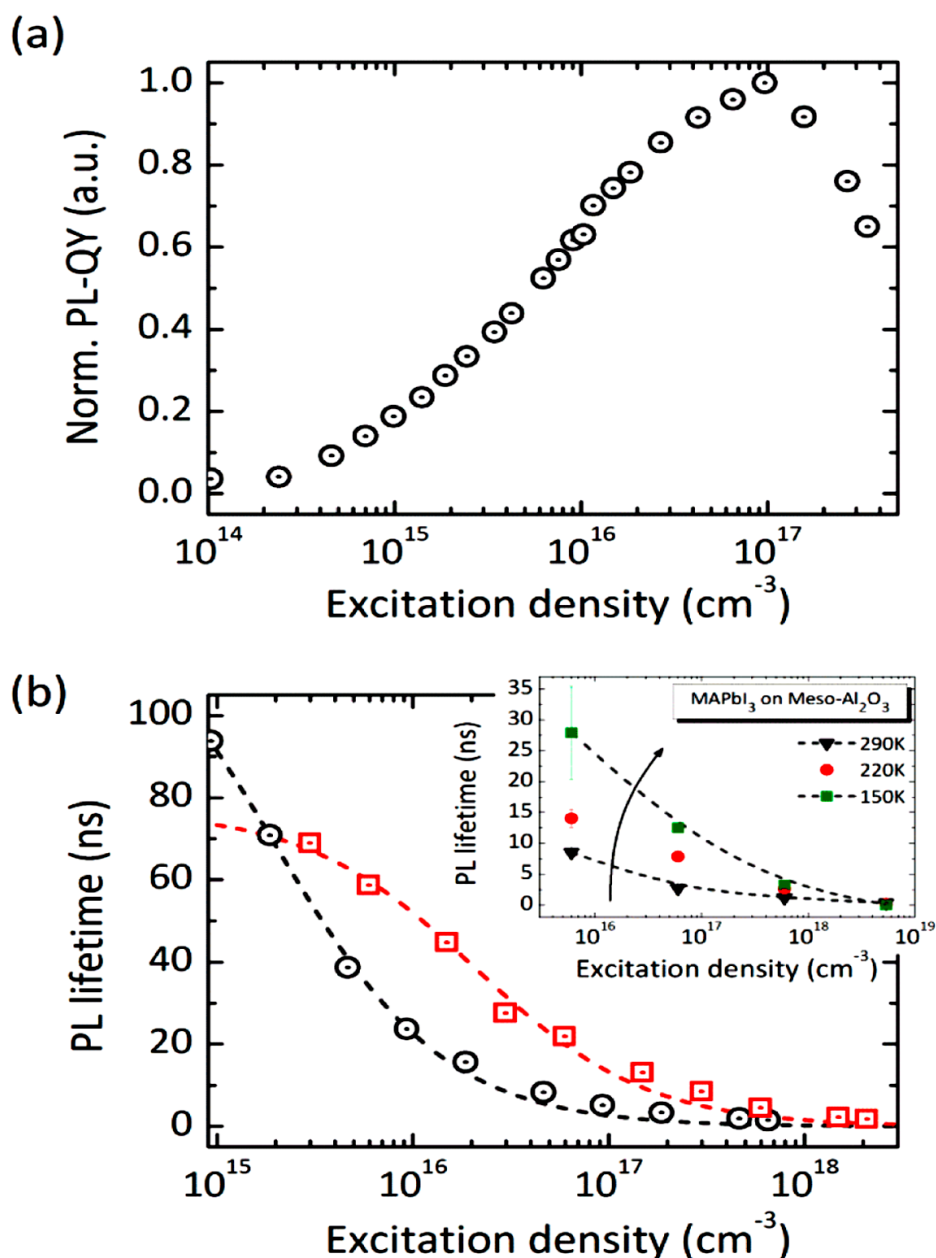


Figure 2.4: (a) Normalized PL quantum yield (calculated as the ratio of the integrated PL spectrum to the incident power) for the sample shown in Figure 2.3a. (b) PL lifetime as a function of the excitation density for MAPbI₃ samples with small (black circles) and large (red squares) crystallites. Dashed lines represents the curves obtained fitting the data to eq 1. The inset shows the PL lifetime as a function of initial excitation density for Meso-MAPbI₃ at room temperature (black triangles), 220 K (red circles), and 150 K (green squares). The error bars refer to the 95% confidence intervals of the fitted parameter values. Adapted with permission from Ref.[118].

2.4 PREPARATION METHODS OF ORGANOMETALLIC HALIDE PEROVSKITE THIN FILMS

Perovskite thin-films are prepared by four different methods reported so far, which comprises spin-coating [123], vacuum vapour deposition [124], two-step deposition technique (TSD) [125, 126 – 128] and patterning thin film [129]. One-step spin coating method was initially employed for the fabrication of the solar cells, but couldn't attain high quality film, let alone obtain the best solvent that can dissolve both organic and inorganic part. Moreover, perovskites particles were unable to effectively fill the mesoporous metal oxide (MMO) scaffold, and this lead to poor sunlight absorption. TSD was created by Mitzi and co-workers [126] for the preparation of organometallic halide perovskite. By employing TSD to coat $\text{CH}_3\text{NH}_3\text{PbI}_3$ layers, high quality thin films were achieved and as a result the large characteristics differences among devices were reduced during preparations [125]. Oriented thin films of layered perovskites with a precise control of the film property could be achieved by employing vacuum evaporation technique. Nonetheless, this technique demands high vacuum which consumes too much energy, and again, various perovskite preparation utilising different organic components is expected to be limited. The use of the vapor-assisted solution process for the fabrication of planar perovskite thin films and their corresponding solar cell has been demonstrated by a recent report [130]. In this method, film growth via in situ reaction of the as-deposited film of PbI_2 with $\text{CH}_3\text{NH}_3\text{I}$ vapour is the key step. The concept of this method differs from the current solution process and vacuum deposition method, by mitigating co-deposition of organic and inorganic species. Full surface coverage, uniform grain structure with grain size up to micrometers, and 100% precursor transformation completeness are achieved employing this approach.

2.5 BAND GAP ENGINEERING

Most of the solar energy is concentrated in the region from the visible to near infra-red (NIR) in the solar spectrum. In order for the organometallic halide perovskite materials to harvest most of the solar energy, their absorption spectrum must extensively cover the solar spectrum. Nevertheless, materials with a bandgap that is too small results in a device that is able to collect most of the extra current but with low open circuit voltage (V_{OC}). For materials with a bandgap that is too wide (2 eV), only a small part of the solar spectrum will be harvested. Therefore, semiconductor materials with a bandgap in the range 1.4 – 1.6 eV are

the potential candidates for the development of single junction solar cells. The bandgap of organometallic halide perovskite materials can be decreased by (i) increasing the in-plane M-I-M bond angle, which is done by octahedral tilting distortions, (ii) increasing the dimensionality of the $MI(X)_6$ network, and (iii) by the decrease in the electronegativity of the anions system [132].

The increase in the M-I-M bond angle has a significant impact in bandgap of semiconductor materials. Different metal cations (i.e. ABl_3 ($B = Ge^{2+}, Sn^{2+},$ and Pb^{2+}), results with variations in the M-I-M bond angles, $166.27(8)^\circ$, $159.61(5)^\circ$, and $155.19(6)^\circ$, for Ge^{2+} , Sn^{2+} , and Pb^{2+} , respectively [133]. Additionally, a decreasing M-I covalent bond character was observed while going down the 14th group, attributed to an increase in the electronegativity difference of the two atoms, $Ge\ 4p < Sn\ 5p < Pb\ 6p$. Thus, the bandgap of organometallic halide perovskites ABl_3 , with different metal cations (i.e. $B = Ge^{2+}, Sn^{2+},$ and Pb^{2+}), obeys the trend $AGeI_3 < ASnI_3 < APbI_3$. Perovskites based on Sn^{2+} are more suitable candidates for applications in photovoltaics than perovskites based on Pb^{2+} due to their smaller bandgap redshift i.e. 260 nm. It has been demonstrated by recent studies that perovskite solar cells based on Sn^{2+} can attain a high short-circuit current density of approximately $20.04\ mA\ cm^{-2}$ [134]. Nevertheless, the efficiency was notably lower than that of the Pb^{2+} counterpart employing similar device architecture. Thus, the low device performance was due to lower V_{OC} and fill factor (FF).

It has been reported by previous studies that the A cation does not play any role to the band structure and the electronic properties [135]. Nevertheless, the symmetry of the BX_6^{4-} octahedral network can be affected by the size of the A cation, depending upon the difference of the tolerance factor, and therefore can modulate the bandgap. A symmetry lowering trend: $FAPbI_3 > MAPbI_3 > CsPbI_3$ [131] exists for the three cations $HN=CHNH_3^+$ (FA^+), $CH_3NH_3^+$ (MA^+), and Cs^+ , respectively. There is a gradual deviation of Pb-I-Pb bridging angles from linear conformation from $FAPbI_3$ to $CsPbI_3$ resulting in a reduction in the orbital overlap of Pb-I. Therefore, a trend in widening of bandgap is observed: $FAPbI_3 < MAPbI_3 < CsPbI_3$. Perovskites designed by a mixture of FA^+ and MA^+ in the A site results in the redshift of the optical absorption onset of $MA_xFA_{1-x}PbI_3$ in comparison to that of $MAPbI_3$, and therefore the harvesting of solar energy is enhanced. Moreover, $MA_xFA_{1-x}PbI_3$ has a longer exciton lifetime [135] and hence it exhibits higher carrier-collection efficiency in comparison to the single cations analogues. Perovskites based on FA^+ have a narrower bandgap; however, they suffer from the instability more than the perovskites based on MA^+ cation. A stable and

efficient mixed-perovskite light harvesting layer was recently designed by rational incorporation of MAPbI₃ into FAPbI₃, and the device PCE was improved to 18% [136]. The oxide perovskites, ABO₃ (A = alkaline-earth metal: Sr, Ca, or Ba and B = transition metal = Ti), have a wide bandgap in the range 3 – 5 eV and are extensively used in thin-film electronic components and electro-optical materials. Their wide band gap is due to the large difference in electronegativity between the metal and the oxygen atoms [137]. The bandgap can be reduced by decreasing the difference in electronegativity and the metal atom, for example, BiFeO₃ has a lower bandgap than BiTiO₃ because Fe has a higher electronegativity than Ti [138]. Furthermore, the bandgap of CH₃NH₃PbI₃ is only 1.55 eV lower than that of ATiO₃ regime, which is due to the smaller difference in electronegativity between I⁻ and Pb atoms (I⁻, 2.66 vs Pb²⁺, 2.33).

Decrease of the Electronegativity of the Anions. Experimental studies demonstrated that the absorption of CH₃NH₃PbX₃ shifts to the blue region of the solar spectrum with changing of anions from I⁻ to Br⁻ to Cl⁻. Mixed anions perovskites CH₃NH₃Pb(I_{1-x}Br_x)₃ showed a blue-shift absorption band-edge in comparison to that of CH₃NH₃PbI₃ due to the fact that I⁻ anion has a lower electronegativity than that of Br⁻ anion [139,140].

Tetragonal-to-Cubic Transition. There is a transition in the structure of CH₃NH₃PbBr₃ from cubic (at high temperatures) to tetragonal structure (at temperatures below 235 K [141, 142]). The transition originates from tilting of the PbBr₆ octahedral and orientation ordering of the MA cation [141,143]. The transition from cubic to tetragonal was classified as displacive [144] i.e. change in symmetry as a consequence of changes in bond length and bond angles. Recent work by Quarti and co-workers has demonstrated a gradual blue-shift of the absorption spectra in the MAPbI₃ regime when the temperature was increased from 310 to 400K, associated with an increase in bandgap from ~1.61 to ~1.69 eV [145]. Foley and co-workers demonstrated that the band gap shifting is attributed to down shift of the valence band [146], and this was confirmed by the blue-shift in the absorption spectra of MAPbI₃.

2.5.1 Organic cation (A) modification

(a) Formamidinium Perovskites

A lot of work has been devoted to perovskites materials employing methylamine CH₃NH₃⁺ (MA⁺), as an organic cation. The methylamine lead perovskites have bandgaps of 1.55 eV and beyond. The effect of replacing the methylammonium cation with a slightly larger

cation, i.e. Formamidinium $\text{HN}=\text{CHNH}_3^+$ (FA^+), has been explored by G. E. Eperon et al. [150]. The formamidinium lead trihalide perovskites have been reported to have a bandgap that can be tuned between 1.48 and 2.23 eV, which is most suitable for single junction solar cell architecture. The formamidinium perovskite also demonstrated long range of electron and hole diffusion lengths, making it a suitable candidate for planar heterojunction solar cell architectures. The planar heterojunction solar cell devices employing this material at the active layer have been fabricated and a high short-circuit current of $>23 \text{ mA cm}^{-2}$ yielded a power conversion efficiency of up to 14.2%. The high short circuit current was attributed to the reduced bandgap. Therefore, formamidinium lead triiodide perovskite is a new potential candidate in the class of organometallic halide perovskite materials.

Nevertheless, the optimal bandgap for single junction solar cells is known to be between 1.1 and 1.4 eV. The bandgaps of methylammonium lead trihalide perovskite systems are beyond this range [148], and this inspired the realisation of lower bandgap perovskite absorbers.

Although the organic cation A has been proposed to not play any major role in determining the band structure, its size is crucial. Depending on the size of the cation employed, the lattice of the perovskite can be expanded or contracted. Since the A cation must fit between the corner-sharing metal halide octahedra, there is an allowed range for the size of the A cation. The A cations with a size that is too large do not allow the 3D structure of the perovskite to be favoured instead perovskites with confined structure or lower dimensional layered structure will be formed [149]. On the other hand, A cations with a size that is too small will cause too much strain on the perovskite lattice. The impact of varying the size of the A cation in order to tune (engineer) the bandgap of the perovskite materials has been investigated. Results showed that by increasing the size of the A cation, the bandgap was reduced. This impact was investigated by synthesizing perovskites employing different A cations of different sizes, namely; methylammonium (CH_3NH_3^+) lead triiodide, cesium (Cs^+) lead triiodide, and formamidinium ($\text{HC}(\text{NH}_2)_2^+$). Formamidinium cation has a larger ionic radius and cesium has the smallest ionic radius than methylammonium. Cesium lead triiodide perovskite was observed to absorb at shorter wavelength and the formamidinium lead triiodide perovskite absorbed at much longer wavelengths than the methylammonium lead triiodide perovskite. This implies that cations with larger ionic radius expand the lattice of the perovskite and resultantly the bandgap is reduced corroborated by a redshift in absorption onset. The bandgaps of the three materials are given in Figure 2.5, which shows that by replacing methylammonium with a cation of larger ionic radius (i.e Formamidinium), the

bandgap can be tuned closer to the optimum bandgap for planar heterojunction solar cell [148].

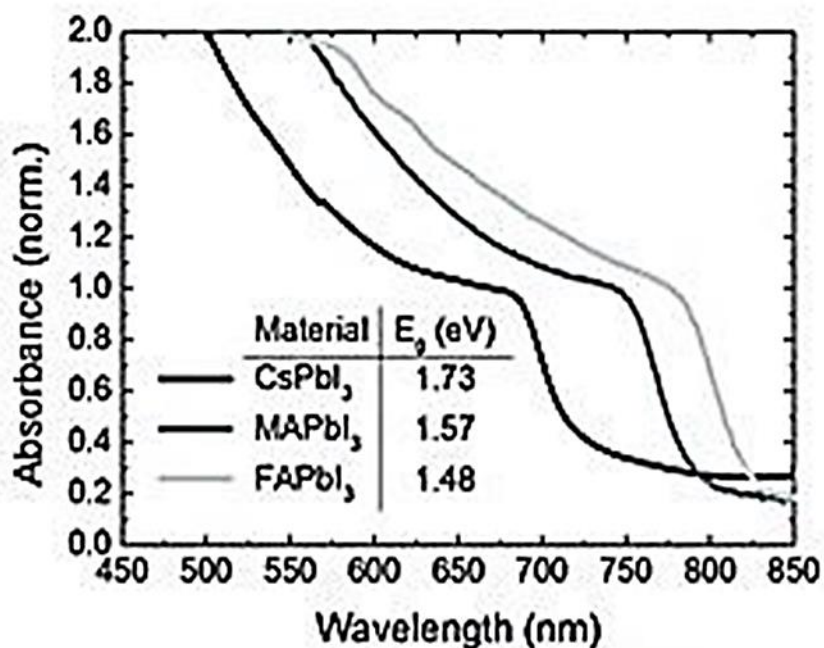


Figure 2.5: UV-Vis spectra for the APbI₃ perovskites formed, where A is either caesium (Cs), methylammonium (MA) or formamidinium (FA). Adapted with permission from Ref. [150].

A mixed halide formamidinium perovskite FAPbI_yBr_{3-y} was synthesised to explore the range of tuning the bandgap of formamidinium triiodide systems. Most of the mixed halide samples were attained, however, X-ray diffraction (XRD) demonstrated that the crystalline phases were not attained for $y = 0.5, 0.6$ and 0.8 . The absorbance and photoluminescence of the mixed halide formamidinium perovskite systems are illustrated in Figure 2.6a and b respectively. It was found that the bandgap of these systems is tuneable in the range between 1.48 and 2.23 eV. This also suggested that the bandgap of formamidinium perovskite can be tuned over a wide range implying a wide flexibility of the system. A narrower bandgap of 1.48 eV was attained for formamidinium lead iodide perovskite (at ~840 nm absorption onset) than the commonly used methylammonium lead iodide perovskite (~1.57 eV). The bandgap of formamidinium lead iodide perovskite lies closer to ideal bandgap (1 – 1.4 eV) for optimum planar heterojunction solar cells. Higher photocurrents should be attained by harnessing more of the solar spectrum, if more photogenerated electrons and holes are suitably long lived and mobile to be extracted from the solar cell.

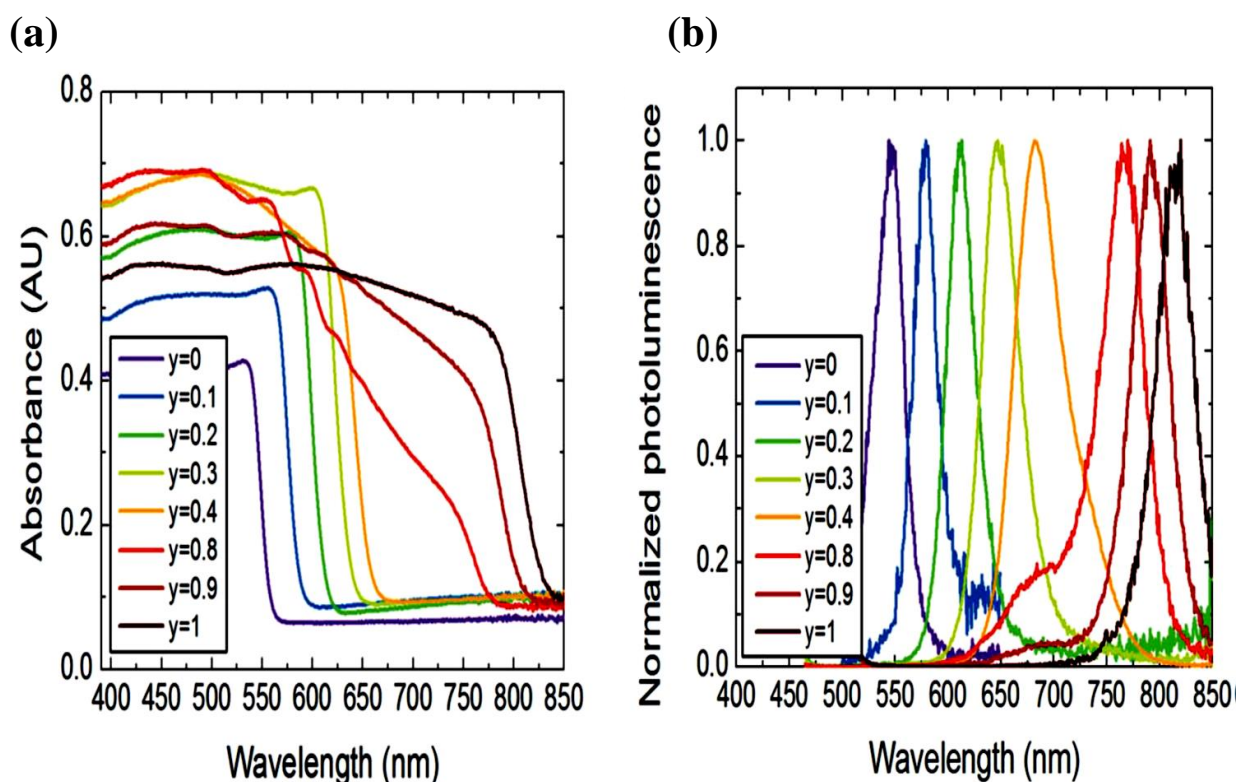


Figure 2.6: Tunability of the $\text{FAPbI}_y\text{Br}_{3-y}$ perovskite system. (a) UV-Vis absorbance of the $\text{FAPbI}_y\text{Br}_{3-y}$ perovskites with varying y , measured in an integrating sphere. (b) Corresponding steady-state photoluminescence spectra for the same films. Adapted with permission from Ref. [150].

For a material to be compatible for planar heterojunction architecture, it must have good charge transport abilities across the film thickness greater than the absorption depth of a few hundred nanometers. Time resolved photoluminescence quenching experiments were performed to determine the optimum architecture for utilization of FAPbI_3 into photovoltaic cells. These experiments were performed to obtain electron and hole effective diffusion lengths as 177 ± 2 nm and 813 ± 72 nm. Notably, both electron and hole diffusion lengths for FAPbI_3 are longer than those of MAPbI_3 , however, they are shorter than those in the mixed halide system $\text{MAPbI}_{3-x}\text{Cl}_x$ which are over a 1 micron for both electrons and holes [151].

An efficiency of up to 14.2% attributed to the high short-circuit current of over 23 mA cm^{-2} was achieved for the best performing device optimised with FAPbI_3 perovskite utilizing compact TiO_2 and Spiro-OMeTAD as electron and hole-transporting materials, respectively, and this made a new record for the solution-processed planar heterojunction perovskite solar cells. A photocurrent out to ~ 840 nm was generated due to a narrower bandgap, which was better than only 800 nm attainable with the conventional MAPbI_3 material [147]. The FAPbI_3

perovskite system has higher power conversion efficiency mainly due to two advantages. The first advantage is that with FAPbI_3 , uniform and continuous thin films with few pinhole or defects can be formed via solution-processing, which has been a huge challenge for the MAPbX_3 thin films [152]. With uniform perovskite coverage, the open circuit voltage can be maximized. The second advantage is that, the narrow bandgap of ~ 1.48 eV in comparison to ~ 1.57 eV in the $\text{MAPbI}_{3-x}\text{Cl}_x$, allows for the harnessing of most of the solar spectrum, and it is closer to the ideal bandgap for a hetero junction solar cell. A corresponding drop in V_{OC} was expected for a narrower bandgap. The best FAPbI_3 planar heterojunction solar cell attained V_{OC} of 0.94 V in comparison to 0.97 V attained in the best $\text{MAPbI}_{3-x}\text{Cl}_x$ solution processed planar heterojunction solar cells [151].

Devices fabricated with increased bromide content $\text{FAPbI}_y\text{Br}_{3-y}$ were also explored. High open circuit voltages were expected since the devices have a higher bandgap, as it was previously observed with the MAPbX_3 system [153, 154]. Planar heterojunction solar cells were fabricated for different compositions of $\text{FAPbI}_y\text{Br}_{3-y}$ for $y = 0$ (FAPbBr_3), $y = 0.8$ ($\text{FAPbI}_{0.8}\text{Br}_{2.2}$) and $y = 1$ (FAPbIBr_2). Higher open circuit voltages of 0.1 V accompanied by a drop in photocurrent were observed as the iodide content was decreased (increasing the bromide content) from $y = 1$ to $y = 0.8$. This was in agreement with an increase in bandgap from 1.48 eV to 1.55 eV and hence the increase in V_{OC} was expected.

(b) Mixed-Organic-Cation Perovskites

Organic-inorganic hybrid perovskites are prepared by employing a variety of organic cations [157,158-164]. The size of the organic ammonium cation has been demonstrated to have influence on the optical bandgap of the perovskite materials by affecting the M-I-M (M=Sn, Pb) bond angle or by enhancing the formation of insulating barriers between semiconducting PbI_4 layers [160]. The bigger cations lead to formation of two-dimensional perovskites with PbI_6^{4-} edge sharing octahedrons. The two dimensional (2D) perovskites i.e iodoplumbate and iodostannate, have been reported to have wider bandgaps [166,167], making them unsuitable for panchromatic absorption of the visible solar spectrum. Various organic cations have been demonstrated to have an effect on the bandgap by as much as 1 eV in iodostannate [166]. In theory, methylammonium (CH_3NH_3 , MA^+) and formamidinium ($\text{HN}=\text{CHNH}_3$, FA^+) cations are small enough to form 3D perovskites, in contrast to ethylammonium ($\text{CH}_3\text{CH}_2\text{NH}_3^+$)

which is known to form a 2D perovskite [157]. Mitzi and co-workers described FASnI₃ early in 1995 [161], and its Pb analogue was recently explored by Kanatzidis and coworkers [168], both reported a significant redshift of the optical absorption in comparison to that of MAPbI₃. Formamidinium cation has been reasoned to offer lower band gap of 1.4 eV [169] to the conventional MAPbI₃, which is most favourable to convert AM 1.5 sunlight to electricity. The bandgap of MAPbI₃ was tuned by gradual substitution of MA with FA cations while monitoring the shift in the optical response. Studies on mixed-organic-cations perovskites focused on their electronic properties. A semi-conductor-to-metal transition within the series (HN = CHNH₃)₂-(CH₂NH₃)_nSn_nI_{3n+2} [161,170], as *n* increased, was described by Mitzi and co-workers. The three dimensional (3D) perovskites employing mixed-organic-cations and Sn as a metal i.e (HN =CHNH₃)_{0.5}(CH₃NH₃)_{0.5}-SnI₃ [171]; have also been synthesized, nonetheless, their photovoltaic and optical properties were not explored. A lot of attention on bandgap tuning of metal halide perovskites has been devoted on the mixing of halide anions e.g Br/I [167,172] or Cl/I [155,163] rather than employing mixed cations.

The study of 3D perovskites employing a mixed-organic-cations (MA)_x(FA)_{1-x}PbI₃ (*x* = 0 – 1) prepared by sequential deposition method [156] has also been explored as photoactive layers in mesoscopic solar cells by N. Pellet et al [173]. The sequential deposition method was used as a powerful technique to yield perovskites crystals composed of both methylammonium and formamidinium cations in accurate proportions. Fully functional photovoltaic (PV) devices were tested employing 2,2',7,7'-tetrakis(N,N-di-p-methoxyphenylamine)-9,9'-spiro-bifluorene (spiro-OMeTAD) as the hole-transporting material (HTM) [174], a mesoscopic TiO₂ scaffold (m-TiO₂) for infiltration of nanostructured perovskite, and a compact TiO₂ film (b-TiO₂) as the hole-blocking layer. The results showed remarkable improvements in PV performance from employing mixed-organic-cations as photoactive layers.

Ultraviolet Visible (UV/Vis) absorption spectra of mixed-organic-cations lead iodide perovskites (MA)_x(FA)_{1-x}PbI₃ for various compositions is shown in Figure 2.7a. The results of UV/Vis showed that only 20 mol % FAI redshifted the absorption onset of the perovskite by 20 nm, while the steepness of the absorption edge for MAI was preserved. The absorption onset shifted to longer wavelengths with further increase in FAI concentration, while the film absorbance decreased. The best ratio of mixed-organic-cations MAI:FAI for optimum

extension of light absorption to near IR was proven to be 4:1 or 3:2 in 2-propanol bath solution, with retention of high absorption coefficient of MAPbI₃. The tailing of absorbance beyond the bandgap for MAPbI₃ perovskite proved that MAPbI₃ scatters light more strongly than FAPbI₃. This difference in light scattering is attributed to smaller crystal size of FAPbI₃ in comparison to their methylammonium counterparts.

Figure 2.7a shows the normalised near-infrared photoluminescence (PL) of the (MA)_x(FA)_{1-x}PbI₃ (x = 0 – 1) films. A remarkable red shift by 27 nm in the emission peaks from MAPbI₃ (λ_{max} = 776 nm) to FAPbI₃ (λ_{max} = 803 nm) was noted, consistent with absorption spectrum, together with a noticeable broadening of the emission profile. The observed similar trends suggest that the ratio of the incorporated organic cations corresponds to that of the dissolved organic-cations in the precursor solution. The interactions between methylammonium and formamidinium cations were confirmed by the non-linearity of the emission shifts.

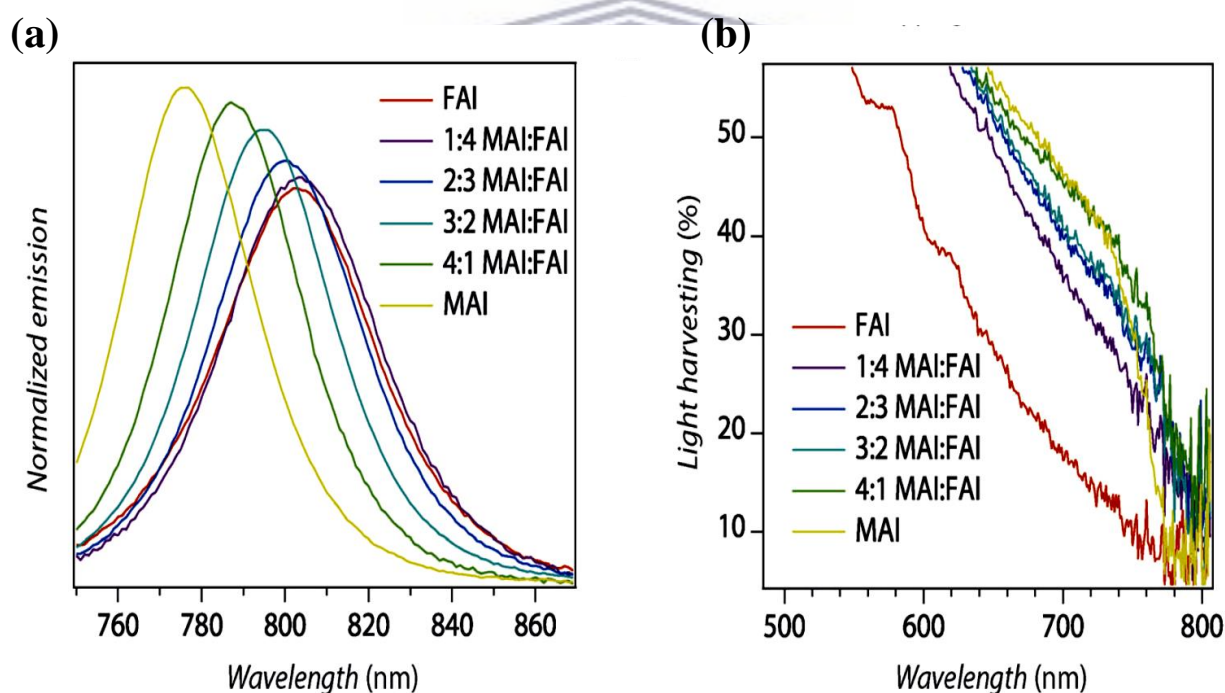


Figure 2.7: (a) Normalized emission of (CH₃NH₃)_x-(HNCHNH₃)_{1-x}PbI₃ (x = 0, 0.2, 0.4, 0.6, 0.8, 1). The emission is shifted further into the red and broadened as x is decreased. (b) Light harvesting spectra of the different perovskite films recorded in integrating sphere. Note the 20 nm red shift of the absorbance onset for (CH₃NH₃)_{0.8}-(HNCHNH₃)_{0.2}PbI₃ as compared to (CH₃NH₃)PbI₃. As the formamidinium concentration was increased, the absorbance of the film decreased, while no change in the bandgap was discernible. Adapted with permission from Ref. [173].

Devices based on pure MAPbI₃ yielded short circuit current density J_{SC} of 17.83 mAcm⁻², open circuit potential V_{OC} of 1046 mV, fill factor FF of 0.655, and power conversion efficiency PCE of 12.5%, respectively. The devices based on MAPbI₃ yielded a short circuit current density of 17.3 mAcm⁻² and a PCE of 12.0% on average, and this was in agreement with the results reported previously [156]. The pure formamidinium lead iodide FAPbI₃ yielded $J_{SC} = 16.6$ mAcm⁻², $V_{OC} = 928$ mV, FF = 0.66, and PCE = 10.5%. A PCE of 11.0% was attained for the most efficient FAPbI₃-based devices, which was below the average PCE attained for pure MAPbI₃. Mixed-cation perovskites (MA)_x(FA)_{1-x}PbI₃ of different ratio compositions $x = 0.2, 0.4, 0.6,$ and 0.8 were also tested. The perovskite of composition MA_{0.6}FA_{0.4}PbI₃ gave the best performance amongst the rest. The typical cell device based on MA_{0.6}FA_{0.4}PbI₃ yielded an $V_{OC} = 1027$ mV, $J_{SC} = 18.15$ mAcm⁻², a FF of 0.715, and a PCE of 13.4%. Noticeably, the MA_{0.6}FA_{0.4}PbI₃ had higher performance than the single-cation compositions, FAPbI₃ and MAPbI₃. The *J-V* characteristics of the best MA_{0.6}FA_{0.4}PbI₃ device yield $J_{SC} = 21.2$ mAcm⁻², $V_{OC} = 1.003$ V, and FF = 0.70 which resulted in an overall power-conversion efficiency of 14.9%.

The incident-photon-current conversion efficiency (IPCE) or the external quantum efficiency (EQE) was measured across the visible spectrum in order to rationalize the substantial gains in photocurrent observed for the mesoscopic cells based on mixed-cation perovskite light harvesters. It was found that the photocurrent onset shifted by 20 nm to the red from 780 to 800 nm for FAPbI₃ and MA_{0.6}FA_{0.4}PbI₃. This was in accordance with the absorbance spectra shown in Figure 2.7b. MA_{0.6}FA_{0.4}PbI₃ showed an impressive spectrum that has a combination of the advantages of the red-shifted onset observed for FAPbI₃ with a steep increase in the IPCE at bandgap characteristic of the MAPbI₃. MA_{0.6}FA_{0.4}PbI₃ achieved IPCE values transcending the ones achieved with two single cation perovskites across the whole visible range and reached about 90% at a wavelength of 500 nm. The IPCE spectra of MAPbI₃, FAPbI₃, and MA_{0.6}FA_{0.4}PbI₃ from 340-850 nm, produced short circuit photocurrent densities of 17.0, 16, and 20.2 mAcm⁻², respectively. A fastest drop in absorbance with increasing wavelength was observed for FAPbI₃, while MAPbI₃ was the slowest, and the mixed-cation perovskite was average. MAPbI₃ showed a redshift in bandgap at a wavelength of 787 nm (1.575 eV), and FAPbI₃ at 810 nm (1.530 eV). MA_{0.6}FA_{0.4}PbI₃ exhibited the same bandgap as FAPbI₃, which was opposite to the expectations.

The absorbed-photon-to-current conversion efficiency (APCE) or internal quantum efficiency (IQE) of these materials was also investigated. High APCE values of 80-85% were

maintained throughout the visible spectrum for $\text{MA}_{0.6}\text{FA}_{0.4}\text{PbI}_3$. These values confirmed high quantum efficiency of carrier generation and collection by the device, different to MAPbI_3 and FAPbI_3 , which collect a little quantity of charges produced by red photons than by blue photons, resulting in shorter carrier-diffusion length for the single-cation perovskite phases. The photoluminescence life time of the perovskite deposited on nonconductive glass from solutions of MAI/FAI and PbI_2 in *N,N*-dimethylformamide (DMF) was measured to further substantiate this interpretations. An impressive emission of 85% decay was displayed by $\text{MA}_{0.6}\text{FA}_{0.4}\text{PbI}_3$ with a long lifetime of 130 ns, therefore this emission stayed longer than the ones for the pure-phase perovskites. The prolonged lifetime in the mixed-cation perovskite improves the carrier-collection efficiency as seen with $\text{MA}_{0.6}\text{FA}_{0.7}\text{PbI}_3$, since it enhances the diffusion length of the material.

2.5.2 Metal (B) modification

(a) Tin Perovskites

It has been demonstrated by recent studies that mixed halide organic inorganic perovskites materials show electron-hole diffusion lengths beyond 1 μm , which is consistent with reports of very high carrier mobilities observed in these materials [179] and substantiate the anticipation for highly efficient and cheap solar cells employing thick absorption layers [180,181]. The toxicity of lead Pb metal used in the materials prevents the commercialization of this technology. Hence, it is crucial to achieve ideal optical and photovoltaic performance employing lead-free organic inorganic materials. A first attempt employing lead free perovskites $\text{CH}_3\text{NH}_3\text{SnI}_3$ as a sunlight harvester for fabrication of solution-processed photovoltaic cell was reported by F. Hao et al. [185]. The methylammonium tin iodide perovskite $\text{CH}_3\text{NH}_3\text{SnI}_3$ features an even lower bandgap of 1.3 eV than the 1.55 eV achieved with the benchmark counterpart $\text{CH}_3\text{NH}_3\text{PbI}_3$. Photovoltaic devices employing $\text{CH}_3\text{NH}_3\text{SnI}_3$ as a sunlight harvester and spiro-OMeTAD as a hole-transporting material attained an absorption onset of 950 nm. An efficient energetic tuning of the band structure for $\text{CH}_3\text{NH}_3\text{SnI}_3$ was achieved by blending of iodide with bromide, yielding a PCE of 5.8% under simulated solar illumination of 100 mW cm^{-2} . $\text{CH}_3\text{NH}_3\text{SnI}_3$ takes on a perovskite structure and it crystallizes in the pseudocubic space group $P4mm$ under ambient conditions.

CH₃NH₃SnI₃ is classified as a direct-bandgap semiconductor with a bandgap of 1.3 eV, as this has been demonstrated both experimentally and theoretically [179, 182]. The material displays a strong photoluminescence emission at 950 nm at room temperature, and this corresponds to the absorption onset shown in Figure 2.8a. The intensity of photoluminescence is proportional to number of e⁻h⁺ pairs produced by the incident light [183], and therefore the photoluminescence intensity serves as a qualitative measure of the number of photogenerated carriers in semiconductors. The bulk electrical conductivity was determined as $\sigma \sim 5 \times 10^{-2} \text{ S cm}^{-1}$ at room temperature, corresponding to a Seebeck coefficient of $\sim -60 \mu\text{V K}^{-1}$ (n-type). The CH₃NH₃SnI₃ material holds very low carrier concentration on the order of $\sim 1 \times 10^{14} \text{ cm}^{-3}$ and high electron mobilities (μ_e) on the order of $\sim 2,000 \text{ cm}^2 \text{ V}^{-1} \text{ s}^{-1}$, which is close or even transcending most of the conventional semiconductors, including Si, CuInSe₂ and CdTe, which have close energy gaps. Ultraviolet Photoelectron Spectroscopy (UPS) measurements were used to determine the valence band maximum (E_{VB}) of the CH₃NH₃SnI₃ material and it was estimated to be ~ -5.47 eV below vacuum level, which is comparable to the reported value for CH₃NH₃PbI₃ (~ -5.43 eV) [175]. The conduction band energy E_{CD} of CH₃NH₃SnI₃ was determined to be ~ -4.17 eV, from the observed optical bandgap value. The conduction band energy E_{CD} of CH₃NH₃SnI₃ is slightly higher than the E_{CD} for the TiO₂ anatase electrode (~ -4.26 eV) [175].

Devices based on CH₃NH₃SnI₃ as the light absorbing layer exhibited a high mean short-circuit photocurrent density J_{SC} of 16.30 mA cm^{-2} , an open circuit voltage V_{OC} of 0.68 V and a moderate fill factor (FF) of .048, yielding a corresponding PCE of 5.23%. The incident photon-to-electron conversion efficiency (IPCE) of the solar cell device based on CH₃NH₃SnI₃ exhibits improved panchromatic property by covering the entire visible spectrum and absorbs to maximum of over 60% from 600 nm to 850 nm. This IPCE value of 60% was accompanied with a remarkable absorption onset of 950 nm, which corresponds well with the optical bandgap of ~ 1.30 eV. A current density of 16.60 mA cm^{-2} was obtained by integrating the overlap of the IPCE spectrum with the AM 1.5G solar photon flux, and this value (16.60 mA cm^{-2}), was in good agreement with determined photocurrent density.

It was noted that although the obtained J_{SC} for the CH₃NH₃SnI₃ perovskite device is less efficient than that for the CH₃NH₃PbI₃ device [176,177,178,152], the maximum current density that can be generated is beyond 30 mA cm^{-2} when AM 1.5G solar spectrum is

integrated to values below the bandgap of $\text{CH}_3\text{NH}_3\text{SnI}_3$ material (1.30 eV). It has been observed recently that the charge accumulation in high density also occur in the perovskite absorber material and not only in the semiconducting TiO_2 electrodes, making perovskite device basically different from dye-sensitized solar cells [184]. Consequently, the V_{OC} in a perovskite device is not only related to the difference in energy between the HTM potential and TiO_2 conduction bandedge, but it is also correlated with the difference in energy between the HTM potential and the conduction bandedge of the perovskite itself. Thus, it could be concluded that the conduction bandedge E_{CD} of $\text{CH}_3\text{NH}_3\text{SnI}_3$ is ~ 0.24 eV lower than that of $\text{CH}_3\text{NH}_3\text{PbI}_3$, yielding a lower V_{OC} for $\text{CH}_3\text{NH}_3\text{SnI}_3$ perovskite solar cell device.

Chemical substitution of iodide atom with bromide was applied to engineer the bandgap energetics [175] as an attempt to increase the open circuit voltage V_{OC} of lead-free devices. Mixed halide compounds of $\text{CH}_3\text{NH}_3\text{SnI}_{3-x}\text{Br}_x$ were synthesized by stoichiometric mixing of $\text{CH}_3\text{NH}_3\text{X}$ and SnX_2 ($\text{X} = \text{Br}, \text{I}$). Ultraviolet-visible diffuse reflectance spectra of $\text{CH}_3\text{NH}_3\text{SnI}_{3-x}\text{Br}_x$ ($x = 0, 1, 2, 3$) were measured and converted to absorption spectra, to investigate the optical properties in the hybrid mixed halide perovskites. The absorption onset of hybrid mixed halide perovskites $\text{CH}_3\text{NH}_3\text{SnI}_{3-x}\text{Br}_x$ ($x = 0, 1, 2, 3$) could be tuned from 954 nm (1.30 eV for $\text{CH}_3\text{NH}_3\text{SnI}_3$) to 577 nm (2.15 eV for $\text{CH}_3\text{NH}_3\text{SnBr}_3$), resulting in notable colour tunability for hybrid mixed halide perovskites. $\text{CH}_3\text{NH}_3\text{SnI}_2\text{Br}$ and $\text{CH}_3\text{NH}_3\text{IBr}_2$ iodide/bromide perovskite intermediates exhibited absorption onsets of 795 nm (1.56 eV) and 708 nm (1.75 eV), respectively.

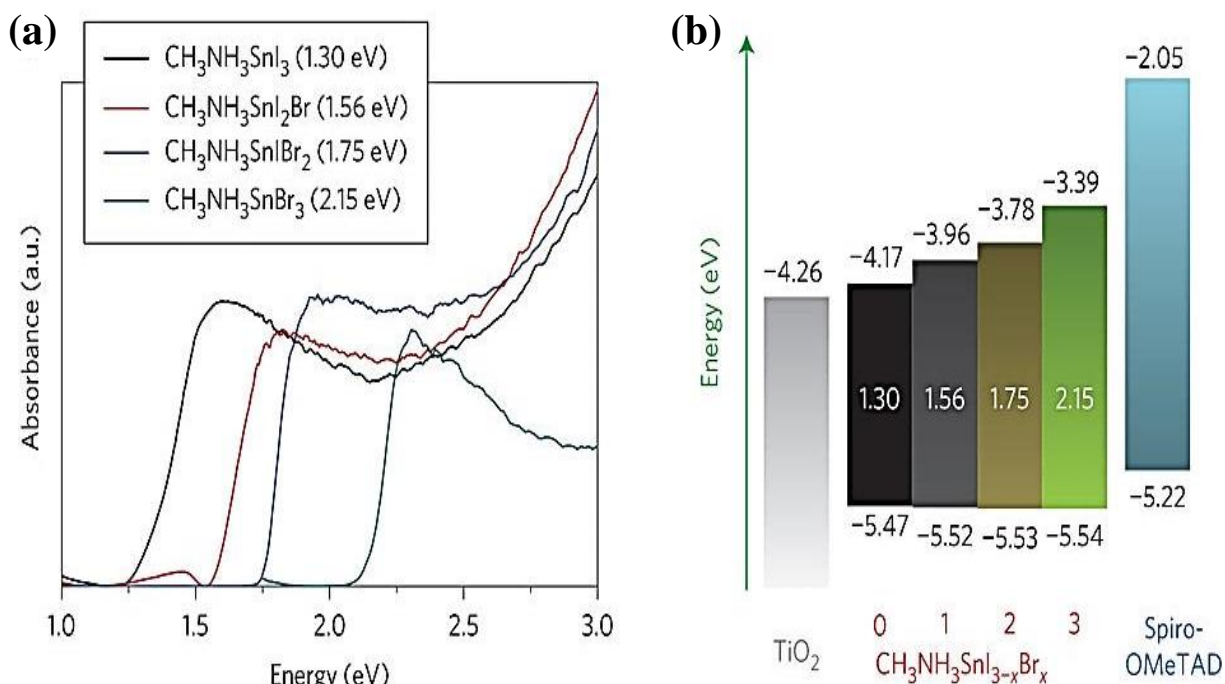


Figure 2.8: (a) Absorption spectra of the CH₃NH₃SnI_{3-x}Br_x (x = 0, 1, 2, 3) perovskites. (b) Schematic energy level diagram of CH₃NH₃SnI_{3-x}Br_x, with TiO₂ and spiro-OMeTAD HTM. The Valence band maxima E_{CB} of the methylammonium tin halides were extracted from UPS measurements under high vacuum. Adapted with permission from Ref. [185].

UPS measurements were used to estimate the valence band energy E_{VB} of the CH₃NH₃SnI_{3-x}Br_x compounds. The E_{CB} increased from -4.17 eV below vacuum level for CH₃NH₃SnI₃ to -3.96 eV for CH₃NH₃SnI₂Br and -3.78 eV for CH₃NH₃IBr₂, and finally to -3.39 eV for CH₃NH₃SnBr₃, as illustrated in Figure 2.8b. From the band alignment it was clear that the change in bandgap E_g of the CH₃NH₃SnI_{3-x}Br_x compounds is attributed by the shift in conduction band to higher energy, with the valence band remaining constant. The changes in energy levels permit bandgap engineering of perovskite materials and the modulation of energetics for more efficient solar cell architectures. Remarkably, a decrease in J_{SC} from 16.30 mA cm⁻² for CH₃NH₃SnI₃ to 8.26 mA cm⁻² for CH₃NH₃SnBr₃ was observed when increasing Br content. A significant increase in V_{OC} from 0.68 V to 0.88 V when shifting from the pure iodide to pure bromide perovskite compound was observed. A remarkable increase in FF from 0.48 to 0.59 was also observed upon incorporation of the Br ions. Mixed halide perovskite with composition CH₃NH₃SnIBr₂ amongst the investigated CH₃NH₃SnI_{3-x}Br_x perovskites, attained the highest PCE of 5.73% , with a J_{sc} of 12.30 mA cm⁻², a V_{OC} of 0.82 V and a FF of 0.57 V. A decrease in the value of J_{SC} with increasing Br content is directly proportional to the blue shift of absorption onset, as shown from the Figure 2.8a. A

blueshift in IPCE spectra from 950 nm for iodide perovskite to ~600 nm for pure bromide perovskite appeared to be consistent with the bandgap modulation. The enhancement in V_{OC} could be due to the elevated conduction band edge E_{CB} with increasing Br content in $CH_3NH_3SnI_{3-x}Br_x$.

(b) Tin-Lead (Sn-Pb) Perovskites

A recent work on hybrid metal perovskites demonstrated that solid solutions of Sn and Pb perovskites materials with optical bandgap range between 1.1 and 1.7 eV can be easily manufactured, making them potential candidates as sunlight harvesters in energy conversion or detector devices [194]. A mixed bivalent metal Sn-Pb perovskite which permitted bandgap modulation of the perovskite sunlight harvester by varying the Sn:Pb ratio has been reported by a recent study of Ogimi et al, demonstrating that Sn could be relevant for lead-free metal ion, especially for lower bandgap photovoltaic cells [195]. Nevertheless, this study reported that the pure $CH_3NH_3SnI_3$ doesn't show significant photovoltaic properties and therefore a minimum content of Pb is essential to stabilize Sn in its 2^+ state. F. Hao et al. reported a study on alloyed perovskites of methylammonium tin iodide ($CH_3NH_3SnI_3$) and its lead analogue ($CH_3NH_3PbI_3$) as novel panchromatic light absorbing material for fabrication of solution-processed solid-state solar cell devices in conjunction with an organic hole transport layer [204]. A remarkable IPCE response from visible to near infrared (up to 1050 nm) was realized for the first time with the solid solution $CH_3NH_3Pb_{1-x}Sn_xI_3$, which is currently the widest absorption range reported for solar cell devices based on perovskites [196-198]. An impressive short-circuit photo-current density of 20.64 mA cm^{-2} was obtained with mesoporous TiO_2 electrode and spiro-OMeTAD as hole transporting layer under 100 mW cm^{-2} solar illumination. Improved photocurrent density could be achieved with further device optimization to minimize charge recombination and maximize the light harvesting capacity.

The solid solution of $CH_3NH_3Sn_{1-x}Pb_xI_3$ took on the perovskite structure type which consists of $[Sn_{1-x}Pb_xI_6]^{4-}$ octahedra in which the metal position is randomly occupied by either Sn or Pb. $CH_3NH_3SnI_3$ and $CH_3NH_3PbI_3$ compounds crystallized in the pseudocubic $P4mm$ (α -phase) and tetragonal $I4cm$ (β -phase) space groups, respectively, at ambient conditions. $CH_3NH_3PbI_3$ was observed to undergo structural phase transition to the $P4mm$ space group at high temperatures, thus becoming isostructural to its Sn analogue. $CH_3NH_3Sn_{1-x}Pb_xI_3$ also

exhibited the same structural change under ambient conditions. A distortion of the relative positions of the octahedral about the 4-fold crystallographic axis (*c*-axis) is involved in such transition. The tilting angle between $[\text{SnI}_6]^{-4}$ octahedra is $177.43(1)^\circ$ in ideal case of $\text{CH}_3\text{NH}_3\text{SnI}_3$, and this angle deviates slightly from the ideal straight angle. In the ideal case of $\text{CH}_3\text{NH}_3\text{PbI}_3$, the tilting angle is enlarged at $163.55(1)^\circ$, notably distorting the $(\text{PbI}_3)^-$ framework, and consequently reducing the symmetry of the unit cell. The intermediate $\text{CH}_3\text{NH}_3\text{Sn}_{0.43}\text{Pb}_{0.57}\text{I}_3$ composition adopted the tetragonal *I4cm* structure [194] corresponding to an angle of magnitude equal to $169.43(1)^\circ$ when compared to $\text{CH}_3\text{NH}_3\text{SnI}_3$ and $\text{CH}_3\text{NH}_3\text{PbI}_3$. The deviations from the ideal cubic (*Pm-3m*) structure are due to orientational ordering of the CH_3NH_3^+ cation along the crystallographic *c*-axis. The tilting of the octahedra gives rise to the difference between the two structural types. For example, the tilting of $\text{CH}_3\text{NH}_3\text{PbI}_3$ occurs in opposite sense along the (pseudo)-tetragonal axis which is out of plane tilting, in contrast to in-phase tilting observed for β - CsSnI_3 and α - $\text{HC}(\text{NH}_2)_2\text{SnI}_3$. The electrical conductivity of perovskites becomes optimal for the least distorted Sn/Pb-I-Sn/Pb angles and therefore the charge-transport properties is a reflection of the structural qualities of the perovskites. The Sn-I-Sn bond angle in $\text{CH}_3\text{NH}_3\text{SnI}_3$ deviates slightly from linearity and hence the material exhibits the highest conductivity amid $\text{CH}_3\text{NH}_3\text{Sn}_{1-x}\text{Pb}_x\text{I}_3$ compounds, whereas $\text{CH}_3\text{NH}_3\text{PbI}_3$ with the largest tilting angle is the lowest conductive material.

The semiconducting behaviour of all the $\text{CH}_3\text{NH}_3\text{Sn}_{1-x}\text{Pb}_x\text{I}_3$ compositions was realised with increase in conductivity with increasing temperature which was also in agreement with the optically determined bandgap energies within the range 1.15 – 1.55 eV. Additionally, the n-type semiconductor behaviour of all solid solution compositions was realised with the Seebeck coefficient decreasing dramatically as the Pb content increased (i.e., as the x-value increased). An observed decrease in carrier concentration from $1.1 \times 10^{14} \text{cm}^{-3}$ for $\text{CH}_3\text{NH}_3\text{SnI}_3$ to $\sim 4.8 \times 10^{14} \text{cm}^{-3}$ for $\text{CH}_3\text{NH}_3\text{PbI}_3$ was dictated by the bandgaps of the compounds. Diffuse reflectance measurements were used to determine the optical bandgaps (E_g) of the $\text{CH}_3\text{NH}_3\text{Sn}_{1-x}\text{Pb}_x\text{I}_3$ solid solutions. The transformed Kubelka-Munk UV-vis near-IR absorption spectra for the synthesized $\text{CH}_3\text{NH}_3\text{Sn}_{1-x}\text{Pb}_x\text{I}_3$ serial compounds is shown in Figure 2.9a. Solid solutions of $\text{CH}_3\text{NH}_3\text{Sn}_{1-x}\text{Pb}_x\text{I}_3$ with a tunable bandgap between the range 1.17 and 1.55 eV were synthesized by stoichiometric mixing of the divalent metal iodides of Sn and Pb with methylammonium iodide. The smallest bandgaps of 1.17 eV were attained for the intermediate compounds with $x = 0.2$ and 0.5. The ideal optimal bandgap for single

junction solar cell is between 1.1 and 1.4 eV, and this range is currently beyond the most studied methylammonium lead trihalide systems [199]. Therefore, the $\text{CH}_3\text{NH}_3\text{Sn}_{1-x}\text{Pb}_x\text{I}_3$ series is a promising candidate for more efficient single junction and tandem architecture photovoltaic devices where the optimum bandgap for a bottom cell lies in around 1 eV [186]. Ultraviolet photoelectron spectroscopy (UPS) was further employed to interrogate the valence bandgap energies (E_g). The E_{VB} was estimated to decrease from -5.45 eV below vacuum level for $\text{CH}_3\text{NH}_3\text{PbI}_3$ with decreasing x fraction from 1 to 0.25 as shown from Figures 2.9b. Nevertheless, the E_{VB} for neat tin material $\text{CH}_3\text{NH}_3\text{SnI}_3$ was found to be around -5.47 eV, which was comparable to that of neat lead material $\text{CH}_3\text{NH}_3\text{PbI}_3$. The conduction band energy (E_{CB}) of $\text{CH}_3\text{NH}_3\text{Sn}_{1-x}\text{Pb}_x\text{I}_3$ from the observed optical bandgaps is also shown in the diagram of Figure 2.9b.

High quality film coverage was displayed by the $\text{CH}_3\text{NH}_3\text{Sn}_{0.5}\text{Pb}_{0.5}\text{I}_3$ in contrast to $\text{CH}_3\text{NH}_3\text{PbI}_3$ film. This suggested the formation of smaller crystallite domains implying more efficient film formation through a favourable crystal growth of the mixed-metal perovskite [200,201]. Solar cell devices based on $\text{CH}_3\text{NH}_3\text{Sn}_{1-x}\text{Pb}_x\text{I}_3$ as sunlight absorbers in the active layer and 2,2',7,7'-tetrakis(N,N-di-p-methoxyphenylamine)-9,9'-spirobifluorene (spiro-MeOTAD) with lithium bis(trifluoromethylsulfonyl)imide and pyridinium additives as a hole transporting materials (HTM) were constructed and tested. Devices based on neat tin $\text{CH}_3\text{NH}_3\text{SnI}_3$ perovskites exhibited a remarkable short-circuit photocurrent density (J_{SC}) of 15.18 mA cm^{-2} , an open-circuit voltage (V_{OC}) of 0.716 V and a fill factor (FF) of 50.07% under AM1.5G solar illumination, which yielded a power conversion efficiency (PCE) of 5.44%. The significant power conversion efficiency of neat tin (lead free) perovskite was noteworthy. However, this photocurrent density was lower when compared to the reported neat lead $\text{CH}_3\text{NH}_3\text{PbI}_3$ perovskite based device [187-192,193], which could be attributed by the poor perovskite film quality and low coverage on the TiO_2 electrode. Nevertheless, $\text{CH}_3\text{NH}_3\text{SnI}_3$ solid state device showed a broad coverage of the entire visible spectrum from 500 to 850 nm and reached broad absorption coverage of 50% together with a significant absorption onset of up to 950 nm. This was in good agreement with the optical bandgap of 1.3 eV. The obtained V_{oc} for $\text{CH}_3\text{NH}_3\text{SnI}_3$ was notably higher than the one reported by Omigi et al, and this proved that Sn halide perovskite did not exhibit any photovoltaic properties in itself [195]. Sn perovskite devices reported on literature show low photovoltage, which could be attributed by the oxidation of Sn^{2+} in the Sn perovskites, confirmed by the extra Bragg peaks at approximately 15° and 30° in the X-ray powder

diffraction spectrum. These extra peaks could be assigned to the $\text{Sn}^{4+} (\text{CH}_3\text{NH}_3)_2\text{SnI}_6$ compounds [194]. The oxidation could be induced by self-doping of the Sn perovskite [202,203] or from external environment during device preparations.

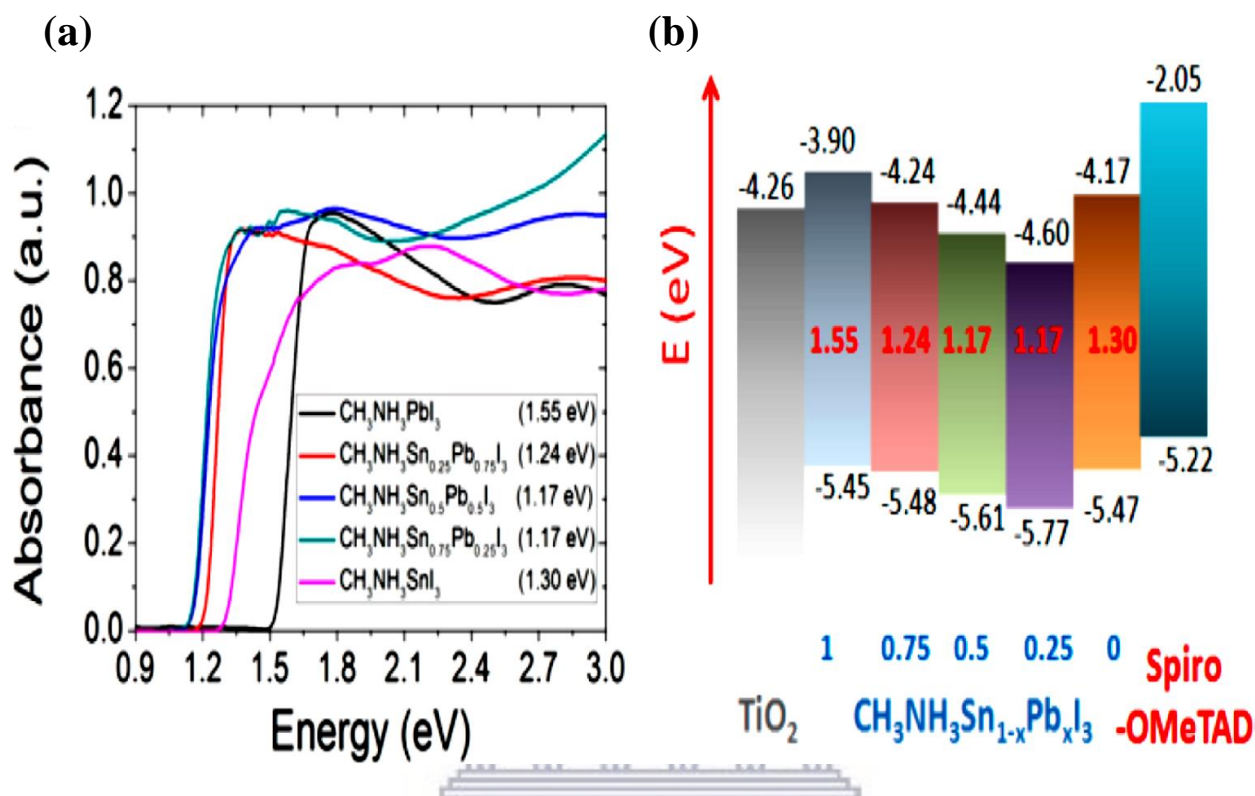


Figure 2.9: Absorption spectra and schematic energy level diagram of the $\text{CH}_3\text{NH}_3\text{Sn}_{1-x}\text{Pb}_x\text{I}_3$ solid solution perovskites. (a) Electronic absorption spectra and (b) schematic energy level diagram of the $\text{CH}_3\text{NH}_3\text{Sn}_{1-x}\text{Pb}_x\text{I}_3$ solid solution perovskites. The valence band maximum (E_{CB}) of the hybrid methylammonium tin/lead triiodide were extracted from UPS measurements under high vacuum. Adapted with permission from Ref. [204].

This work gave the first report of the panchromatic IPCE response from visible to near infrared spectrum (1.1 eV, up to 1050 nm) attained with solid solution $\text{CH}_3\text{NH}_3\text{Sn}_{1-x}\text{Pb}_x\text{I}_3$ for high-performing perovskite based devices [196-198]. A remarkable decrease in V_{OC} from 0.863 to 0.376 V was observed when switching from the neat lead $\text{CH}_3\text{NH}_3\text{PbI}_3$ perovskite to the solid solution of $\text{CH}_3\text{NH}_3\text{Sn}_{0.75}\text{Pb}_{0.25}\text{I}_3$. This decrease could be ascribed to the lower conduction band edge (E_{CB}) with decreasing Pb content in $\text{CH}_3\text{NH}_3\text{Sn}_{1-x}\text{Pb}_x\text{I}_3$ solid solution as shown in the energy diagram of Figure 2.9b [205]. On the other hand, the Fill Factor (FF) was significantly lower than the reported values for advance performing perovskite solar cells

[188,189,193] which could also be induced by Sn^{2+} oxidation during device manufacturing process [202].

2.5.3 Halide (X) Mixing

(a) Combined Halides (Cl, Br, I) Perovskites

The work on combined halides perovskites was first reported by B. Suarez et al [221], which exploited and focused on the charge recombination of the perovskite-based photovoltaic devices since it has direct influences on the photovoltaic parameters, and a special influence on the open circuit voltage, V_{OC} . In this work, charge recombination mechanisms were investigated and explained by analysing recombination resistance, R_{rec} , which is inversely related to the recombination rate [214]. A widely used technique for characterizing photovoltaic devices known as Impedance Spectroscopy (IS) [214] was employed to determine R_{rec} , of a series of perovskite based devices and disclosed unprecedented results [206,208,210,211,215-218].

The combined halides perovskite samples are denoted as $\text{MAPb}(\text{Br}_x\text{I}_{1-x})_{3-y}\text{Cl}_y$, where x is determined by the ratio between Br and I ions but y is not determined. The role played by the Cl ion in the perovskite preparations is still controversial, due to the fact that either significant reduced quantities of Cl have been traced in $\text{MAPbI}_{3-y}\text{Cl}_y$ or have not been traced at all [212,213]. Again, the exact impact of Cl on the electrical properties and the crystallinity of the perovskite is not known [212], hence the notation $\text{MAPb}(\text{Br}_x\text{I}_{1-x})_{3-y}\text{Cl}_y$ was used to just indicate the use of Cl precursor in the preparation of combined halides perovskites. Photovoltaic devices based on combined halides perovskite with different ion ratios, $\text{MAPb}(\text{Br}_x\text{I}_{1-x})_{3-y}\text{Cl}_y$ where $0 \leq x \leq 1$, are depicted in a picture shown in Figure 2.9a. The observed change in colour from dark brown to yellow in absorber films was tuned by controlling the content of Br. The absorption measurements of the combined halides perovskite films were also taken and are illustrated in Figure 2.10b. An increase in the Br content resulted in a systematic shift of the absorption band edge to shorter wavelengths. The energy band gap (E_g) could therefore be tuned by varying the Br/I ratio. Figure 2.10c represents the dependence of the energy band gap with the Br content. A linear correlation represented with the equation

$$E_g = 1.563 + 6.916 \times 10^{-3} \cdot [x] \quad (2)$$

where $[x]$ is the bromide percentage for samples with different halide compositions was observed. The remarkable energy band gaps obtained for $\text{MAPbI}_{3-y}\text{Cl}_y$ (1.57 eV) and $\text{MAPbBr}_{3-y}\text{Cl}_y$ (2.27 eV), were in good agreement with the values previously reported in the literature [209,219,220].

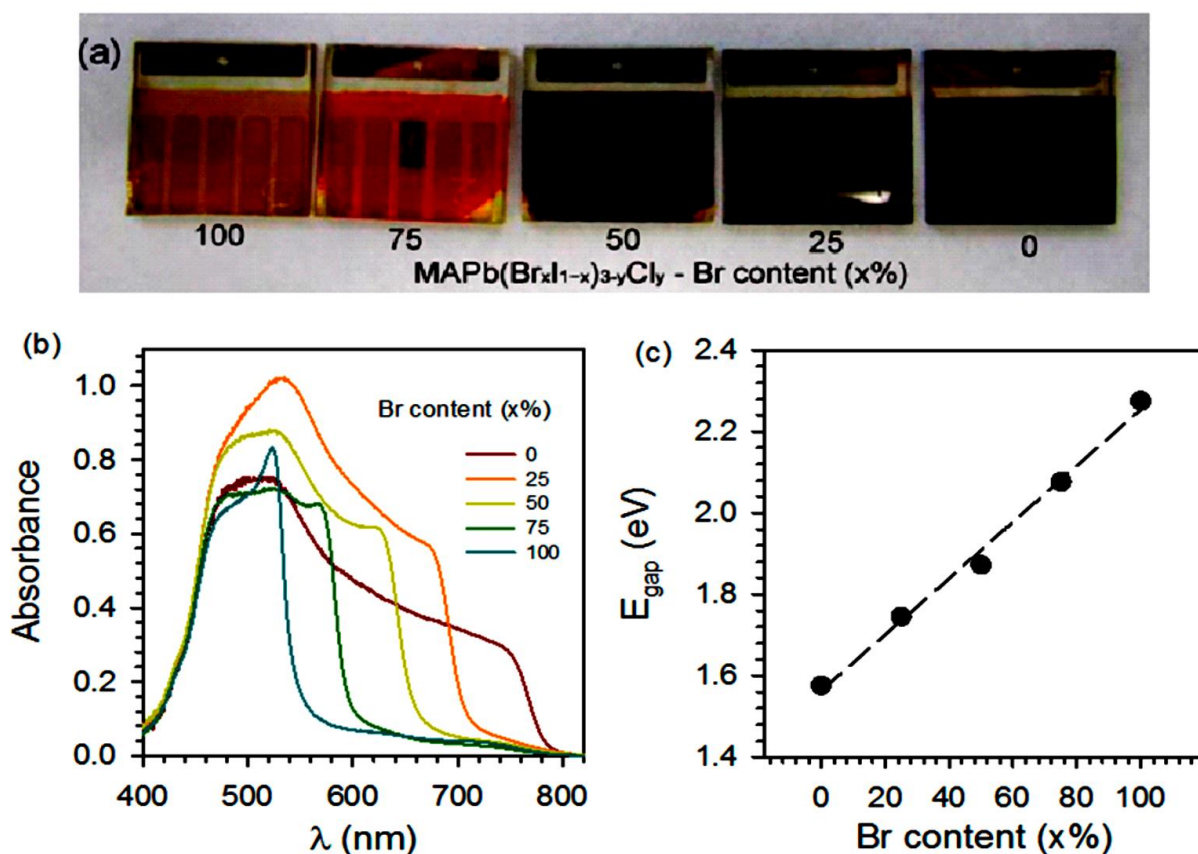


Figure 2.10: (a) Picture of $\text{MAPb}(\text{Br}_x\text{I}_{1-x})_{3-y}\text{Cl}_y$, ($0 \leq x \leq 1$) devices with different Br/I molar ratios grown on mesoporous TiO_2 substrates after sample characterization. (Yellow parts in some samples indicate degradation). (b) Absorption spectra of the samples (absorption tail observed at long wavelengths is due to the mesoporous layer light scattering). (c) The energy bandgap extracted from the absorption measurements depending on the percentage of the Br. Adapted with permission from Ref. [221].

Solar cell devices based on combined halides perovskites with different halide compositions were fabricated and tested under 1 sun illumination by measuring their current-voltage (J - V) characteristics. Samples prepared with Cl precursors yielded higher efficiencies than their counterparts (devoid Cl), this observation was independent of the Br/I ratios. The resulting

trend was induced by an increase in both V_{OC} and a short circuit current, J_{sc} , while the fill factor (FF) remained in the same range. However, by increasing the content of Br, a significant drop of the cell efficiency was observed which was induced by a decrease in the J_{sc} . The decrease in the J_{sc} was attributed to the blue shift of the absorption band edge, as seen in Figure 2.10b. Moreover, devices based on $MAPb(Br_xI_{1-x})_3Cl_y$ employing NS-TiO₂ exhibited lower short circuit current J_{sc} and a lower V_{oc} than devices prepared onto NS-Al₂O₃. Perovskite solar cells with Cl-doped films [206,207] prepared by one-step methodology has been reported to have attained the highest efficiencies of 15%, while the Cl-free devices attained a maximum efficiency of 9.7% [222]. This observation inspired the exploitation of perovskite solar cells with mixed halides for high performing devices. In spite of the fact that the previously reported work in literature focused on the thin-film devices based on bihalide structures (I-Cl, Br-Cl, or I-Br), B. Suarez et al reported for the first time a combination of three halides (Cl, Br, and I) in complete perovskite devices. With addition of Br content, a shift to shorter wavelengths was observed on the ICPE onset. This observation correlated with the absorption measurements shown in Figure 2.10b for all sample sets studied.

2.5.4 Bandgap engineering of lead halide perovskites using a sequential deposition process for planar heterojunction (PHJ) solar cells

The adaptation of a sequential deposition process to tune the band-gap of a organometallic mixed halide perovskite sensitizer was reported by Sneha A. Kulkarni et al [223]. Lead iodide (PbI₂) film was first deposited onto a mesoporous (mp)-TiO₂/bl-TiO₂/FTO substrate, annealed and dipped into mixed methylammonium iodide (MAI)/methylammonium bromide (MABr) which was also followed by subsequent annealing to produce mixed halide perovskites. Two different methods were employed in the sequential deposition process to tune the bandgap of the mixed halide perovskites: first by fixing the molar ratio of the mixed halide (*i.e.* MAI : MABr) solution whilst varying the dipping time (from 30s to 20 minutes) of the PbI₂ film, and secondly by varying the molar ratios of the mixed halide solutions while the time for dipping the PbI₂ was kept constant.

The band gap of the triiodide perovskite MAPbI_3 (formed by dipping PbI_2) was noted to remain invariant at 1.56 eV against the dipping time, and the bandgap value was consistent with earlier reports. A band-gap variation from 1.69 to 1.82 eV was observed at different time intervals for PbI_2 films dipped in the 1:1 mixture of MAI : MABr. A subsequent stabilization of band-gap at 1.75 eV was observed after 20 minutes of dipping time, this could be due to perovskite formation at a particular time interval (15 to 20 min) which depends upon the contribution of X (X= I&Br) as well as the X position in the octhedra. Remarkably, dip coating of PbI_2 films in pure MABr to form perovskite films resulted in a clear blue shift in the absorption band-edge for different time intervals. Perovskite films formed at 0.5 min, 5 min, 10 min & 20 min dipping time intervals showed absorption edge of 660 nm, 635 nm, 625 nm & 556 nm equivalents to bandgaps of 1.89 eV, 1.92 eV, 1.98 eV & 2.23 eV. Therefore the observed shift in bandgap to wider band-gap regions in response to dipping time indicated the possibility to tune the bandgap by controlling the composition of the halides precursors and changing the dipping time interval of the PbI_2 film in the precursor solution.

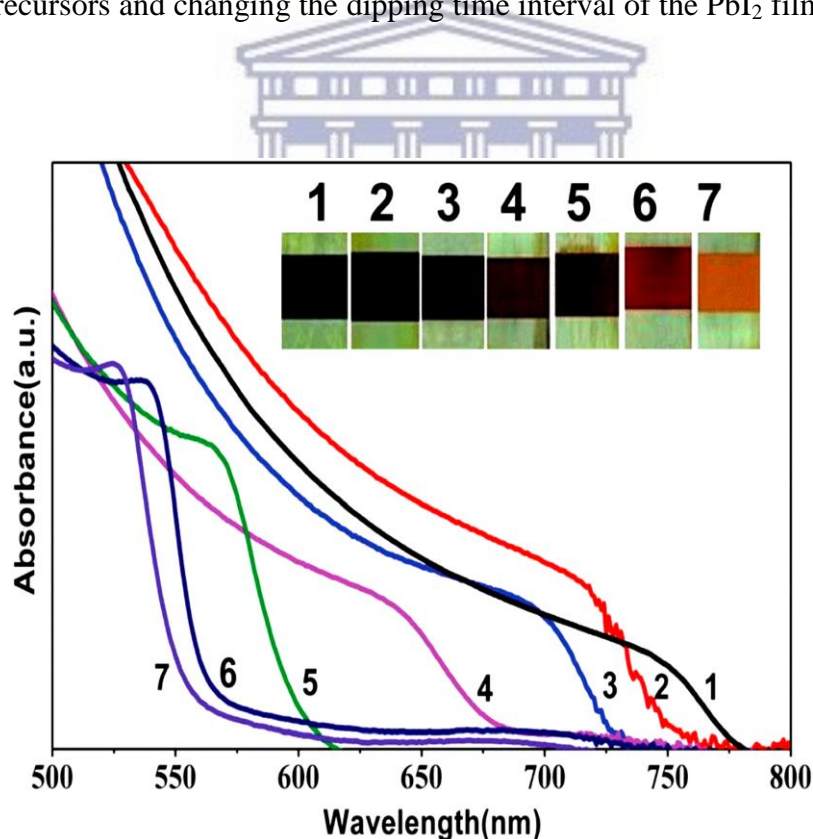


Figure 2.11: UV-Vis absorption spectra of the mixed halide lead perovskite ($\text{MAPb}(\text{I}_{1-x}\text{Br}_x)_3$ ($0 \leq x \leq 1$) films formed via a sequential deposition process. The numbers 1 – 7 correspond to the mixed lead halide perovskite films with different halide (iodide/bromide) compositions. The inset shows the photograph of mixed lead halide nanocomposite perovskite films on FTO substrates. Adapted with permission from Ref. [223].

The effect of concentration at a fixed time interval of 20 minutes was also evaluated by dipping PbI_2 films into various molar compositions of the halide precursor solutions (*i.e.* varying the volume ration of MAI and MABr of known concentration). A shift in absorption onset from 794 nm (1.57 eV) for pure iodide based perovskite to lower wavelength of 556 nm (2.23 eV) for the bromide rich mixed halide based perovskite was observed with an increase in MABr content, as shown in Figure 2.11. Resultantly, a change in colour from dark brow/black to red to orange (Figure 2.11, inset of photograph 1 to 7) of perovskite films was observed with an increase in bromide content. Photovoltaic devices fabricated with MAPbI_3 and $\text{MAPb}(\text{I}_{0.05}\text{Br}_{0.95})_3$ attained efficiencies of 12.04% and 1.58%, respectively. An increase in perovskite films resulted with a reduction in the J_{sc} which was attributed to the increased bandgap which give rise to blue shift of the absorption onset. A systematic shift towards lower wavelengths with increasing Br content in the perovskite films was clearly shown by IPCE, corroborated by optical measurements.

2.5.5 Band-gap engineering by heterovalent doping of perovskite materials with Bi^{3+} , Au^{3+} , and In^{3+}

This work was first reported by A. L. Abdelhady et al. In this work, an efficient in situ chemical route that attains the controlled incorporation of trivalent cations (Bi^{3+} , Au^{3+} , or In^{3+}) via the exploitation of the reversible solubility behaviour of perovskites was demonstrated [224]. A bandgap tuning (~ 300 meV) was attained with Bi^{3+} incorporation. A successful incorporation of heterovalent dopants into perovskite crystals was attained and the host lattice structure was conserved, opening new opportunities to modulate the electronic and optoelectronic properties of this rapidly evolving class of solution-processed hybrid semiconductor materials. Doping of MAPbX_3 has principally been reported only employing isovalent elements with the anions (I/Cl) [228-231] or with the metal cations $\text{Pb}^{2+}/\text{M}^{2+}$ ($\text{M}^{2+} = \text{Sn}^{2+}$, Sr^{2+} , Cd^{2+} or Ca^{2+}) [232]. The challenge to dope perovskite crystals with heterovalent cations was reflected on the absence of the reports on the heterovalent doping of hybrid trihalide perovskite polycrystalline films. The various trivalent cations that were tried in this work Bi^{3+} (isoelectronic with Pb^{2+}), Au^{3+} , and In^{3+} had tolerance factors 0.889, 0.946, and 0.963, respectively. The values of the respective tolerance factors fall within range (0.75 – 1.00) which is reported to allow the perovskite formation. The variation of the Bi^{3+} concentration had a direct impact on both optical and electronic properties of MAPbBr_3 . The

incorporation of Bi^{3+} as a dopant cation remarkably narrowed the bandgap (~ 300 meV). These results indicated Bi as a potential dopant to narrow the bandgap of hybrid perovskites, as well as iodide perovskite crystals, in the range 1.0 – 1.3 eV which is suitable for single junction solar cells [233]. In situ incorporation of dopants was implemented by adding a mixture of trivalent cations (Bi^{3+} , Au^{3+} , In^{3+}) into a crystallization solution containing a mixture of PbBr_2 and MABr in DMF, and then heating to the required temperature.

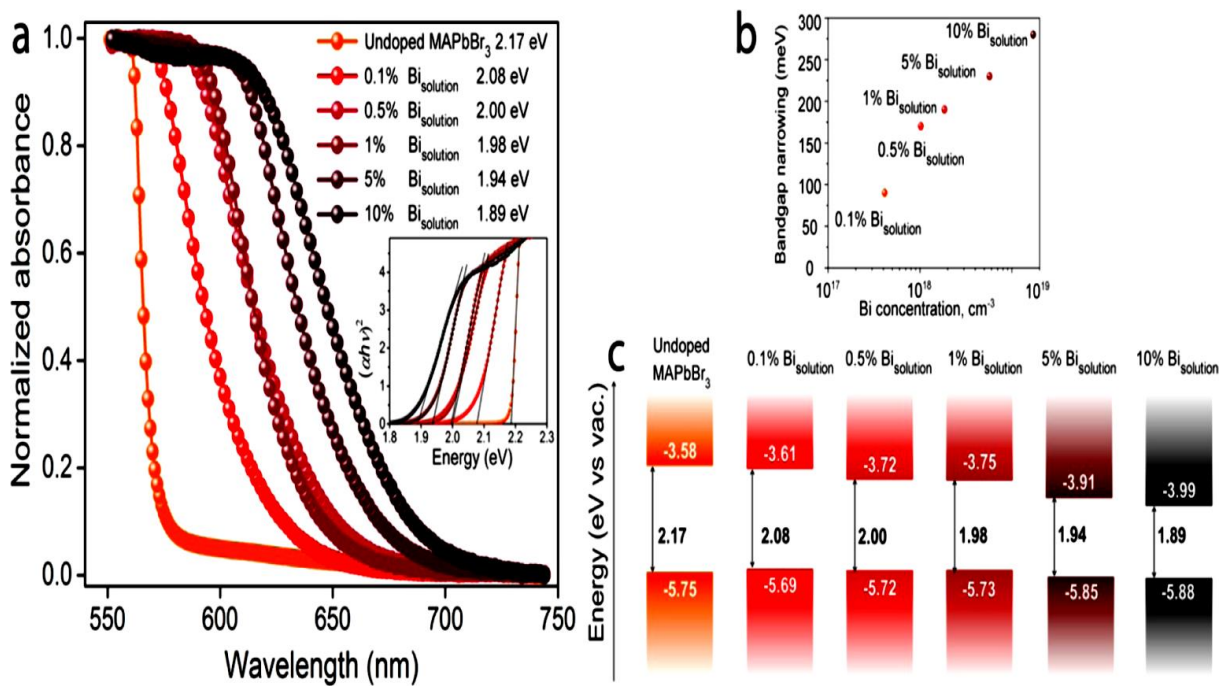


Figure 2.12: (a) Steady-state absorption spectra of MAPbBr₃ crystals with various Bi%. Inset: corresponding Tauc plots. (b) Bandgap narrowing as a function of Bi concentration in the crystal. (c) Bandgap alignment of MAPbBr₃ crystals with various Bi%. Adapted with permission from Ref. [224].

A colour change from orange to deep red was only observed in Bi-doped crystals, but not in other dopants. A colour fading in Au-doped crystals was observed, which could be attributed either to the incorporation of the Au^{3+} or to the reduction of Au^{3+} to Au^+ . Inductively coupled plasma (ICP) traced low content of In^{3+} (0.004%) which was attributed by large difference in ionic radii between lead and indium. X-Ray diffraction measurements confirmed the successful incorporation of heterovalent cations with preservation of the host lattice perovskite structure. A redshift in the absorption edge of the Bi-doped crystal was observed while the In- and Au-doped crystals did not show spectral change from the undoped

crystals. This observation was consistent with previous reports indicating that band gap narrowing (BGN) is dependent on the nature of the dopant [225]. Theoretical studies suggest that the ns^2 electrons play a critical role in bandgap modulation [234], and therefore the Bi-doped crystals were in agreement with these studies. It was shown by density functional theory (DFT) calculations that Au and In create deeper, more localized, and less interacting states than Bi, and this was consistent with the failure to incorporate Au and In to produce significant BGN.

A redshift proportional to the Bi content is shown by the normalized spectra of Bi-doped crystals in Figure 2.12a. BGN as a function of Bi content in the crystals is shown in Figure 2.12b. Lower concentrations of Bi in solution (0.01%) could also result in BGN. A shift in band edge from 570 nm to 680 nm for the undoped crystals in the case of the highest Bi% was observed. The latter wavelength corresponds to a bandgap of 1.89 eV, which was caused by the interaction of the electrons with positive impurities, modifying the density of states [225,226]. The narrowing of bandgap could also be explained by the fact that Bi has a higher electronegativity compared to Pb, which results to more covalent bonding with bromide. This was in good agreement with previously reported studies that a decrease in bandgap from Pb to Sn and Ge due to electronegativity difference [227]. Bi^{3+} incorporation resulted in prolonged carrier lifetime which was determined by nanosecond time-resolved transient absorption experiments. The calculated values for Valence Band Maximum (VBM) and Conduction Band Maximum (CBM) are shown in Figure 2.12c. It was observed from Figure 2.12c that the conduction band moves downward considerably in energy, implying that Bi doping may likely produce n-type semiconductors. In this study, the bandgap of MAPbI_3 was reduced from its intrinsic value of 1.51 eV [224] to as low as 1.28 eV.

2.5.6 Bandgap engineering by incorporation of chalcogenide anions (S & Se) into current triiodide perovskite structure to prepare new mixed ions (organo-chalcogenic) perovskites $\text{CH}_3\text{NH}_3\text{PbI}_2\text{S}$ and $\text{CH}_3\text{NH}_3\text{PbI}_2\text{Se}$ for application in single-junction solar cells

In this study, chalcogenide anions (S & Se) will be incorporated into the structure of the triiodide perovskite to synthesise new perovskite nanomaterials with mixed ions (organo-chalcogenic perovskites): $\text{CH}_3\text{NH}_3\text{PbI}_2\text{S}$ and $\text{CH}_3\text{NH}_3\text{PbI}_2\text{Se}$. A bandgap of organic-inorganic perovskite nanomaterials can be decreased by lowering the Pauling

electronegativity between the metal cation and halide anion (employing least electronegative anions) to improve absorption. It has been shown by experimental studies that the absorption of $\text{CH}_3\text{NH}_3\text{PbX}_3$ shifts to the blue region of the solar spectrum with changing anions from I^- to Br^- to Cl^- (increase in electronegativity from I^- to Cl^-) [139,140]. Pauling electronegativity differences between PbI_2 , PbS , PbSe are calculated as 0.33, 0.25, and 0.22, respectively. A decrease in Pauling electronegativity difference is observed since the electronegativities of all chalcogenide anions S (2.58) and Se (2.55) are all lower than the electronegativity of I_2 (2.66). Therefore incorporation of chalcogenide anions; S & Se, into the triiodide perovskite structure $\text{CH}_3\text{NH}_3\text{PbI}_3$ will result in mixed ions (organo-chalogenic) perovskite nanomaterials; $\text{CH}_3\text{NH}_3\text{PbI}_2\text{S}$, $\text{CH}_3\text{NH}_3\text{PbI}_2\text{Se}$ with lower bandgaps. The incorporation of chalcogenide anions (S & Se) (heterovalent anions, i.e., S^{2-} and Se^{2-} in contrast to I^-) into the structure of triiodide perovskite was inspired by the work done by A. L. Abdelhady et al. whereby band-gap engineering was done by heterovalent doping of perovskite materials with trivalent cations: Bi^{3+} , Au^{3+} , and In^{3+} (in contrast to Pb^{2+}) [224].



BIBLIOGRAPHY

- [1] S. B. Darling, F. Q. You, T. Veselka, and A. Velosa, Assumptions and the levelized cost of energy for photovoltaics, *Energy and Environmental Science*. **4**, 3133–3139 (2011).
- [2] D. Ginley, M. A. Green, and R. Collins, Solar energy conversion toward 1 terawatt, *MRS Bull.* **33**, 355–364 (2008).
- [3] P. Jackson, D. Hariskos, E. Lotter, S. Paetel, and R. Wuerz, New world record efficiency for Cu(In,Ga)Se₂ thin-film solar cells beyond 20%, *Progress in Photovoltaics: Research and Applications*. **19**, 894–897 (2011).
- [4] X. Chen, B. H. Jia, Y. N. Zhang, and M. Gu, Exceeding the limit of plasmonic light trapping in textured screen-printed solar cells using Al nanoparticles and wrinkle-like graphene sheets, *Light: Science and Applications*. **2**, e92 (2013).
- [5] C. J. Hibberd, E. Chassaing, W. Liu, D. B. Mitzi, and D. Lincot, Non-vacuum methods for formation of Cu(In,Ga)(Se,S)₂ thin film photovoltaic absorbers, *Progress in Photovoltaics: Research and Applications*. **18**, 434–452 (2010).
- [6] B. O'Regan and M. Grätzel, A low-cost, high-efficiency solar cell based on dye sensitized colloidal TiO₂ films, *Nature*. **353**, 737–740 (1991).
- [7] A. Yella, H. W. Lee, H. N. Tsao, C. Y. Yi, and A. K. Chandiran, Porphyrin-sensitized solar cells with cobalt (II/III)-based redox electrolyte exceed 12 percent efficiency, *Science*. **334**, 629–634 (2011).
- [8] U. Bach, D. Lupo, P. Comte, J. E. Moser, and F. Weissortel, Solid-state dye-sensitized mesoporous TiO₂ solar cells with high photon-to-electron conversion efficiencies, *Nature*. **395**, 583–585 (1998).

- [9] L. Yang, U. B. Cappel, E. L. Unger, M. Karlsson, and K. M. Karlsson, Comparing spiro-OMeTAD and P3HT hole conductors in efficient solid state dye-sensitized solar cells, *Physical Chemistry Chemical Physics*. **14**, 779–789 (2012).
- [10] W. Zhang, R. Zhu, F. Li, Q. Wang, and B. Liu, High-performance solid-state organic dye sensitized solar cells with P3HT as hole transporter, *The Journal of Physical Chemistry C*. **115**, 7038–7043 (2011).
- [11] S. X. Tan, J. Zhai, M. X. Wan, Q. B. Meng, and Y. L. Li, Influence of small molecules in conducting polyaniline on the photovoltaic of solid-state dye-sensitized solar cells, *The Journal of Physical Chemistry B*. **108**, 18693–18697 (2004).
- [12] K. Murakoshi, R. Kogure, Y. Wada, and S. Yanagida, Fabrication of solid-state dye sensitized TiO₂solar cells combined with polypyrrole, *Solar Energy Materials and Solar Cells*. **55**, 113–125 (1998).
- [13] J. Krüger, R. Plass, L. Cevey, M. Piccirelli, and M. Grätzel, High efficiency solid-state photovoltaic device due to inhibition of interface charge recombination, *Applied Physics Letters*. **79**, 2085–2087 (2001).
- [14] A. Kojima, K. Teshima, Y. Shirai, and T. Miyasaka, Organometal halide perovskites as visible-light sensitizers for photovoltaic cells, *Journal of American Chemical Society*. **131**, 6050–6051 (2009).
- [15] H. S. Kim, C. R. Lee, J. H. Im, K. B. Lee, and T. Moehl, Lead iodide perovskite sensitized all-solid-state submicron thin film mesoscopic solar cell with efficiency exceeding 9%, *Science Reports*. **2**, 591 (2012).
- [16] M. Liu, M. B. Johnston, and H. J. Snaith, Efficient planar heterojunction perovskite solar cells by vapour deposition, *Nature*. **501**, 395–398 (2013).
- [17] K. Wojciechowski, M. Saliba, T. Leijtens, A. Abate, and H. J. Snaith, Sub-150°C processed meso-superstructured perovskite solar cells with enhanced efficiency, *Energy Environ. Sci*. **7**, 1142–1147 (2014).

- [18] J. H. Im, C. R. Lee, J. W. Lee, S. W. Park, and N. G. Park, 6.5% efficient perovskite quantum-dot-sensitized solar cell, *Nanoscale*. **3**, 4088–4093 (2011).
- [19] M. M. Lee, J. Teuscher, T. Miyasaka, T. N. Murakami, and H. J. Snaith, Efficient hybrid solar cells based on mesosuperstructured organometal halide perovskites, *Science*. **338**, 643–647 (2012).
- [20] L. Etgar, P. Gao, Z. S. Xue, Q. Peng, and A. K. Chandiran, Mesoscopic CH₃NH₃PbI₃/TiO₂ heterojunction solar cells, *Journal of the American Chemical Society*. **134**, 17396–17399 (2012).
- [21] S. S. Shin, J. S. Kim, J. H. Suk, K. D. Lee, and D. W. Kim, Improved quantum efficiency of highly efficient perovskite BaSnO₃-based dye-sensitized solar cells, *American Chemical Society Nanotechnology*. **7**, 1027–1035 (2013).
- [22] E. Edri, S. Kirmayer, D. Cahen, and G. Hodes, High open-circuit voltage solar cells based on organic–inorganic lead bromide perovskite, *The Journal of Physical Chemistry Letters*. **4**, 897–902 (2013).
- [23] J. H. Noh, S. H. Im, J. H. Heo, T. N. Mandal, and S. I. Seok, Chemical management for colorful, efficient, and stable inorganic–organic hybrid nanostructured solar cells, *Nano Letters*. **13**, 1764–1769 (2013).
- [24] D. Q. Bi, L. Yang, G. Boschloo, A. Hagfeldt, and E. M. J. Johansson, Effect of different hole transport materials on recombination in CH₃NH₃PbI₃ perovskite-sensitized mesoscopic solar cells, *The Journal of Physical Chemistry Letters*. **4**, 1532–1536 (2013).
- [25] I. Chung, B. H. Lee, J. Q. He, R. P. H. Chang, and M. G. Kanatzidis, All-solid-state dye-sensitized solar cells with high efficiency, *Nature*. **485**, 486–489 (2012).
- [26] H. S. Kim, J. W. Lee, N. Yantara, P. P. Boix, and S. A. Kulkarni, High efficiency solid-state sensitized solar cell-based on submicrometer rutile TiO₂ nanorod and CH₃NH₃PbI₃ perovskite sensitizer, *Nano Letters*. **13**, 2412–2417 (2013).

- [27] A. Abrusci, S. D. Stranks, P. Docampo, H. L. Yip, and A. K. Y. Jen, High performance perovskite-polymer hybrid solar cells via electronic coupling with fullerene monolayers, *Nano Letters*. **13**, 3124–3128 (2013).
- [28] J. M. Ball, M. M. Lee, A. Hey, and H. J. Snaith, Low-temperature processed meso superstructured to thin-film perovskite solar cells, *Energy and Environmental Science*. **6**, 1739–1743 (2013).
- [29] J. Burschka, N. Pellet, S. J. Moon, R. Humphry-Baker, and P. Gao, Sequential deposition as a route to high-performance perovskite-sensitized solar cells, *Nature*. **499**, 316–319 (2013).
- [30] W. Zhang, M. Saliba, S. D. Stranks, Y. Sun, and X. Shi, Enhancement of perovskite based solar cells employing core-shell metal nanoparticles, *Nano Letters*. **13**, 4505–4510 (2013).
- [31] A. Abate, D. J. Hollman, J. Teuscher, S. Pathak, and R. Avolio, Protic ionic liquids as p dopant for organic hole transporting materials and their application in high efficiency hybrid solar cells, *Journal of the American Chemical Society*. **135**, 13538–13548 (2013).
- [32] G. E. Eperon, V. M. Burlakov, P. Docampo, A. Goriely, and H. J. Snaith, Morphological control for high performance, solutionprocessed planar heterojunction perovskite solar cells, *Advanced Functional Materials*. **24**, 151–157 (2014).
- [33] D. Q. Bi, S. J. Moon, L. Häggman, G. Boschloo, and L. Yang, Using a two-step deposition technique to prepare perovskite (CH₃NH₃PbI₃) for thin film solar cells based on ZrO₂ and TiO₂ mesostructures, *RSC Advances*. **3**, 18762–18766 (2013).
- [34] J. H. Qiu, Y. C. Qiu, K. Y. Yan, M. Zhong, and C. Mu, All-solidstate hybrid solar cells based on a new organometal halide perovskite sensitizer and one-dimensional TiO₂ nanowire arrays, *Nanoscale*. **5**, 3245–3248 (2013).
- [35] D. Q. Bi, G. Boschloo, S. Schwarzmüller, L. Yang, and E. M. J. Johansson, Efficient and stable CH₃NH₃PbI₃-sensitized ZnO nanorod array solid-state solar cells, *Nanoscale*. **5**,

11686–11691 (2013).

[36] J. A. Christians, R. C. M. Fung, and P. V. Kamat, An inorganic hole conductor for organo-lead halide perovskite solar cells. Improved hole conductivity with copper iodide, *Journal of the American Chemical Society*. **136**, 758–764 (2014).

[37] N. JoongJeon, J. Lee, J. H. Noh, M. K. Nazeeruddin, and M. Grätzel, Efficient inorganic–organic hybrid perovskite solar cells based on pyrenearylamine derivatives as hole-transporting materials, *Journal of the American Chemical Society*. **135**, 19087–19090 (2013).

[38] T. M. Koh, K. W. Fu, Y. N. Fang, S. Chen, and T. C. Sum, Formamidinium-containing metal-halide: an alternative material for near-IR absorption perovskite solar cells, *The Journal of Physical Chemistry C*. **118**, 16458–16462 (2014).

[39] B. Conings, L. Baeten, C. D. Dobbelaere, J. D’Haen, and J. Manca, Perovskite-based hybrid solar cells exceeding 10% efficiency with high reproducibility using a thin film sandwich approach, *Advanced Materials*. **26**, 2041–2046 (2014).

[40] J. T. W. Wang, J. M. Ball, E. M. Barea, A. Abate, and J. A. Alexander-Webber, Low-temperature processed electron collection layers of Graphene/TiO₂ nanocomposites in thin film perovskite solar cells, *Nano Letters*. **14**, 724–730 (2014).

[41] Q. Chen, H. P. Zhou, Z. R. Hong, S. Luo, and H. S. Duan, Planar heterojunction perovskite solar cells via vapor-assisted solution process, *Journal of the American Chemical Society*. **136**, 622–625 (2014).

[42] D. Y. Liu and L. Kelly, Perovskite solar cells with a planar heterojunction structure prepared using room-temperature solution processing techniques, *Nature Photonics*. **8**, 133–138 (2014).

[43] G. E. Eperon, S. D. Stranks, C. Menelaou, M. B. Johnston, and L. M. Herz, Formamidinium lead trihalide: a broadly tunable perovskite for efficient planar heterojunction solar cells, *Energy and Environmental Science*. **7**, 982–988 (2014).

[44] J. B. You, Z. R. Hong, Y. Yang, Q. Chen, and M. Cai, Low-temperature solution processed perovskite solar cells with high efficiency and flexibility, *ACS Nanotechnology*. **8**, 1674–1680 (2014).

[45] A. Kojima, M. Ikegami, K. Teshima, and T. Miyasaka, Highly luminescent lead bromide perovskite nanoparticles synthesized with porous alumina media, *Chemistry Letters*. **41**, 397 (2012).

[46] C. I. Covaliu, L. C. Chioaru, L. Crăciun, O. Oprea, and I. Jitaru, Electrical properties of new organo-inorganic layered perovskites, *Optoelectronics and Advanced Materials*. **5**, 1097 (2012).

[47] C. R. Kagan, D. B. Mitzi, and C. D. Dimitrakopoulos, Organic-inorganic hybrid materials as semiconducting channels in thin film field-effect transistors, *Science*. **286**, 945 (1999).

[48] D. B. Mitzi, C. A. Feild, Z. Schlesinger, and R. B. Laibowitz, Transport, Optical, and Magnetic Properties of the Conducting Halide Perovskite $\text{CH}_3\text{NH}_3\text{SnI}_3$, *Journal of Solid State Chemistry*. **114**, 159 (1995).

[49] G. Hodes, Perovskite-based solar cells, *Science*. **342**, 317–318 (2013).

[50] H.S Kim, C. R. Lee, J. H. Im, K. B. Lee, T. Moehl, A. Marchioro, S. J. Moon, R. Humphry-Baker, J. H. Yum, J. E. Moser, M. Grätzel, and N. G. Park, Lead iodide perovskite sensitized all-solid-state submicron thin film mesoscopic solar cell with efficiency exceeding 9%, *Science Reports*. **2**, 591 (2012).

[51] M.Z. Liu, M.B Johnston, and H.J Snaith, Efficient planar heterojunction perovskite solar cells by vapour deposition, *Nature*. **501**, 395 (2013).

[52] J. Burschka, N. Pellet, S. J Moon, R. Humphry-Baker, P. Gao, M. K. Nazeeruddin, and M. Grätzel, Sequential deposition as a route to high-performance perovskite solar cells, *Nature*, **499**, 316 (2013).

[53] M. M. Lee, J. Teuscher, T. Miyasaka, T. N. Murakami, and H. J. Snaith, Efficient hybrid solar cells based on meso-superstructured organometal halide perovskites, *Science*. **338**, 643 (2012).

[54] W. Shockley, and H. J. Queisser, Detailed Balance Limit of Efficiency of p-n Junction Solar Cells*. *Journal of Applied Physics*. **32**, 510 (1961).

[55] H. J. Snaith, Perovskites: The Emergence of a New Era for Low-Cost, High-Efficiency Solar Cells, *The Journal of Physical Chemistry Letters*. **4**, 3623 (2013).

[56] N. G. Park, Perovskites: The Emergence of a New Era for Low-Cost High Efficiency Solar Cells, *The Journal of Physical Chemistry Letters*. **4**, 2423 (2013).

[57] G. Hodes, Perovskite-Based Solar Cells, *Science*. **342**, 317 (2013).

[58] T. Baikie, Y. Fang, J. M. Kadro, M. Schreyer, F. Wei, S. G. Mhaisalkar, M. Graetzel, and T. J. White, Synthesis and crystal chemistry of the hybrid perovskite (CH₃NH₃)PbI₃ for solid-state sensitized solar cell applications, *Journal of Materials Chemistry A*. **1**, 5628 (2013).

[59] C. Ziyong and Jun Lin, Layered organic-inorganic hybrid perovskite: structure, optical properties, film preparation, patterning and templating engineering. *Crystal Engineering Communications*. **12**, 2646 (2010).

[60] Y. Kawamura, H. Mashiyama, and K. Hasebe, Structural study on Cubic-Tetragonal Transition of CH₃NH₃PbI₃, *Journal of the Physical Society of Japan*. **71**, 1694 (2002).

[61] D. B. Mitzi, C. A. Field, Z. Schlesinger, and R. B. Laibowitz, Transport, optical, and magnetic properties of the conducting halide perovskite CH₃NH₃SnI₃, *Journal of Solid State Chemistry*. **114**, 159–163 (1995).

[62] O. Knop, R. E. Wasylshen, M. A. White, T. S. Cameron, and M. J. M. V. Oort, Alkylammonium lead halides. Part 2. CH₃NH₃PbX₃ (X = Cl, Br, I) perovskites:

cuboctahedral halide cages with isotropic cation reorientation, *Canadian Journal of Chemistry*. **68**, 412–422 (1990).

[63] C. C. Stoumpos, C. D. Malliakas, and M. G. Kanatzidis, Semiconducting tin and lead iodide perovskites with organic cations: phase transitions, high mobilities, and near-infrared photoluminescent properties, *Inorganic Chemistry*. **52**, 9019–9038 (2013).

[64] A. Poglitsch and D. Weber, Dynamic disorder in methyl ammonium trihalogenoplumbates (II) observed by millimeter-wave spectroscopy, *The Journal of Chemical Physics*. **87**, 6373–6378 (1987).

[65] K. Shum, Z. Chen, J. Qureshi, C. L. Yu, and J. J. Wang, Synthesis and characterization of CsSnI₃ thin films, *Applied Physics Letters*. **96**, 221903 (2010).

[66] K. Yamada, Y. Kuranaga, K. Ueda, S. Goto, and T. Okuda, Phase transition and electric conductivity of A₂SnCl₃ (A = Cs and CH₃NH₃), *Bulletin of the Chemical Society of Japan*. **71**, 127–134 (1998).

[67] I. Borriello, G. Cantele, and D. Ninno, Ab initio investigation of hybrid organic inorganic perovskites based on tin halides, *Physical Review*. **B 77**, 235214 (2008).

[68] V. M. Goldschmidt, Crystal Structure and Chemical Combination. *Berichte der Deutschen Chemischer Gesellschaft*. **60**, 1263–1268 (1927).

[69] *Inorganic Solid Fluorides: Chemistry and Physics*; P. Hagenmuller, Ed.; Materials Science Series; Academic Press: London, (1985).

[70] C. Li, K. C. K. Soh, P. Wu, Formability of ABO₃ Perovskites. *Journal of Alloys and Compounds*. **372**, 40–48 (2004).

[71] C. Li, X. Lu, W. Ding, L. Feng, Y. Gao, Z. Guo, Formability of ABX₃ (X = F, Cl, Br, I) Halide Perovskites. *Acta Crystallographica*. **B64**, 702–707 (2008).

[72] G. Alagona, C. Ghio, P. Kollman, Monte Carlo Simulation Studies of the Solvation of Ions. 1. Acetate Anion and Methylammonium Cation. *Journal of the American Chemical Society*. **108**, 185–191(1986).

[73] R. D. Shannon, Revised Effective Ionic Radii and Systematic Studies of Interatomic Distances in Halides and Chalcogenides. *Acta Crystallographica*. **A32**, 751–767 (1976).

[74] E. J. Gabe, The Crystal Structure of Methyl Ammonium Bromide. *Acta Crystallographica*. **14**, 1296 (1961).

[75] B. N. Cohen, C. Labarca, N. Davidson, H. A. Lester, Mutations In M2 Alter: The Selectivity of the Mouse Nicotinic Acetylcholine Receptor for Organic and Alkali Metal Cations. *The Journal of General Physiology*. **100**, 373–400 (1992).

[76] L. Q. Jianga, J. K. Guob, H. B. Liua, M. Zhua, X. Zhoua, P. Wuc, C. H. Li, Prediction of Lattice Constant in Cubic Perovskites. *Journal of Physics and Chemistry of Solids*. **67**, 1531–1536 (2006).

[77] U. Shirwadkar, E. V. D. van Loef, R. Hawrami, S. Mukhopadhyay, J. Glodo, K. S. Shah, New promising scintillators for gamma-ray spectroscopy: Cs(Ba,Sr) (Br,I)₃. *IEEE NSS/MIC Conference*. 1583–1585 (2011).

[78] S. Hesse, J. Zimmermann, H. von Seggern, H. Ehrenberg, H. Fuess, C. Fasel, R. Riedel, CsEuBr₃: Crystal structure and its role in the photostimulation of CsBr:Eu²⁺, *Journal of Applied Physics*. **100**, 083506 (2006).

[79] A. Horowitz, M. Amit, J. Makovsky, L. B. Dor, Z. H. Kalman, Structure types and phase transformations in KMnCl₃ and TlMnCl₃. *Journal of Solid State Chemistry*. **43**, 107–125 (1982).

[80] I. B. Koutselas, L. Ducasse and G. C. Papavassiliou, Electronic properties of three-and low-dimensional semiconducting materials with Pb halide and Sn halide units, *Journal of Physics: Condensed Matter*. **8**, 1217–1227 (1996).

- [81] T. Umebayashi, K. Asai, T. Kondo and A. Nakao, Electronic structure of lead iodide based low-dimensional crystals, *Physical Reviews B: Condensed Matter and Materials Physics*. **67**, 155405 (2003).
- [82] Y. H. Chang, C. H. Park and K. Matsuishi, First-Principles Study of the Structural and Electronic Properties of the Lead-Halide-Based Inorganic-Organic Perovskites $(\text{CH}_3\text{NH}_3)\text{PbX}_3$ and CsPbX_3 ($X = \text{Cl}, \text{Br}, \text{I}$), *Journal of the Korean Physical Society*. **44**, 889–893 (2004).
- [83] E. Mosconi, A. Amat, M. K. Nazeeruddin, M. Gratzel and F. De Angelis, First-Principles Modelling of Mixed Halide Organometal Perovskites for Photovoltaic Applications, *Journal of Physical Chemistry C*. **117**, 13902–13913 (2013).
- [84] T. Baikie, Y. N. Fang, J. M. Kadro, M. Schreyer, F. X. Wei, S. G. Mhaisalkar, M. Gratzel and T. J. White, Synthesis and crystal chemistry of the hybrid perovskite $(\text{CH}_3\text{NH}_3)\text{PbI}_3$ for solid-state sensitized solar cell application, *Journal of Materials Chemistry A*. **1**, 5628–5641 (2013).
- [85] Y. Wang, T. Gould, J. F. Dobson, H. Zhang, H. Yang, X. Yao, and H. Zhao, Density functional theory analysis of structural and electronic properties of orthorhombic perovskite $\text{CH}_3\text{NH}_3\text{PbI}_3$ *Physical Chemistry Chemical Physics*. **16**, 1424–1429 (2014).
- [86] R. Ito, S. Hayase, T. Kondo, S. Iwamoto, K. Ema, H. Kunugita, M. Mizuno and J. Ishi, Third-Order Optical Nonlinear Due to Exciton and Bi-exciton in a self-organised Quantum-Well Material $(\text{C}_6\text{H}_5\text{C}_2\text{H}_4\text{NH}_3)_2\text{PbI}_4$, *Journal of Nonlinear Optical Physics Materials*. **07**, 153–159 (1998).
- [87] M. Shimizu and J.-I. Fujisawa, Exciton-exciton interaction in an inorganic-organic layered semiconductor, $(\text{C}_6\text{H}_5\text{C}_2\text{H}_4\text{NH}_3)_2\text{PbI}_4$, *Journal of Luminescence*. **108**, 189–194 (2004).
- [88] J. Ishi, H. Kunugita, K. Ema, T. Ban and T. Kondo, Influence of exciton-exciton interactions on frequency-mixing signals in a stable exciton-biexciton system, *Physical Review. B: Condensed Matter and Materials Physics*. **63**, 073303 (2001).

[89] N. Kitazawa, M. Aono and Y. Watanabe, Temperature-dependent time-resolved photoluminescence of $(\text{C}_6\text{H}_5\text{C}_2\text{H}_4\text{NH}_3)_2\text{PbI}_4$, *Materials Chemistry and Physics*. **134**, 875–880 (2012).

[90] M. Hirasawa, T. Ishihara and T. Goto, Exciton Features in 0-, 2-, and 3-Dimensional Networks of $[\text{PbI}_6]^{4-}$ octahedral, *Journal of the Physical Society of Japan*. **63**, 3870–3879 (1994).

[91] X. Hong, T. Ishihara and A. V. Nurmikko, Dielectric confinement effect on excitons in PbI_4 -based layered semiconductors, *Physical Reviews B: Condensed Matter and Materials Physics*. **45**, 6961–6964 (1992).

[92] J. F. Muth, J. H. Lee, I. K. Shmagin, R. M. Kolbas, H. C. Casey, B. P. Keller, U. K. Mishra and S. P. DenBaars, Absorption coefficient, energy gap, exciton binding energy, and recombination life time of GaN obtained from transmission measurements, *Applied Physics Letters*. **71**, 2572–2574 (1997).

[93] S. J. Zhang, P. Audebert, Y. Wei, A. Al Choueiry, G. Lanty, A. Brehier, L. Galmiche, G. Clavier, C. Boissiere, J. S. Lauret and E. Deleporte, Preparations and Characterization of Luminescent Two Dimensional Organic-inorganic Perovskite Semiconductors, *Materials*. **3**, 3385–3406 (2010).

[94] K. Tanaka, T. Takahashi, T. Ban, T. Kondo, K. Uchida and N. Miura, Comparative study on the excitons in Lead-halide-based perovskite-type crystals $\text{CH}_3\text{NH}_3\text{PbBr}_3$ $\text{CH}_3\text{NH}_3\text{PbI}_3$, *Solid State Communications*. **127**, 619–623 (2003).

[95] Z. Chen, C. L. Yu, K. Shum, J. J. Wang, W. Pfenninger, N. Vockic, J. Midgley and J. T. Kenney, Photoluminescence study of polycrystalline CsSnI_3 thin films: Determination of exciton binding energy, *Journal of Luminescence*. **132**, 345–349 (2012).

[96] H. S. Kim, C. R. Lee, J. H. Im, K. B. Lee, T. Moehl, A. Marchioro, S. J. Moon, R. Humphry-Baker, J. H. Yum, J. E. Moser, M. Gratzel and N. G. Park, Lead iodide perovskite

sensitized all-solid-state submicron thin film mesoscopic solar cell with efficiency exceeding 9%, *Science Reports*. **2**, 591 (2012).

[97] M. Hirasawa, T. Ishihara, T. Goto, K. Uchida and N. Miura, Magnetoabsorption of the lowest exciton in perovskite-type compound $(\text{CH}_3\text{NH}_3)\text{PbI}_3$, *Physica B*. **201**, 427–430 (1994).

[98] T. Ishihara, Optical properties of PbI-based perovskite structures, *Journal of Luminescence*. **60-1**, 269–274 (1994).

[99] S. Sun, T. Salim, N. Mathews, M. Duchamp, C. Boothroyd, G. Xing, T. C. Sum and Y. M. Lam, The origin of high efficiency in low-temperature solution-processable bilayer organometal halide hybrid solar cells, *Energy and Environmental Science*. **7**, 399–407 (2014).

[100] W. Zhang, M. Saliba, S. D. Stranks, Y. Sun, X. Shi, U. Wiesner and H. J. Snaith, Enhancement of Perovskite-Based Solar Cells Employing Core-Shell Metal Nanoparticles. *Nano Letters*. **13**, 4505–4510 (2013).

[101] F. Deschler, M. Price, S. Pathak, L. E. Klintberg, D. Jarausch, R. Higler, S. Hüttner, T. Leijtens, S. D. Stranks, H. J. Snaith, M. Atatüre, R. T. Phillips, and R. H. Friend, High Photoluminescence Efficiency and Optically Pumped Lasing in Solution-Processed Mixed Halide Perovskite Semiconductors, *Journal of Physical Chemistry Letters*. **5**, 1421 (2014).

[102] B. R. Sutherland, S. Hoogland, M. M. Adachi, C. T. O. Wong, and E. H. Sargent, Conformal Organohalide Perovskite Enable Lasing on Spherical Resonators, *ACS Nano*. **8**, 10947 (2014).

[103] Z.-K. Tan, R. S. Moghaddam, M. L. Lai, P. Docampo, R. Higler, F. Deschler, M. Price, A. Sadhanala, L. M. Pazos, D. Credgington, F. Hanusch, T. Bein, H. J. Snaith, and R. H. Friend, Bright Light-emitting diodes based on organometal halide perovskite, *Nature Nanotechnology*. **9**, 687 (2014).

- [104] G. Xing, N. Mathews, S. S. Lim, N. Yantara, X. Liu, D. Sabba, M. Grätzel, S. Mhaisalkar, and T. C. Sum, Low temperature solution-processed wavelength-tuneable perovskites for lasing, *Nature Materials*. **13**, 4076 (2014).
- [105] Y. Yamada, T. Nakamura, M. Endo, A. Wakamiya, and Y. Kanemitsu, Photocarrier Recombination Dynamics in Perovskite $\text{CH}_3\text{NH}_3\text{PbI}_3$ for Solar Cell Applications, *Journal of American Chemical Society*. **136**, 11610 (2014).
- [106] S. D. Stranks, V. M. Burlakov, T. Leijtens, J. M. Ball, A. Goriely, and H. J. Snaith, Recombination Kinetics in Organic-inorganic Perovskite: Excitons, Free Charge, and Subgap States, *Physical Review Applied*. **2**, No. 034007 (2014).
- [107] M. Saba, M. Cadelano, D. Marongiu, F. Chen, V. Sarritzu, N. Sestu, C. Figus, M. Aresti, R. Piras, A. Geddo Lehmann, C. Cannas, A. Musinu, F. Quochi, A. Mura, and G. Bongiovanni, Correlated electron-hole plasma in organometal perovskite, *Nature Communications*. **5**, No. 5049 (2014).
- [108] J. S. Manser, and P. V. Kamat, Band filling with free charge carriers in organometal halide perovskite, *Nature Photonics*. **8**, 737 (2014).
- [109] S. D. Stranks, G. E. Eperon, G. Grancini, C. Menelaou, M. J. P. Alcocer, T. Leijtens, L. M. Herz, A. Petrozza, and H. J. Snaith, Correlated electron-hole plasma in organometal perovskite, *Nature Communications*. **342**, 341 (2013).
- [110] G. Grancini, S. Marras, M. Prato, C. Giannini, C. Quarti, F. De Angelis, M. De Bastiani, G. E. Eperon, H. J. Snaith, L. Manna, and A. Petrozza, The impact of the Crystallization Processes on the Structural and Optical Properties of Hybrid Perovskite Films for Photovoltaics, *Journal of Physical Chemistry Letters*. **5**, 3836 (2014).
- [111] J.-H. Im, I.-H. Jang, N. Pellet, M. Grätzel, and N.-G. Park, Growth of $\text{CH}_3\text{NH}_3\text{PbI}_3$ cuboids with controlled size for high-efficiency perovskite solar cells, *Nature Nanotechnology*. **9**, 927 (2014).

[112] M. De Bastiani, V. D’Innocenzo, S. D. Stranks, H. J. Snaith, and A. Petrozza, Role of the crystallization substrate on the photoluminescence properties of organo-lead mixed halide perovskites, *APL Materials*. **2**, No. 081509 (2014).

[113] D. Bi, S.-J. Moon, L. Häggman, G. Boschloo, L. Yang, E. M. K. Johansson, Nazeeruddin, M. Grätzel, and A. Hagfeldt, Using a two steps deposition technique to prepare perovskite ($\text{CH}_3\text{NH}_3\text{PbI}_3$) for thin film solar cells based on ZrO_2 and TiO_2 mesostructures, *RSC Advances*. **3**, 18762 (2013).

[114] J. Burschka, N. Pellet, S. -J Moon, R. Humphry-Baker, P. Gao, M. K. Nazeeruddin, and M. Grätzel, Sequential deposition as a route to high-performance perovskite sensitized solar cells, *Nature*. **499**, 316 (2013).

[115] P. Docampo, F. Hanusch, S. D. Stranks, M. Döblinger, J. M. Feckl, M. Ehrensperger, N. K. Minar, M. B. Johnston, H. J. Snaith, and T. Bein, Solution Deposition-Conversion for Planar Heterojunction Mixed Halide Perovskite Solar Cells, *Advanced Energy Materials*. **4**, No. 1400355 (2014).

[116] G. Xing, N. Mathews, S. Sun, S. S. Lim, Y. M. Lam, M. Grätzel, S. Mhaisalkar, and T. C. Sum, Long-Range Balanced Electron and Hole-Transport lengths in Organic-inorganic $\text{CH}_3\text{NH}_3\text{PbI}_3$, *Science*. **342**, 344 (2013).

[117] V. Roiati, S. Colella, G. Lerario, L. De Marco, A. Rizzo, A. Listorti, and G. Gigli, Investigating charge dynamics in halide perovskite sensitized mesostructured solar cells *Energy and Environmental Science*. **7**, 1889 (2014).

[118] V. D’Innocenzo, A. R. S. Kandada, M. De Bastiana, M. Gandini, and A. Petrozza, Tuning the Light Emission Properties by Band Gap Engineering in Hybrid Lead Halide Perovskite, *Journal of American Chemical Society*. **136**, 17730 – 1773 (2014).

[119] C. Jordan, J. F. Donegan, J. Hegarty, B. J. Roycroft, S. Taniguchi, T. Hino, E. Kato, N. Noguchi, and A. Ishibashi, Carrier-density dependence of the photoluminescence lifetimes in $\text{ZnCdSe}/\text{ZnSSe}$ quantum wells at room temperature, *Applied Physics Letters*. **74**, 3359 (1999).

[120] C. C. Stoumpos, C. D. Malliakas, and M. G. Kanatzidis, Semiconducting Tin and Lead iodide Perovskite with Organic Cations: Phase Transitions, High Mobilities, and Near-Infrared Photoluminescence Properties, *Inorganic Chemistry*. **52**, 9019 (2013).

[121] Y. P. Varshni, Temperature dependence of the energy gap in semiconductors, *Physica*. **34**, 149 (1967).

[122] V. D' Innocenzo, G. Grancini, M. J. P. Alcocer, A. R. S. Kandada, S. D. Stranks, M. M. Lee, G. Lanzani, H. J. Snaith, and A. Petrozza, Excitons versus free charges in organolead tri-halide perovskite, *Nature Communications*. **5**, No. 3586 (2014).

[123] Z. Y. Cheng and J. Lin, Layered organic-inorganic hybrid perovskite: structure, optical properties, film preparations, patterning and templating engineering, *Crystal Engineering Communications*. **21**, 2646 (2010).

[124] N. Kitazawa, K. Enomoto, M. Aono, and Y. Watanabe, Optical properties of $(\text{C}_6\text{H}_5\text{C}_2\text{H}_4\text{NH}_3)_2\text{PbI}_{4-x}\text{Br}_x$ ($x = 0 - 4$) mixed-crystal doped PMMA films. *Journal of Materials Science*. **39**, 749 (2004) .

[125] J. Burschka, N. Pellet, S. J. Moon, R. Humphry-Baker, P. Gao, M. K. Nazeeruddin, and M. Grätzel, Sequential deposition as a route to high-performance perovskite-sensitized solar cells, *Nature*. **499**, 316 (2013).

[126] K. N. Liang, D. B. Mitzi, and M. T. Prikas, Synthesis and characterization of Organic-Inorganic Perovskite Thin Films Prepared Using a Versatile Two-step Dipping Technique, *Chemistry of Materials*. **10**, 403 (1998).

[127] K. Pradeesh, J. J. Baumberg, and G. V. Prakash, *In situ* intercalation strategies for device-quality hybrid inorganic-organic self-assembled quantum wells, *Applied Physics Letters*. **95**, 173305 (2009).

[128] D. Q. Bi, S.-J. Moon, L. Häggman, G. Boschloo, L. Yang, E. M. J. Johansson, M. K. Nazeeruddin, M. Grätzel, and A. Hagfeldt, Using a two-step deposition technique to prepare perovskite ($\text{CH}_3\text{NH}_3\text{PbI}_3$) for thin film solar cells based on ZrO_2 and TiO_2 mesosuperstructures, *RSC Adv.* **3**, 18762 (2013).

[129] Y. N. Xia and G. M. Whitesides, SOFT LITHOGRAPHY, *Annual Reviews: Materials Science.* **28**, 153 (1998).

[130] Q. Chen, H. Zhou, Z. Hong, S. Luo, H.-S. Duan, H.-H. Wang, Y. Liu, G. Li, and Y. Yang, Planar heterojunction perovskite solar cells via vapour-assisted solution process, *Journal of American Chemical Society.* **136**, 622 (2014).

[131] G. E. Eperon, S. D. Stranks, C. Menelaou, M. B. Johnston, L. M. Herz, and H. J. Snaith, Formamidinium lead trihalide: A broadly tunable perovskite for efficient planar heterojunction solar cells. *Energy and Environmental Science.* **7**, 982–988 (2014).

[132] J. L. Knutson, J. D. Martin, and D. B. Mitzi, Tuning the bandgap in hybrid tin iodide perovskite semiconductors using structural templating, *Inorganic Chemistry.* **44**, 4699–4705 (2005).

[133] Y. Ogomi et al. $\text{CH}_3\text{NH}_3\text{Sn}_x\text{Pb}_{(1-x)}\text{I}_3$ perovskite solar cells covering up to 1060 nm. *Journal of the Physical Chemistry Letters.* **5**, 1004–1011 (2014).

[134] I. Borriello, G. Cantele, D. Ninno, Ab initio investigation of hybrid organic-inorganic perovskite based on tin halides, *Physical Reviews B: Condensed Matter Materials Physics.* **77**, 235214 (2008).

[135] Q. Dong, Y. Fang, Y. Shao, P. Mulligan, J. Qiu, L. Cao, J. Huang, Electron-hole diffusion lengths $> 175 \mu\text{m}$ in solution-grown $\text{CH}_3\text{NH}_3\text{PbI}_3$ single crystals, *Science.* **347**, 967–970 (2015).

- [136] N. J. Jeon, J. H. Noh, W. S. Yang, Y. C. Kim, S. Ryu, J. Seo, S. I. Seok, Compositional engineering of perovskite materials for high performance solar cells, *Nature*. **517**, 476–480 (2015).
- [137] Y. Li, X. P. Gao, G. R. Li, G. L. Pan, T. Y. Yan, H. Y. Zhu, Titanate nanofiber reactivity: Fabrication of MTiO_3 ($M = \text{Ca}, \text{Sr}, \text{and Ba}$) perovskite oxides, *Journal of Physical Chemistry C*, **113**, 4386–4394 (2009).
- [138] S. R. Basu, L. W. Martin, Y. H. Chu, M. Gajek, R. Ramesh, R. C. Cai, J. L. Musfeldt, Photoconductivity in BiFeO_3 thin films, *Applied Physics Letters*. **92**, 091905 (2008).
- [139] S. A. Kulkarni, T. Baikie, P. P. Boix, N. Yantara, N. Mathews, S. Mhaisalkar, Band-gap tuning of lead halide perovskite using a sequential deposition process, *Journal of Materials Chemistry*. **2**, 9221–9225 (2014).
- [140] G. Xing, N. Mathews, S. Sun, S. S. Lim, Y. M. Lam, M. Grätzel, S. Mhaisalkar, T. C. Sum, Long-range balanced electron- and hole-transport lengths in organic-inorganic $\text{CH}_3\text{NH}_3\text{PbI}_3$, *Science*. **342**, 344–347 (2013).
- [141] I. P. Swainson, R. P. Hammond, C. Souliere, O. Knop, W. Massa, *Journal of Solid State Chemistry*. **176**, 97 (2003).
- [142] K. P. Ong, T. W. Goh, Q. Xu, A. Huan, Mechanical origin of the structural phase transition in methylammonium lead iodide $\text{CH}_3\text{NH}_3\text{PbI}_3$. *Journal of the Physical Chemistry Letters*. **6**, 681–685 (2015).
- [143] L. Chi, I. P. Swainson, L. Cranswick, J. H. Her, P. Stephens, O. Knop, The ordered phase of methylammonium lead chloride $\text{CH}_3\text{NH}_3\text{PbCl}_3$. *Journal of Solid State Chemistry*. **178**, 1376–1385 (2005).
- [144] H. Mashiyama, Y. Kawamura, E. Magome, Y. Kubota, Displacive character of the cubic-tetragonal transition in $\text{CH}_3\text{NH}_3\text{PbIX}_3$, *Journal of the Korean Physical Society*. **42**, S1026–S1029 (2003).

- [145] C. Quarti, E. Mosconi, J. M. Ball, V. D'Innocenzo, C. Tao, S. Pathak, H. J. Snaith, A. Petrozza, F. De Angelis, Structural and optical properties of methylammonium lead iodide across the tetragonal to cubic phase transition: implications for perovskite solar Cells, *Energy and Environmental Science*. **9**, 155–163(2016).
- [146] B. J. Foley, D. L. Marlowe, K. Sun, W. A. Saidi, L. Scudiero, M. C. Gupta, J. J. Choi, Temperature dependent energy levels of methylammonium lead iodide perovskite, *Applied Physics Letters*.**106**, 243904 (2015).
- [147] J. Burschka, N. Pellet, S.-J. Moon, R. Humphry-Baker, P. Gao, M. K. Nazeeruddin and M. Grätzel, Sequential deposition as a route to high-performance perovskite-sensitized solar cells, *Nature*. **499**, 316–319 (2013).
- [148] F. Meillaud, A. Shah, C. Droz, E. Vallat-Sauvain and C. Miazza, Efficiency limits for single-junction and tandem solar cells, *Solar Energy Materials and Solar Cells*. **90**, 2952–2959 (2006).
- [149] D. B. Mitzi, *Progress in Inorganic Chemistry*, John Wiley & Sons, Inc, 1999, vol. 48.
- [150] G. E. Eperon, S. D. Stranks, C. Menelaou, M. B. Johnston, L. M. Herz, and H. J. Snaith, Formamidinium lead trihalide: a broadly tunable perovskite for efficient planar heterojunction solar cells, *Energy and Environmental Science*, **7**, 982 (2014).
- [151] S. D. Stranks, G. E. Eperon, G. Grancini, C. Menelaou, M. J. P. Alcocer, T. Leijtens, L. M. Herz, A. Petrozza and H. J. Snaith, Electron-hole diffusion lengths exceeding 1 micrometer in an organometal trihalide perovskite absorber, *Science*. **342**, 341–344 (2013).
- [152] G. E. Eperon, V. M. Burlakov, P. Docampo, A. Goriely and H. J. Snaith, Morphological control for high performance, solution-processed planar heterojunction perovskite solar cells. *Advanced Functional Materials*. **24**, 151–157 (2013).
- [153] B. Cai, Y. Xing, Z. Yang, W.-H. Zhang and J. Qiu, High performance hybrid solar cells sensitized by organolead halide perovskite, *Energy and Environmental Science*. **6**, 1480–1485 (2013).

[154] J. H. Noh, S. H. Im, J. H. Heo, T. N. Mandal and S. Il Seok, Chemical management for colourful, efficient, and stable inorganic-organic hybrid nanostructured solar cells, *Nano Letters*. **13**, 1764–1769 (2013).

[155] H. Tanaka, and K. Iio, K. Nagata, Magnetic properties of $\text{Rb}_{1-x}\text{K}_x\text{NiCl}_3$, RbVBr_3 and CsNiL_3 , *Journal of Magnetism and Magnetic Materials*. **104 – 107**, 829 – 830 (1992).

[156] J. Burschka, N. Pellet, S.-J. Moon, R. Humphry-Baker, P. Gao, M. K. Nazeeruddin, and M. Grätzel, Sequential deposition as a route to high-performance perovskite-sensitized solar cells, *Nature*. **499**, 316 – 319 (2013).

[157] J. Im, J. Chung, S. Kim, and N. Park, Effects of crystallization and dopant concentration on the emission behaviour of $\text{TiO}_2\text{:Eu}$ nanophosphors. *Nanoscale Research Letters*. **7**, 1–7 (2012).

[158] D. B. Mitzi, Synthesis, Crystal Structure, and Optical and Thermal Properties of $(\text{C}_4\text{H}_9\text{NH}_3)_2\text{MI}_4$ ($\text{M}=\text{Ge}, \text{Sn}, \text{Pb}$), *Chemistry of Materials*. **8**, 791 – 800 (1996).

[159] D. B. Mitzi, C. D. Dimitrakopoulos, and L. L. Kosbar, Structurally Tailored Organic-inorganic Perovskites: Optical Properties and Solution-Processed Channel Materials for Thin-Film Transistors, *Chemistry of Materials*. **13**, 3728 – 3740 (2001).

[160] X. Hong, T. Ishihara, and A. Nurmikko, Dielectric confinement effect on excitons in PbI_4 -based layered semiconductors, *Physical Reviews B*. **45**, 6961 – 6964 (1992).

[161] S. Wang, D. B. Mitzi, C. A. Feild, and A. Guloy, Synthesis and Characterization of $[\text{NH}_2\text{C}(\text{I})\text{:NH}_2]_3\text{MI}_5$ ($\text{M}=\text{Sn}, \text{Pb}$): Stereochemical Activity in Divalent Tin and Lead Halides Containing Single. Itrbrac. 110. Rtbbrac. Perovskite Sheets, *Journal of the American Chemical Society*. **117**, 5297 – 5302 (1995).

[162] D. B. Mitzi, K. Chondroudis, and C. R. Kagan, Design, Structure, and Optical Properties of Organic-inorganic Perovskite Containing an Oligothiophene Chromophore, *Inorganic Chemistry*. **38**, 6246 – 6256 (1999).

[163] D. B. Mitzi, Organic-inorganic Perovskites Containing Trivalent Metal Halide: The Templating Influence of the Organic Cation Layer, *Inorganic Chemistry*. **39**, 6107 – 6113 (2000).

[164] D. B. Mitzi, and P. Brock, Structure and Optical properties of Several Organic-Inorganic Hybrids Containing Corner-Sharing Chains of Bismuth Iodide Octahedra, *Inorganic Chemistry*. **40**, 2096 – 2104 (2001).

[165] I. Borriello, G. Cantele, and D. Ninno, *Ab Initio* investigation of hybrid organic-inorganic perovskite based on tin halides, *Physical Review. B*. **77**, 235214 (2008).

[166] J. L. Knutson, J. D. Martin, and D. B. Mitzi, Tuning the Band Gap in Hybrid Tin Iodide Perovskite Semiconductors Using Structural Templating, *Inorganic Chemistry*. **44**, 4699 – 4705 (2005).

[167] E. Mosconi, A. Amat, M. K. Nazeeruddin, M. Grätzel, and F. De Angelis, First-Principles Modeling of Modeling of Mixed Halide Organometal Perovskites for Photovoltaic Applications, *The Journal of Physical Chemistry C*. **117**, 13902 – 13913 (2013).

[168] C. C. Stoumpos, C. D. Malliakas, M. G. Kanatzidis, Semiconducting Tin and Lead Iodide Perovskites with Organic Cations: Transitions, High Mobilities, and Near-Infrared Photoluminescent Properties, *Inorganic Chemistry*. **52**, 9019 – 9038 (2013).

[169] W. Shockley, and H. J. Queisser, Detailed Balance Limit of Efficiency of *p-n* Junction Solar Cells, *Journal of Applied Physics*. **32**, 510 (1961).

[170] D. Mitzi, S. Wang, C. Feild, C. Chess, and A. Guloy, Conducting Layered Organic-inorganic Halide Containing <110>- oriented Perovskites Sheets, *Science*. **267**, 1473 – 1476 (1995).

[171] Y. Lee, D. Mitzi, P. Barnes, and T. Vogt, Pressure-Induced phase transitions and templating effect in three-dimensional organic-inorganic hybrid perovskites, *Physical Review B*. **68**, 020103 (2003).

[172] J. H. Noh, S. H. Im, J. H. Heo, T. N. Mandal, and S. Il Seok, Chemical Management for Colourful, Efficient, and stable Inorganic-Organic Hybrid Nanostructured Solar Cells, *Nano Letters*. **13**, 1764 – 1769 (2013).

[173] N. Pellet, P. Gao, G. Gregori, T. Y. Yang, M. K. Nazeeruddin, J. Maier, and M. Gratzel, Mixed-Organic-Cation Perovskite Photovoltaics for Enhanced Solar-light harvesting, *Angewandte Chemie International Edition in English*. **53**, 3151-3157 (2014).

[174] J. Burschka, A. Dualeh, F. Kessler, E. Baranoff, N.-L. Cevy-Ha, C. Yi, M. K. Nazeeruddin, and M. Gratzel, Tris(2-(1*H*-pyrazol-1-yl)pyridine) cobalt (III) as p-Type Dopant for Organic Semiconductors and Its application in Highly Efficient Solid-State Dye-sensitized Solar Cells, *Journal of the American Chemical Society*. **133**, 18042 – 18045 (2011).

[175] H.-S. Kim et al. Lead iodide perovskite sensitized all-solid-state submicron thin film mesoscopic solar cell with efficiency exceeding 9%, *Science Reports*. **2**, 591 (2012).

[176] M. Liu, M. B. Johnston, and H. J. Snaith, Efficient planar heterojunction perovskite solar cells by vapour deposition. *Nature*. **501**, 395–398 (2013).

[177] J. Burschka et al. Sequential deposition as a route to high-performance perovskite-sensitized solar cells, *Nature*. **499**, 316–319 (2013).

[178] M. M. Lee, J. Teuscher, T. Miyasaka, T. N. Murakami, and H. J. Snaith, Efficient hybrid solar cells based on meso-superstructured organometal halide perovskites, *Science*. **338**, 643–647 (2012).

[179] C. C. Stoumpos, C. D. Malliakas, and M. G. Kanatzidis, Semiconducting tin and lead iodide perovskites with organic cations: phase transitions, high mobilities, and near-infrared photoluminescent properties, *Inorganic Chemistry* **52**, 9019–9038 (2013).

[180] G. Xing et al, Long-range balanced electron- and hole-transport lengths in organic–inorganic CH₃NH₃PbI₃, *Science*. **342**, 344–347 (2013).

[181] S. D. Stranks et al, Electron–hole diffusion lengths exceeding 1 micrometer in an organometal trihalide perovskite absorber, *Science* **342**, 341–344 (2013).

[182] P. Umari, E. Mosconi, and F. de Angelis, Relativistic solar cells. Preprint at <http://arxiv-web.arxiv.org/abs/>. **1309.4895** (2013).

[183] S. Rein, *Lifetime Spectroscopy: A Method of Defect Characterization in Silicon for Photovoltaic Applications* (Springer, 2004).

[184] H.-S. Kim et al, Mechanism of carrier accumulation in perovskite thin-absorber solar cells. *Nature Communications*. **4**, 2242 (2013).

[185] F. Hao, C. C. Stoumpos, D. H. Cao, R. P. H. Chang, and M. G. Kanatzidis, Lead-free solid-state organic-inorganic halide perovskite solar cells, *Nature Photonics*. **8**, 489 – 494 (2014).

[186] B. Kippelen, and J. L. Bredas, *Organic Photovoltaics*, *Energy and Environmental Science*. **2**, 251 (2009).

[187] J.H. Heo, S. H. Im, J. H. Noh, T. N. Mandal, C. S. Lim, J. A. Chang, Y. H. Lee, H. J. Kim, A. Sarkar, M. K. Nazeeruddin, M. Grätzel, and S. I. Seok, Efficient inorganic-organic hybrid heterojunction solar cells containing perovskite compound polymeric hole conductors, *Nature Photonics*. **7**, 487 (2013).

[188] M. Z. Liu, M. B. Johnston, and H. J. Snaith, Efficient planar heterojunction perovskites solar cells by vapour deposition, *Nature*. **501**, 395 (2013).

[189] J. Burschka, N. Pellet, S. J. Moon, R. Humphry-Baker, P. Gao, M. K. Nazeeruddin, and M. Grätzel, Sequential deposition as a route to high-performance perovskite-sensitized solar cells, *Nature*. **499**, 316 (2013).

[190] H. S. Kim, J. W. Lee, N. Yantara, P. P. Boix, S. A. Kulkarni, S. Mhaisalkar, M. Grätzel, and N. G. Park, High Efficiency Solid-State Sensitized Solar Cell-Based on

Submicrometer Rutile TiO₂ Nanorod and CH₃NH₃PbI₃ Perovskite Sensitizers, *Nano Letters*. **13**, 2412 (2013).

[191] A. Abrusci, S. D. Stranks, P. Docampo, H. L. Yip, A. K. Y. Jen, and H. J. Snaith, High-Performance Perovskite-Polymer Hybrid Solar Cells via Electronic Coupling with Fullerene Monolayers, *Nano Letters*. **13**, 3124 (2013).

[192] J. M. Ball, M. M. Lee, A. Hey, and H. J. Snaith, Low-temperature processed mesosuperstructured to thin-film perovskite solar cells, *Energy and Environmental Science*. **6**, 1739 (2013).

[193] M. M. Lee, J. Teuscher, T. Miyasaka, T. N. Murakami, and H. J. Snaith, Efficient Hybrid Solar Cells Based on Meso-superstructured Organometal Halide Perovskites, *Science*. **338**, 643 (2012).

[194] C. C. Stoumpos, C. D. Malliakas, and M. G. Kanatzidis, Semiconducting Tin and Lead Iodide Perovskites with Organic Cations: Phase Transitions, High Mobilities, and Near-Infrared Photoluminescent Properties, *Inorganic Chemistry*. **52**, 9019 (2013).

[195] Y. Ogomi, A. Morita, S. Tsukamoto, T. Saitho, N. Fujikawa, Q. Shen, T. Toyoda, K. Yoshino, S. S. Pandey, T. Ma, and S. Hayase, CH₃NH₃Sn_xPb_(1-x)I₃ Perovskite Solar Cells Covering up to 1060 nm, *Journal of the Physical Chemistry Letters*. **5**, 1004 (2014).

[196] J. H. Noh, S. H. Im, J. H. Heo, T. N. Mandal, and S. I. Seok, Chemical Management for Colourful, Efficient, and Stable Inorganic-Organic hybrid Nanostructured Solar Cells, *Nano Letters*. **13**, 1764 (2013).

[197] T. M. Koh, K. Fu, Y. Fang, S. Chen, T. C. Sum, N. Mathews, N.; S. G. Mhaisalkar, P. P. Boix, and T. Baikie, Formamidinium-Containing Metal-Halide: An Alternative Material for Near-IR Absorption Perovskite Solar Cells, *The Journal of Physical Chemistry C*. 2013, ASAP, DOI: 10.1021/jp411112k.

[198] G. E. Eperon, S. D. Stranks, C. Menelaou, M. B. Johnston, L. M. Herz, and H. J. Snaith, Formamidinium lead trihalide: a broadly tunable perovskite for efficient planar heterojunction solar cells, *Energy and Environmental Science*. **7**, 982 (2014).

[199] F. Meillaud, A. Shah, C. Droz, E. Vallat-Sauvain, and C. Miazza, Efficiency limits for single-junction and tandem solar cells, *Solar Energy Materials and Solar Cells*. **90**, 2952 (2006).

[200] D. B. Mitzi, Thin-Film Deposition of Organic-Inorganic Hybrid Materials, *Chemistry of Materials*. **13**, 3283 (2001).

[201] K. N. Liang, D. B. Mitzi, and M. T. Prikas, Synthesis and Characterization of Organic-Inorganic Perovskite Thin Films Prepared Using a Versatile Two-Step Dipping Technique, *Chemistry of Materials*. **10**, 403 (1998).

[202] Y. Takahashi, R. Obara, Z. Z. Lin, Y. Takahashi, T. Naito, T. Inabe, S. Ishibashi, and K. Terakura, Charge Transport in tin-iodide perovskite $\text{CH}_3\text{NH}_3\text{SnI}_3$: origin of high conductivity, *Dalton Transactions*. **40**, 5563 (2011).

[203] Y. Takahashi, H. Hasegawa, Y. Takahashi, and T. Inabe, Hall mobility in tin iodide perovskite $\text{CH}_3\text{NH}_3\text{SnI}_3$: Evidence for doped semiconductors, *Journal of Solid State Chemistry*. **205**, 39 (2013).

[204] F. Hao, C. C. Stoumpos, R. P. H. Chang, and M. G. Kanatzidiz, Anomalous Band Gap Behaviour in Mixed Sn and Pb Perovskites Enables Broadening of Absorption Spectrum in Solar Cells, *Journal of the American Chemical Society*. **136**, 8094 – 8099 (2014).

[205] H. S. Kim, I. Mora-Sero, V. Gonzalez-Pedro, F. Fabregat- Santiago, E. J. Juarez-Perez, N. G. Park, and J. Bisquert, Morphological Control for High Performance, Solution-Processed Planar Heterojunction Perovskite Solar Cells, *Nature Communications*. **4**, 2242(2013).

[206] J. T.-W. Wang, J. M. Ball, E. M. Barea, A. Abate, J. A. Alexander- Webber, J. Huang, M. Saliba, I. Mora-Sero, J. Bisquert, H. J. Snaith et al., Low-Temperature Processed Electron

Collection Layers of Graphene/TiO₂ Nanocomposites in Thin Film Perovskite Solar Cells. *Nano Letters*. **14**, 724–730 (2014).

[207] K. Wojciechowski, M. Saliba, T. Leijtens, A. Abate, and H. J. Snaith, Sub-150°C Processed Meso-Superstructured Perovskite Solar Cells with Enhanced Efficiency, *Energy and Environmental Science*. **7**, 1142–1147 (2014).

[208] M. H. Kumar, N. Yantara, S. Dharani, M. Graetzel, S. Mhaisalkar, P. P. Boix, N. Mathews, Flexible, Low-Temperature, Solution Processed ZnO-Based Perovskite Solid State Solar Cells, *Chemical Communications*. **49**, 11089–11091 (2013).

[209] J. H. Noh, S. H. Im, J. H. Heo, T. N. Mandal, S. I. Seok, Chemical Management for Colorful, Efficient, and Stable Inorganic–Organic Hybrid Nanostructured Solar Cells, *Nano Letters*. **13**, 1764–1769 (2013).

[210] H.-S. Kim, C.-R. Lee, J.-H. Im, K.-B. Lee, T. Moehl, A. Marchioro, S.-H. Moon, R. Humphry-Baker, J.-H. Yum, J. E. Moser, M. Graetzel et al., Lead Iodide Perovskite Sensitized All-Solid-State Submicron Thin Film Mesoscopic Solar Cell with Efficiency Exceeding 9%, *Science Reports*. **2**, 591 (2012).

[211] H.-S. Kim, I. Mora-Sero, V. Gonzalez-Pedro, F. Fabregat-Santiago, E. J. Juarez-Perez, N.-G. Park, J. Bisquert, Mechanism of Carrier Accumulation in Perovskite Thin-Absorber Solar Cells, *Nature Communications*. **4**, 2242(2013).

[212] V. Gonzalez-Pedro, E. J. Juarez-Perez, W.-S. Arsyad, E. M. Barea, F. Fabregat-Santiago, I. Mora-Sero, J. Bisquert, General Working Principles of CH₃NH₃PbX₃ Perovskite Solar Cells, *Nano Letters*. **14**, 888–893 (2014).

[213] E. Edri, S. Kirmayer, A. Henning, S. Mukhopadhyay, K. Gartsman, Y. Rosenwaks, G. Hodes, D. Cahen, Why Lead Methylammonium Tri-Iodide Perovskite-Based Solar Cells Require a Mesoporous Electron Transporting Scaffold (but Not Necessarily a Hole Conductor), *Nano Letters*. **14**, 1000–1004 (2014).

- [214] S. Colella, E. Mosconi, P. Fedeli, A. Listorti, F. Gazza, F. Orlandi, P. Ferro, T. Besagni, A. Rizzo, G. Calestani et al., MAPbI₃-xCl_x Mixed Halide Perovskite for Hybrid Solar Cells: The Role of Chloride as Dopant on the Transport and Structural Properties, *Chemical Materials*. **25**, 4613–4618 (2013).
- [215] F. Fabregat-Santiago, G. Garcia-Belmonte, I. Mora-Sero, J. Bisquert, Characterization of Nanostructured Hybrid and Organic Solar Cells by Impedance Spectroscopy, *Physical Chemistry Chemical Physics*. **13**, 9083–9118 (2011).
- [216] A. Dualeh, T. Moehl, N. Tétreault, J. Teuscher, P. Gao, M. K. Nazeeruddin, M. Grätzel, Impedance Spectroscopic Analysis of Lead Iodide Perovskite-Sensitized Solid-State Solar Cells, *ACS Nano*. **8** (1), 362–373 (2013).
- [217] E. J. Juarez-Perez, M. Wubler, F. Fabregat-Santiago, K. Lakus-Wollny, E. Mankel, T. Mayer, W. Jaegermann, I. Mora-Sero, Role of the Selective Contacts in the Performance of Lead Halide Perovskite Solar Cells, *The Journal of Physical Chemistry Letters*. **5**, 680–685 (2014).
- [218] H.-S. Kim, J.-W. Lee, N. Yantara, P. P. Boix, S. A. Kulkarni, S. Mhaisalkar, M. Grätzel, N.-G. Park, High Efficiency Solid-State Sensitized Solar Cell-Based on Submicrometer Rutile TiO₂ Nanorod and CH₃NH₃PbI₃ Perovskite Sensitizer, *Nano Letters*. **16**, 2412–2417 (2013).
- [219] J. A. Christians, R. C. M. Fung, and P. V. Kamat, An Inorganic Hole Conductor for Organo-Lead Halide Perovskite Solar Cells. Improved Hole Conductivity with Copper Iodide, *Journal of American Chemical Society*. **136**, 758–764 (2013).
- [220] P. Schulz, E. Edri, S. Kirmayer, G. Hodes, D. Cahen, A. Kahn, Interface Energetics in Organo-Metal Halide Perovskite-Based Photovoltaic Cells, *Energy and Environmental Science*. **7**, 1377–1381 (2014).
- [221] A. Kojima, K. Teshima, Y. Shirai, and T. Miyasaka, Organometal Halide Perovskites as Visible-Light Sensitizers for Photovoltaic Cells, *Journal of American Chemical Society*. **131**, 6050–6051 (2009).

[222] B. Suarez, V. Gonzalez-Pedro, T. S. Ripolles, R. S. Sandnez, L. Otero, and I. Mora-Sero, Recombination Study of Combined Halides (Cl, Br, I) Perovskite Solar Cells, *The Journal of Physical Chemistry Letters*. **5**, 1628 – 1635 (2014).

[223] S. A. Kulkarni, T. Baikie, P. P. Boix, N. Yantara, N. Mathews, and S. Mhaisalkar, Band-gap tuning of lead halide perovskites using a sequential deposition process, *Journal of Materials Chemistry A*. **2**, 9221 – 9225 (2014).

[224] A. L. Abdelhady, M. S. Saidaminoy, B. Murali, V. Adinolfi, O. Voznyy, K. Katsev, O. F. Mohammed, and O. M. Bakr, Heterovalent Dopant Incorporation for Bandgap and Type Engineering of Perovskite Crystals, *Journal of the Physical Chemistry Letters*. **7**, 295 – 301 (2016).

[225] V. Palankovski, G. Kaiblinger-Grujin, S. Selberherr, Study of Dopant-Dependent Band Gap Narrowing in Compound Semiconductor Devices, *Materials Science and Engineering B*. **66**, 46–49 (1999).

[226] P. Van Mieghem, Theory of Band Tails in Heavily Doped Semiconductors, *Reviews of Modern Physics*. **64**, 755–793 (1992).

[227] P. Gao, M. Gratzel, M. K. Nazeeruddin, Organohalide Lead Perovskites for Photovoltaic Applications, *Energy and Environmental Science*. **7**, 2448–2463 (2014).

[228] S. D. Stranks, G. E. Eperon, G. Grancini, C. Menelaou, M. J. P. Alcocer, T. Leijtens, L. M. Herz, A. Petrozza, H. J. Snaith, Electron-Hole Diffusion Lengths Exceeding 1 Micrometer in an Organometal Trihalide Perovskite Absorber, *Science*. **342**, 341– 344 (2013).

[229] Y. Tidhar, E. Edri, H. Weissman, D. Zohar, G. Hodes, D. Cahen, B. Rybtchinski, S. Kirmayer, Crystallization of Methyl Ammonium Lead Halide Perovskites: Implications for Photovoltaic Applications, *Journal of American Chemical Society*. **136**, 13249–13256 (2014).

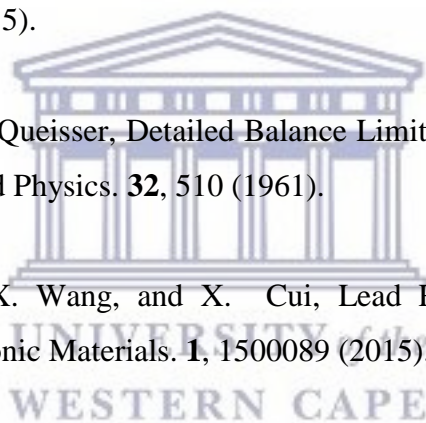
[230] D. W. de Quilettes, S. M. Vorpahl, S. D. Stranks, H. Nagaoka, G. E. Eperon, M. E. Ziffer, H. J. Snaith, D. S. Ginger, Impact of Microstructure on Local Carrier Lifetime in Perovskite Solar Cells, *Science*. **348**, 683–686 (2015).

[231] S. Colella, E. Mosconi, P. Fedeli, A. Listorti, F. Gazza, F. Orlandi, P. Ferro, T. Besagni, A. Rizzo, G. Calestani et al., R. MAPbI_(3-x)Cl_x Mixed Halide Perovskite for Hybrid Solar Cells: the Role of Chloride as Dopant on the Transport and Structural Properties, *Chemistry of Materials*. **25**, 4613–4618 (2013).

[232] J. Navas, A. Sánchez-Coronilla, J. J. Gallardo, N. Cruz Hernández, J. C. Piñero, R. Alcántara, C. Fernández-Lorenzo, D, M. De los Santos, T. Aguilar, J. Martín-Calleja, New Insights into Organic-Inorganic Hybrid Perovskite CH₃NH₃PbI₃ Nanoparticles. An Experimental and Theoretical Study of Doping in Pb²⁺ Sites with Sn²⁺, Sr²⁺, Cd²⁺ and Ca²⁺. *Nanoscale*. **7**, 6216–6229 (2015).

[233] W. Shockley, and H. J. Queisser, Detailed Balance Limit of Efficiency of p-n Junction Solar Cells, *Journal of Applied Physics*. **32**, 510 (1961).

[234] K. Wang, Z. Liang, X. Wang, and X. Cui, Lead Replacement in CH₃NH₃PbI₃ Perovskites. *Advanced Electronic Materials*. **1**, 1500089 (2015).



CHAPTER 3

Experimental Details

3.1 INTRODUCTION

The work done on bandgap engineering of organometallic halide perovskite materials has been extensively reviewed in chapter 2. It was mentioned that the bandgap of organometallic halide perovskite materials can be decreased by (i) increasing the in-plane M-I-M bond angle, which is done by octahedral tilting distortions, (ii) increasing the dimensionality of the $MI(X)_6$ network, and (iii) by the decrease in the electronegativity of the anions system [1]. Experimental studies demonstrated that the absorption of $CH_3NH_3PbX_3$ shifts to the blue region of the solar spectrum with changing of anions from I^- to Br^- to Cl^- . Mixed anions perovskites $CH_3NH_3Pb(I_{1-x}Br_x)_3$ showed a blue-shift absorption band-edge in comparison to that of $CH_3NH_3PbI_3$ due to the fact that I^- anion has a lower electronegativity than that of Br^- anion [2,3]. In this study, chalcogenide anions with low electronegativities; S (2.58) & Se (2.55), than I_2 (2.66), will be incorporated into triiodide perovskite structure $CH_3NH_3PbI_3$ to modulate (tune) the bandgap. These chalcogenide anions are heterovalent (S^{2-} , Se^{2-}) to I^- and this was inspired by the work done by A. L. Abdelhady et al., whereby bandgap engineering was done by heterovalent doping of organometallic triiodide perovskite material with trivalent cations; Bi^{3+} , Au^{3+} , and In^{3+} (in contrast to Pb^{2+}) [4].

3.2 REAGENTS

Methylamine solution (33 wt % in absolute ethanol), Ethanol (99,8%), lead(II) iodide (99,99% trace metal basis), lead (II) iodide (99,99% trace metal basis), lead (II) sulphide (99,99% trace metal basis), Nitric acid (70%, purified by redistillation, $\geq 99,99\%$ trace metal basis), Hydrochloric acid (37%), Hydroiodic acid (55 wt % in H_2O , distilled stabilized, 99,95%), Dimethyl formamide (99,8%), Dimethyl sulfoxide ($\geq 99,5\%$) and Lithium perchlorate (99,99%). All reagents were obtained from Sigma Aldrich and were used without

further purification. Alumina micro polishing pads were obtained from Buehler and urea (99.5%) was obtained from Fluka.

3.3 EXPERIMENT AND PROCEDURE

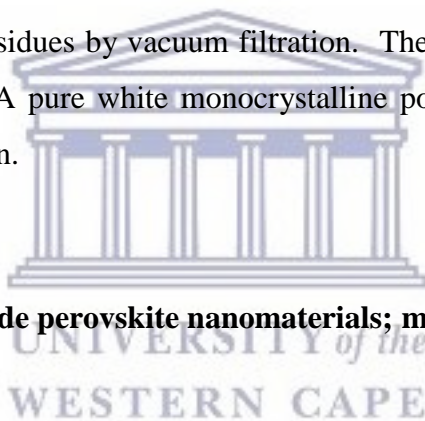
3.3.1 Synthesis of triiodide perovskite nanomaterials: $\text{CH}_3\text{NH}_3\text{PbI}_3$.

(a) Preparation of the starting materials; methylammonium iodide, $\text{CH}_3\text{NH}_3\text{I}$:

The starting material was prepared directly from methylamine solution, CH_3NH_2 (50 mL) in excess and hydroiodic acid (20 mL) in ethanol (200 mL) under nitrogen atmosphere for 2 h.

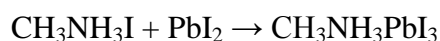


The reaction mixture was then taken for rotary evaporation at 50°C for 30 min. A yellow white precipitate was obtained which was then washed 3 times with ethanol followed by diethyl ether to remove the residues by vacuum filtration. The precipitate was then dried in an oven at 60°C for 24 h. A pure white monocrystalline powder was obtained and used without any further purification.



(b) Synthesis of the triiodide perovskite nanomaterials; methylammonium lead triiodide, $\text{CH}_3\text{NH}_3\text{PbI}_3$.

A triiodide perovskite solution, $\text{CH}_3\text{NH}_3\text{PbI}_3$ was formed from an equimolar mixing of the starting material $\text{CH}_3\text{NH}_3\text{I}$ (0.77115 g, 0.004853 mol) and lead iodide PbI_2 (2.2373 g, 0.004853 mol) in 15 mL solvent mixture of dimethylformamide (DMF)/dimethyl sulfoxide (DMSO), 7:3 (v:v) for 12 h under nitrogen atmosphere:



The metal halide reagent PbI_2 was first dissolved completely in the solvent mixture on hot plate at 75°C , followed by addition of $\text{CH}_3\text{NH}_3\text{I}$ and the reaction mixture turned to a yellow homogenous solution after 2 h. A homogeneous yellow solution was obtained as a product after 12 h.

3.3.2 Incorporation of chalcogenide anions (S and Se) into the triiodide perovskite structure to form new mixed ions (organo-chalogenic) perovskites, $\text{CH}_3\text{NH}_3\text{PbI}_2\text{S}$ and $\text{CH}_3\text{NH}_3\text{PbI}_2\text{Se}$.

The procedure for the synthesis of mixed ions perovskite $\text{CH}_3\text{NH}_3\text{PbI}_2\text{Cl}$ [5] was mimicked in this study to prepare organo-chalogenic perovskites; $\text{CH}_3\text{NH}_3\text{PbI}_2\text{S}$ and $\text{CH}_3\text{NH}_3\text{PbI}_2\text{Se}$. In this procedure, $\text{CH}_3\text{NH}_3\text{PbI}_2\text{Cl}$ was formed by reacting $\text{CH}_3\text{NH}_3\text{I}$ (in excess) with PbCl_2 (source of chlorine, Cl) in a ratio 3:1 of $\text{CH}_3\text{NH}_3\text{I}$ to PbCl_2 .

(a) Synthesis of $\text{CH}_3\text{NH}_3\text{PbI}_2\text{S}$.

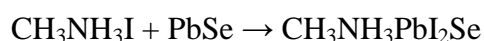
The starting material $\text{CH}_3\text{NH}_3\text{I}$ (0.77115 g, 0.00485 mol) (in excess) was reacted with PbS (0.3877 g, 0.00162 mol) in 15 mL solvent mixture of dimethylformamide (DMF)/dimethyl sulfoxide (DMSO), 7:3 (v:v) for 12 h under nitrogen atmosphere:



The metal chalcogenide reagent PbS was first digested in 2mL aqua regia solution (HNO_3 : HCl , 1 : 3, v:v) followed by addition of $\text{CH}_3\text{NH}_3\text{I}$. The reaction mixture turned to a dark black homogenous solution immediately. A dark black homogeneous solution was obtained as a product after 12 h.

(b) Synthesis of $\text{CH}_3\text{NH}_3\text{PbI}_2\text{Se}$.

The starting material $\text{CH}_3\text{NH}_3\text{I}$ (0.77115 g, 0.00485 mol) (in excess) was reacted with PbSe (0.4636 g, 0.00162 mol) in 15 mL solvent mixture of dimethylformamide (DMF)/dimethyl sulfoxide (DMSO), 7:3 (v:v) for 12 h under nitrogen atmosphere:

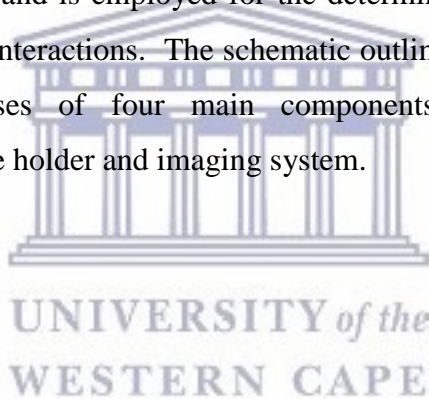


The metal chalcogenide reagent PbSe was first digested in 2mL aqua regia solution (HNO_3 : HCl , 1 : 3, v:v) followed by addition of $\text{CH}_3\text{NH}_3\text{I}$. The reaction mixture also turned to a dark black homogenous solution immediately. A dark black homogenous solution was obtained as a product after 12 h.

3.4 MATERIALS CHARACTERIZATION TECHNIQUES & INSTRUMENTATION

3.4.1 High-Resolution Transmission Electron Microscopy (HR-TEM)

The prepared triiodide perovskite $\text{CH}_3\text{NH}_3\text{PbI}_3$ nanomaterials were taken for TEM analysis to determine the structure, particle size and crystallinity using TECNAI EDAX HR-TEM instrument. In TEM microscopy technique, a beam of electrons is transmitted through a very thin sample. There is an interaction that takes place between an electron beam and the sample during electron transmission. During the interaction, images are formed from the transmitted electrons, magnified and focused onto imaging devices or captured by a sensor such as CCD camera. Atoms in crystalline samples can be directly imaged by high resolution TEM at resolution 0.1 nm, which is smaller than the interatomic distance. High resolution TEM has the capacity to focus an electron beam to a diameter smaller than ~ 0.3 nm, enabling quantitative analysis from a single nanocrystal. High resolution TEM analysis is crucial for nanomaterial characterization and is employed for the determination of particle size, shape, crystallinity and interparticle interactions. The schematic outline of TEM is shown in Figure 3.1 below, and it comprises of four main components namely: electron source, electromagnetic lenses, sample holder and imaging system.



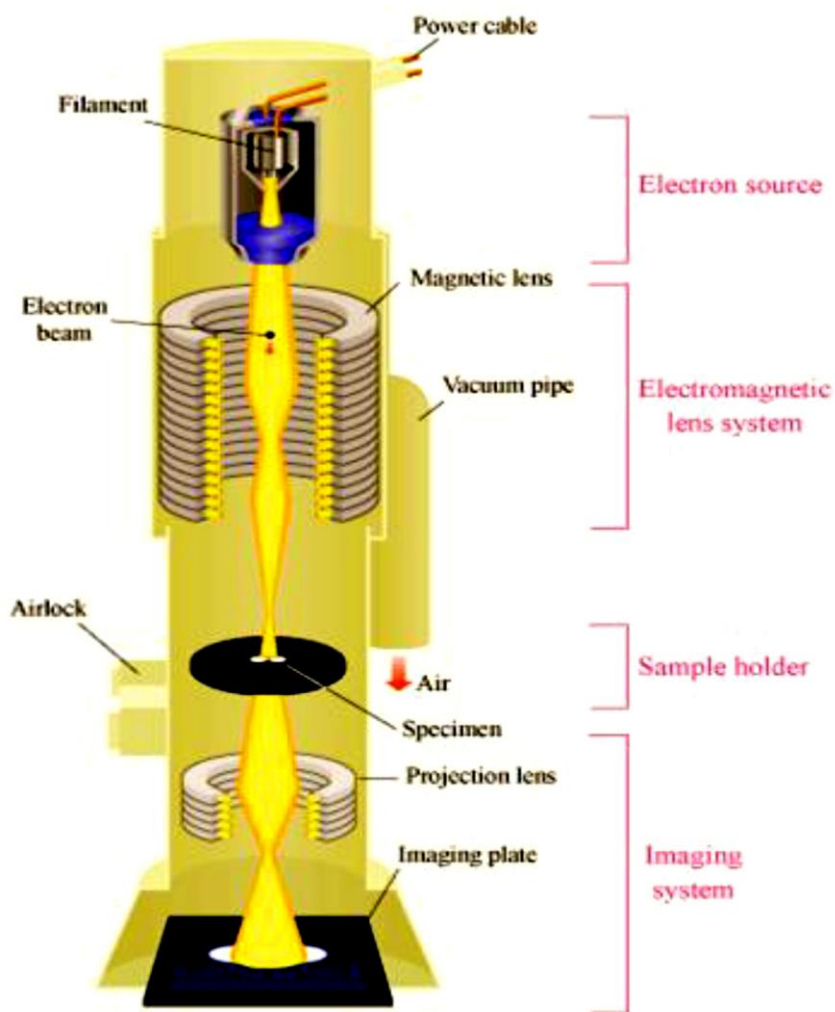


Figure 3.1: Schematic outline of TEM. Adapted with permission from Ref. [6].

During measurements, the produced electron beam passes through numerous electromagnetic lenses. The electron beam further passes through the solenoids (coil wrapped tubes surrounding an electron beam), down the specimen column and collides with the screen and to form an image. To manipulate the image, the voltage of the electron gun is adjusted to accelerate or decrease the speed of electrons and by also changing the electromagnetic wavelength through solenoids. The image is focused onto a screen or photographic plate by a coil [7].

3.4.2 Energy dispersive x-ray spectroscopy (EDS)

The elemental composition of the standard perovskite was determined by energy dispersive x-ray spectroscopy (EDS). The EDS is an analytical characterization technique that is used

together with SEM and TEM. During EDS measurements, an electron beam (typically 10 – 20 keV) is struck upon the surface of the conducting sample, causing X-ray emissions corresponding to elemental composition of the material under investigation. This technique is a high resolution variant of electron microprobe analysis/x-ray microanalysis which gives information about the elemental composition of individual nanoparticles. In this study, the characterization of the triiodide perovskite nanoparticles $\text{CH}_3\text{NH}_3\text{PbI}_3$ was performed by coating a copper-carbon grid with a drop of sample and dried with electric lamp for 30 min [8].

3.4.3 Ultraviolet-Visible (UV-vis) Spectroscopy

UV-vis spectra of $\text{CH}_3\text{NH}_3\text{PbI}_3$, $\text{CH}_3\text{NH}_3\text{PbI}_2\text{S}$ and $\text{CH}_3\text{NH}_3\text{PbI}_2\text{Se}$ were collected on a UV-Vis spectrophotometer Nicolet evolution 100. In Ultraviolet-visible (UV-vis) spectrophotometer technique, light is absorbed and reflected in the ultraviolet-visible spectral region. The intensity (I) of light that passes through a sample is measured and compared to the original intensity (I_0) before passing through the sample. The ratio of the transmitted light intensity and the original intensity (I/I_0) and represented as a percentage (%T). The relationship between absorbance (A) and transmittance is given by the following equation.

$$A = -\log\left(\frac{\%T}{100}\right) \quad (3)$$

For reflectance measurements, the measured intensity of the reflected light from a sample (I) is compared to the intensity of the reflected light from a reference material (I_0). Reflectance is given by the ratio I/I_0 , and is represented as a percentage (%R). The typical UV-vis spectrophotometer technique comprises mainly of two sources of light, namely; deuterium (D2) and tungsten (W) lamps which covers ultraviolet (190 – 400 nm) and visible (300 – 2500 nm) spectral regions, respectively. The schematic outline of UV-vis spectrophotometer is shown in Figure 3.2.

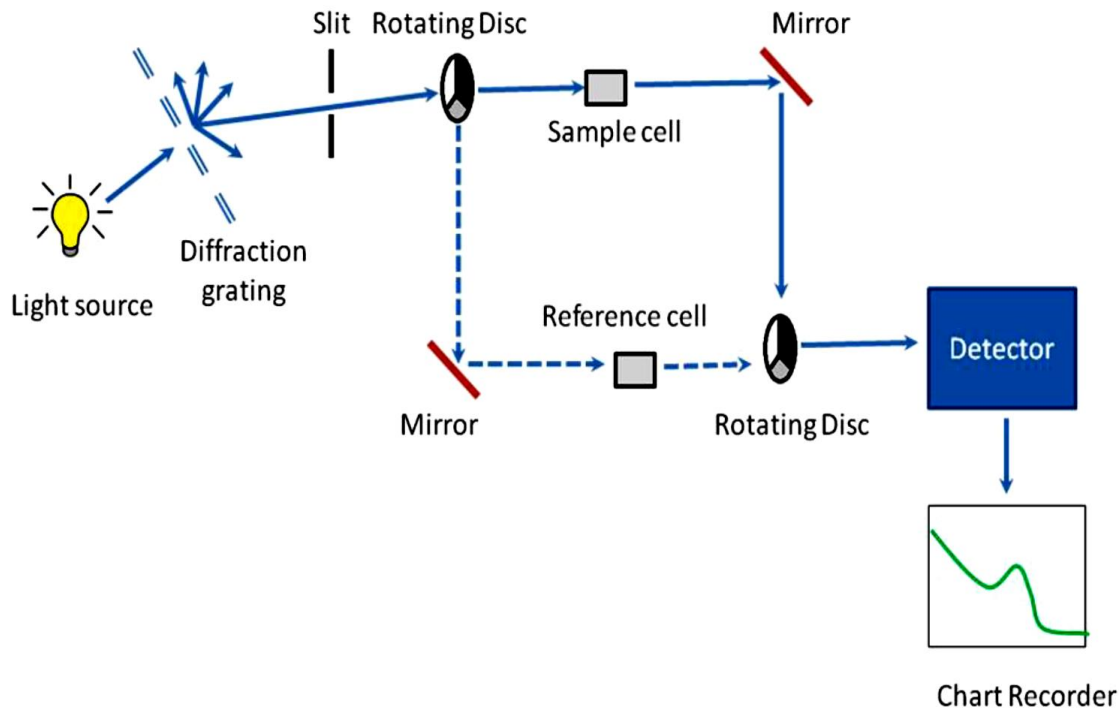


Figure 3.2: Schematic for the UV-visible spectrophotometer. Adapted with permission from Ref. [9].

During the measurements, a light beam is passed through the diffraction grating and the slits. Frequency wavelength is used to separate the radiation by diffraction grating, followed by a narrow slit. The purpose of the slit is to make sure that monochromatic radiation is of very narrowband. A photomultiplier or a photodiode is used to detect the radiation that passes through the sample or reference cell. Light that reaches the detector is filtered to single wavelength by using single photodiode detectors and photomultiplier tubes used in conjunction with scanning monochromator. The diffraction grating is moved to step-through each wavelength by scanning monochromator so that its intensity can be detected and measured as a function of wavelength. The bandgap energy (E_g) of the material (sample) can be determined from the absorption data obtained from the UV-Vis spectrophotometer. Tauc's relation is used to determine the bandgap energy. The difference between the top of the valence band filled with electrons and the bottom of the conduction band without electrons [10]. Tauc, Davis, and Mott proposed the following rational expression which is used to determine the bandgap:

$$h\nu\alpha = A h\nu - E_g^{\frac{1}{n}} \quad (4)$$

where h : Plank's constant, ν frequency of vibration, α : absorption coefficient, A : proportional constant, and E_g band gap energy. The nature of the sample transition is denoted by the value of the exponent n .

$$n = \frac{1}{2} \text{ for direct allowed transition}$$

$$n = \frac{3}{2} \text{ for direct forbidden transition}$$

$$n = 2 \text{ for indirect allowed transition}$$

$$n = 3 \text{ for indirect forbidden transition}$$

The optical bandgap of the sample is determined by the equation below:

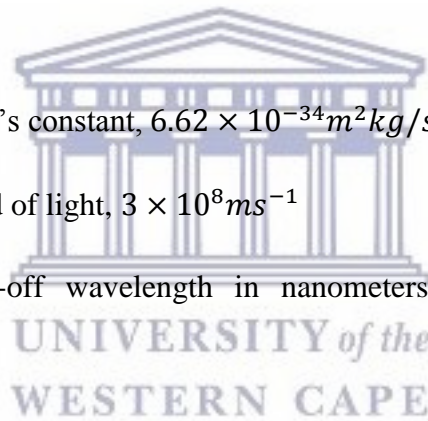
$$E = \frac{hc}{\lambda} = \frac{1240}{\lambda} \quad (5)$$

where:

$$h = \text{Plank's constant, } 6.62 \times 10^{-34} \text{ m}^2 \text{ kg/s,}$$

$$c = \text{speed of light, } 3 \times 10^8 \text{ ms}^{-1}$$

λ = cut-off wavelength in nanometers (nm) from the absorption spectrum of the sample [7].



3.4.4 Photoluminescence (PL) Spectroscopy

The luminescence of organometallic halide perovskite nanomaterials and dynamic processes occurring within the nanomaterials were analysed by using the IGA- 521 X 1 – 50 – 1700 – 1LS, HORIBA JOBIN YVON photoluminescence spectroscopy (PL) [11]. During photoluminescence experiment, light is propagated onto a sample, where it is absorbed and the excess energy is imparted into nanomaterials via photo-excitation process. The sample (organometallic halide nanomaterials) can only dissipate the energy in excess through light emission or luminescence. The excitation energy to the sample is supplied by the excitation source, Xenon lamp, emitted light is distributed in a spectral device, and the optical signal is converted into electric signal that is then processed by an electronic device and lastly by a controlling computer. The results of emission spectrum are recorded as a plot of

luminescence intensity against emission wavelength. The process taking place in the photoluminescence spectrophotometer employed during photoluminescence measurements in this study is outlined in Figure 3.3. An electric device is used to detect and process the emitted luminescence [7].

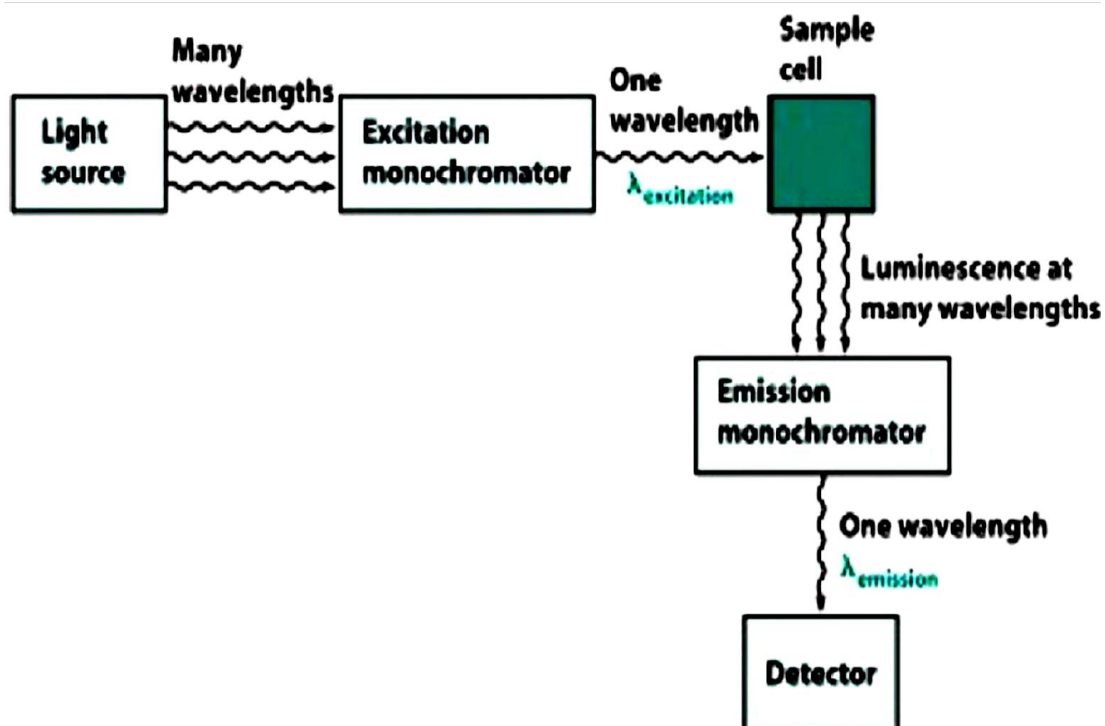


Figure 3.3: Outline presentation of photoluminescence spectroscopy. Adapted with permission from Ref. [12].

UNIVERSITY of the
WESTERN CAPE

3.4.5 Electrochemical characterization by Cyclic Voltammetry (CV)

Electrochemical characterization of all the prepared perovskite materials by cyclic voltammetry was carried out using BAS 100 W and automated electrochemical work station from bio analytical systems (BAS), Lafayette, USA. A computer interface to BAS 100 W electrochemical station was used to record all the cyclic voltammograms. The electrochemical cell (10 mL) system was built with traditional three electrode setup; (1) glassy carbon working electrode (GCE) ($A = 0.071 \text{ cm}^2$), platinum wire as a reference electrode and Ag/AgCl (3M KCl) used as a counter electrode. The glassy carbon electrode were first polished repeatedly with 1.0, 0.3 and 0.05 μm alumina slurries, rinsed with distilled water and sonicated in methanol for 10 min. Lithium perchlorate LiClO_4 (0.1 M, 5 mL) was used as an electrolyte to facilitate electron transfer during redox reactions. The electrolyte

was first purged with nitrogen for 15 minute, followed by addition of the sample (50 μ L). All cyclic voltammograms were recorded from -1000 mV to +1000 mV at a scan rate of 50 mv/s.

Cyclic voltammetry (CV) is an electrochemical characterization technique widely employed to study the oxidation/reduction (redox reactions), give insight into the kinetics of the electron reactions and to sense intermediates in electrochemical reactions. The potentials at which redox reactions takes place are indicated on sweep rates dependence. Therefore, CV is nearly a first choice technique employed to study any system for the first time owing its capacities. During CV experiment, the potential of the working electrode is ramped linearly against time. The potential of the working electrode is inverted when cyclic voltammetry reaches a set potential and this inversion can occur numerous times in only one experiment. The peak potentials (E_{pc} , E_{pa}) and the peak currents (I_{pc} , I_{pa}) are the important parameters in a recorded cyclic voltammogram for the anodic and cathodic scans, respectively. An electrochemically reversible reaction occurs when the electron transfer is faster than other processes such as diffusion [8]. The peak separation is given by the equation:

$$\Delta E_p = |E_{pa} - E_{pc}| = 2.303 \frac{RT}{nF} \quad (6)$$

where:

R = Gas constant, $8.135 \text{ J K}^{-1} \text{ mol}^{-1}$,

T = temperature in K (273 + temperature in $^{\circ}\text{C}$),

n = number of electrons,

F = Farady's constant, $9.684 \times 10^4 \text{ C mol}^{-1}$.

Therefore, for electrochemically reversible redox reactions occurring at $T = 25^{\circ}\text{C}$ with n electrons, the value of ΔE_p reduces to $\frac{0.0592}{n} \text{ V}$. For a reversible couple (or reaction), the formal reduction potential is given by the equation:

$$E^0 = \frac{(E_{pa} + E_{pc})}{2} \quad (7)$$

Organometallic halide perovskites are intrinsic semiconductor materials applied in photovoltaic cells and therefore determination of the bandgap of these materials is crucial.

The relative energy level involved in light harvesting of an organic solar cell is shown in Figure 3.4.

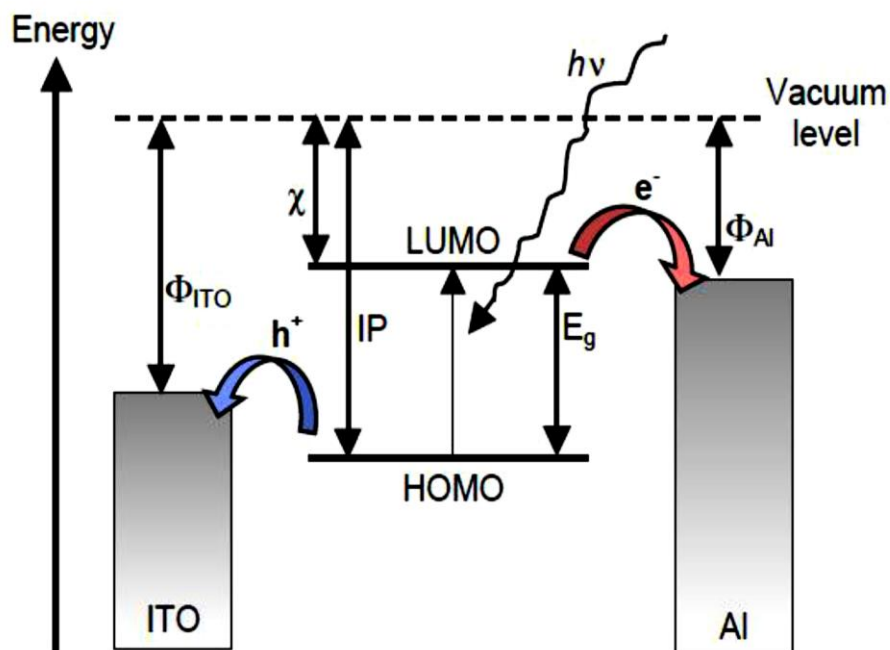


Figure 3.4: Diagram showing energy level and light harvesting of an organic solar cell. Adapted with permission from Ref. [13].

The efficiency of a solar cell is determined by the energy difference (E_g) between the lowest unoccupied molecular orbital (LUMO) and the highest occupied molecular orbital (HOMO). During the oxidation and reduction of an organic molecule, there is an electron transfer process taking place (see Figure 3.5) and the potential change during redox reactions and it can be determined by CV measurements. The electronic bandgap is obtained through the analysis of data obtained by the CV measurements [14]. Cyclic voltammetry is the most useful technique for the characterization of organic materials and estimation of the energy band diagram [15,14,16]. The amount energy required to extract an electron from a molecule is represented by HOMO, which corresponds to oxidation process, and the amount of energy required to inject an electron into a molecule is represented by LUMO, which correspond to reduction process [17]. Cyclic voltammetry method can be utilized to measure these processes by measuring the redox potentials E_{red} and E_{ox} . The energy levels can be calculated using the following empirical Bredas et al [18] equations:

$$E(\text{HOMO}) = -e[E_{ox}(\text{onset}) + 4.4] \quad (8)$$

$$E(\text{LUMO}) = -e[E_{red}(\text{onset}) + 4.4] \quad (9)$$

The bandgap of the material is determined by $E_g = E(LUMO) - E(HOMO)$ difference.

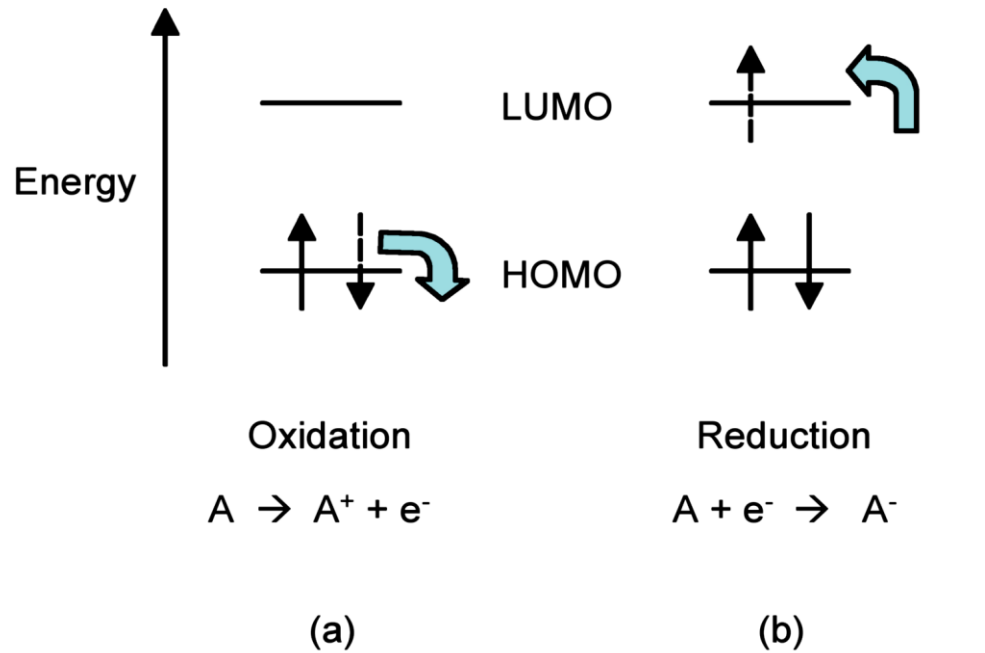
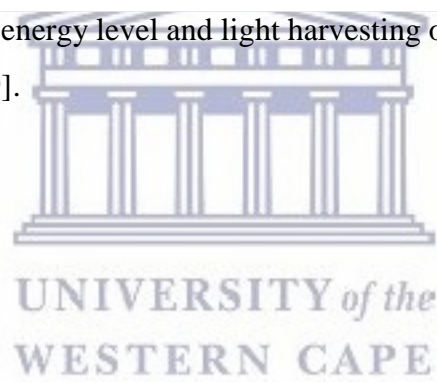


Figure 3.5: Diagram showing energy level and light harvesting of organic solar cell. Adapted with permission from Ref. [19].



BIBLIOGRAPHY

[1] J. L. Knutson, J. D. Martin, and D. B. Mitzi, Tuning the bandgap in hybrid tin iodide perovskite semiconductors using structural templating, *Inorganic Chemistry*. **44**, 4699–4705 (2005).

[2] S. A. Kulkarni, T. Baikie, P. P. Boix, N. Yantara, N. Mathews, S. Mhaisalkar, Band-gap tuning of lead halide perovskite using a sequential deposition process, *Journal of Materials Chemistry*. **2**, 9221–9225 (2014).

[3] G. Xing, N. Mathews, S. Sun, S. S. Lim, Y. M. Lam, M. Grätzel, S. Mhaisalkar, T. C. Sum, Long-range balanced electron- and hole-transport lengths in organic-inorganic CH₃NH₃PbI₃, *Science*. **342**, 344–347 (2013).

[4] A. L. Abdelhady, M. S. Saidaminoy, B. Murali, V. Adinolfi, O. Voznyy, K. Katsev, O. F. Mohammed, and O. M. Bakr, Heterovalent Dopant Incorporation for Bandgap and Type Engineering of Perovskite Crystals, *Journal of the Physical Chemistry Letters*. **7**, 295 – 301 (2016).

[5] M. J. Carnie, C. Charbonneau, M. L. Davies, J. Troughton, T. M. Watson, K. Wojciechowski, H. Snaith and D. A. Worsley, A one-step low temperature processing route for organolead halide perovskite solar cells, *Chemical Communications*. **49**, 7893 (2013).

[6] http://www.hk-phy.org/atomic_world/tem/tem02_e.html [Accessed November 2016]

[7] P. P. Mokoena, O. M. Ntwaeborwa, and H. C. Swarts, MSc dissertation, University of the Free State, South Africa, page 32, 2014.

[8] N. W. Hlongwa, E. Iwuoha, and C. Ikpo, MSc mini-thesis, University of the Western Cape, South Africa, page 33, (2014).

[9] <http://cnx.org/content/m34601/latest/> [Accessed November 2016]

- [10] H. Sezen, and S. Suzer, XPS for chemical-and charge-sensitive analyses, *Thin Solid Films*. **534**, 1-11 (2013).
- [11] G. Blasse, B.C. Grabmair, *Luminescent materials*, Springer-Verlag, (1994)
- [12] R. Ye, R.A. Barron, *Photoluminescence Spectroscopy and its Applications*, Connexions Web site. [Http://cnx.org/content/m38357/1.2/](http://cnx.org/content/m38357/1.2/), Jun 6, 2011.
- [13] S. B. Darling, Block copolymers, *Energy and Environmental Science*. **2**, 1266 (2009).
- [14] A.P. Kulkarni, C.J. Tonzola, A. Babel, and S.A. Jenekhe, Electron transport materials for organic light-emitting diodes, *Chemistry of Materials*. **16**, 4556–4573 (2004).
- [15] M. Al-Ibrahim, H.K. Roth, M. Schroedner, A. Konkin, U. Zhokhavets, G.Gobsch, P.Scharff, and S.Sensfuss, Determination of HOMO and LUMO of [6,6]-Phenyl C61-butyric Acid 3-ethylthiophene Ester and Poly (3-oetyl-thiophene-2,5-diyl) through Voltammetry Characterization, *Organic Electronics*. **6**, 65- 77 (2005).
- [16] B.W.D' Andrade, S. Datta, S.R. Forrest, P.D jurovich, E. Polikarpov, M.E. Thompson, Relationship between the ionization and oxidation potentials for molecular organic semiconductors. **6**, 11 – 20 (2005).
- [17] S. Antohe, *Materiale si dispozitive electronice organice*, Editura Universitatii din Bucuresti, (1996).
- [18] J. L. Bredas, R. Silbey, D. S. Boudreux, and R. R. Chance, Chain-length dependence of electronic and electrochemical properties of conjugated systems: polyacetylene, polyphenylene, polythiophene, and polypyrrole, *Journal of American Chemical Society*. **105(22)**, 6555 (1983).
- [19] D. K. Gosser, J.r., *Cyclic Voltammetry Simulation and Analysis of Reaction Mechanisms*, Wiley – VCH, New York, (1993).

CHAPTER 4

Experimental Results and Discussion

4.1 INTRODUCTION

This chapter discusses in details the obtained experimental results from chapter 3. In this study, spectroscopic techniques which include Ultraviolet-visible spectroscopy (UV-vis), photoluminescence (PL), and potentiodynamic technique which includes cyclic voltammetry (CV) also known as the electrical spectroscopy, were employed to determine the optical and electrochemical bandgap of perovskites under investigation, respectively. The effect of chalcogenide anions (S & Se) on the energy levels, Highest Occupied Molecular Orbitals (HOMOs) and Lowest Unoccupied Molecular Orbitals (LUMOs) of the triiodide perovskite $\text{CH}_3\text{NH}_3\text{PbI}_3$ nanomaterials was also investigated by electrochemical characterization. Finally the bandgaps determined from the two techniques are compared.

4.2 EXPERIMENTAL RESULTS AND DISCUSSION

4.2.1 High Resolution-Transmission Electron Microscopy (HR-TEM)

The HR-TEM images were collected to determine the morphology and particle size of the synthesised triiodide perovskite nanomaterials $\text{CH}_3\text{NH}_3\text{PbI}_3$. The aim of this experiment was to interrogate the morphology of the synthesized triiodide perovskite nanomaterials. The micrograph images are shown in Figure 4.1.

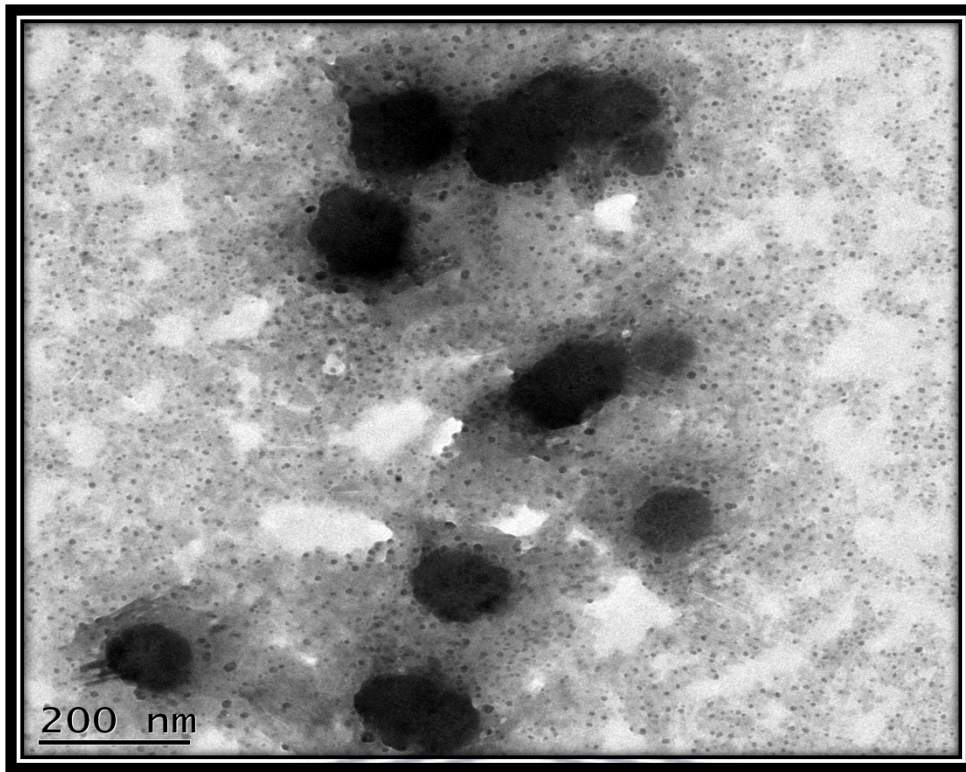


Figure 4.1: TEM micrograph of triiodide perovskite $\text{CH}_3\text{NH}_3\text{PbI}_3$ nanoparticles.

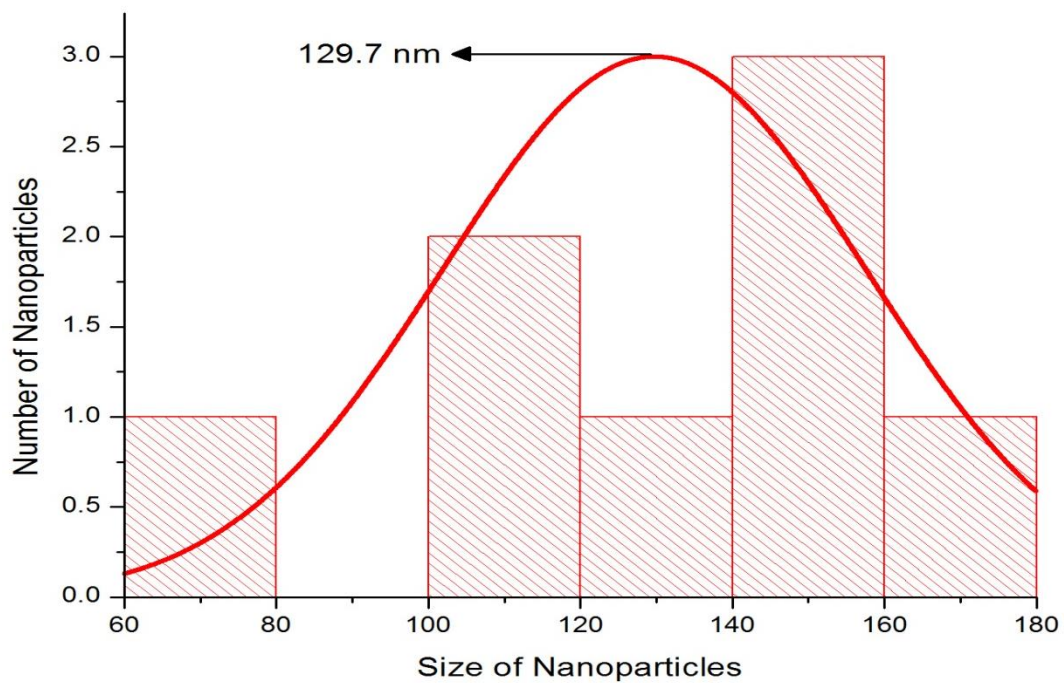
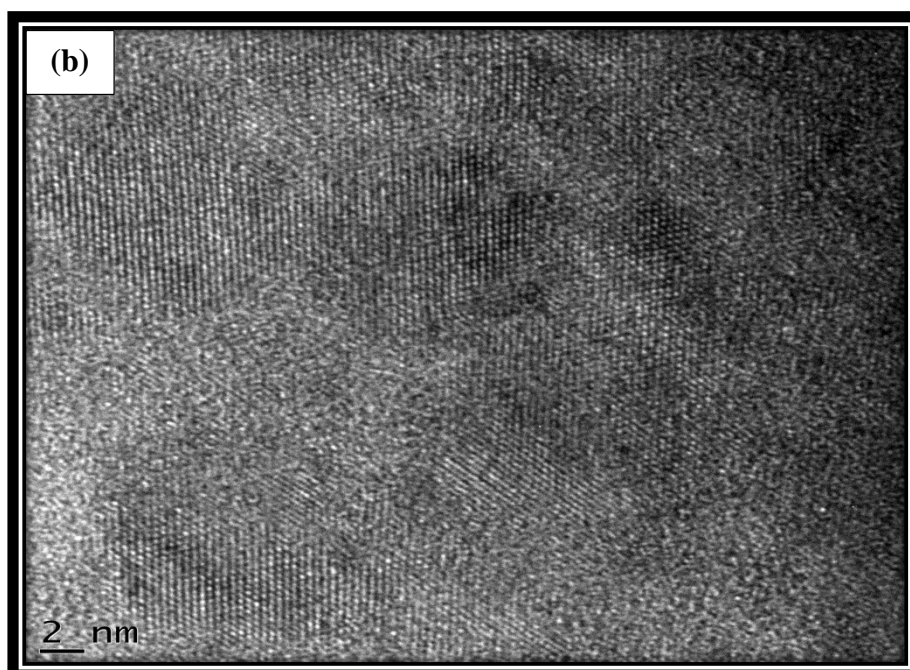
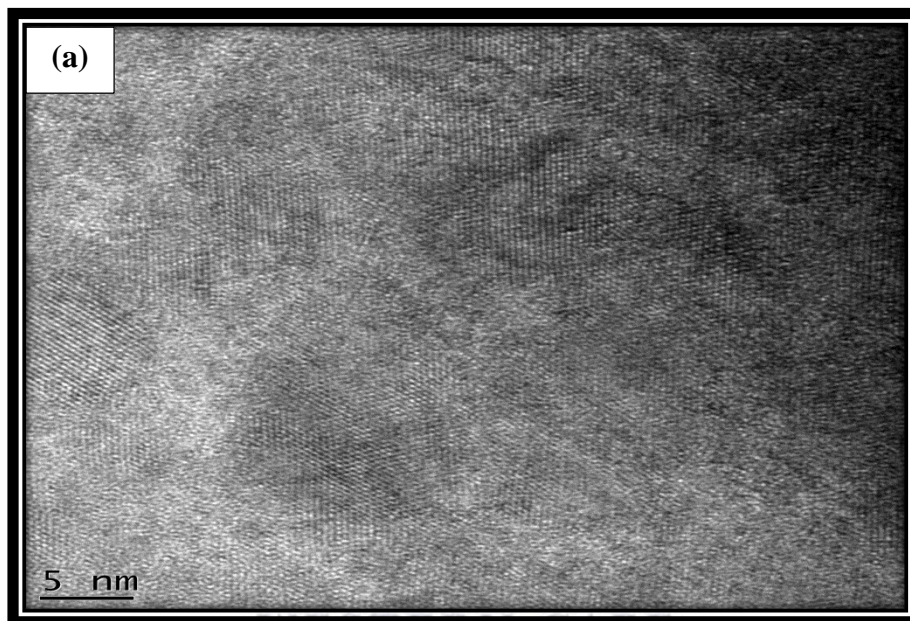


Figure 4.2: Particle size distribution of triiodide perovskite $\text{CH}_3\text{NH}_3\text{PbI}_3$ material.

The TEM image in Figure 4.1 shows hexagonal perovskite nanoparticles. The morphology of the perovskite nanoparticles depends on the type of solvent used during the synthesis. In this study a high polar solvent mixture of dimethyl formamide and dimethyl sulfoxide, (DMF)/(DMSO) was used during synthesis and a hexagonal morphology was anticipated as reported in literature [1]. The particle size distribution was calculated using image J software for nanoparticles and the average particle size was determined as 129.7 nm as shown in the distribution bar graph fitted under curve in Figure 4.2.



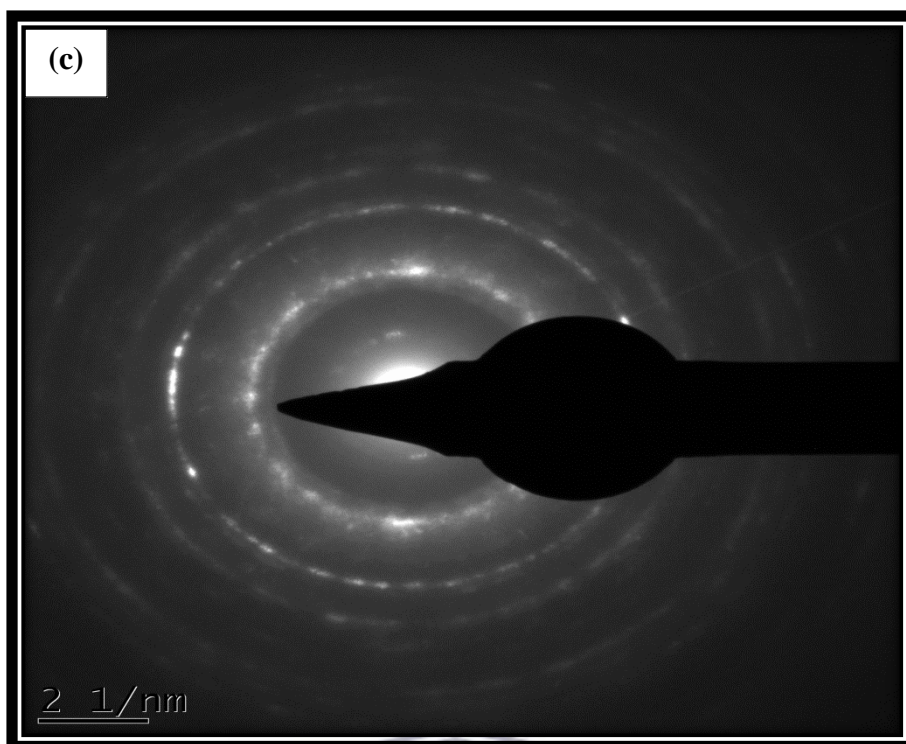


Figure 4.3: TEM micrograph of triiodide perovskite $\text{CH}_3\text{NH}_3\text{PbI}_3$ at higher magnifications (a) – (b) and (c) is the selected area electron diffraction (SAED) patterns .

It was seen from Figure 4.3 (a) and (b) that the triiodide perovskite $\text{CH}_3\text{NH}_3\text{PbI}_3$ nanomaterials under investigation had a polycrystalline morphology with crystal planes pointing at different directions, as reported in literature [1]. The high crystallinity of the nanomaterials was further confirmed by the electron diffraction rings shown in (c). These images confirmed the successful synthesis of polycrystalline perovskite material with hexagonal morphology.

4.2.2 Energy Dispersive x-ray Spectroscopy (EDS)

The elemental composition was investigated by EDS technique and the spectrum showed the main elements present in the structure of the triiodide perovskite nanomaterials $\text{CH}_3\text{NH}_3\text{PbI}_3$ which comprises of Pb, I₂ and C. The Cu was from the copper grid used during sample preparation. Nitrogen and hydrogen did not show up in the spectrum and the oxygen O element was from DMSO solvent used during synthesis. The reason why H was not detected in the spectrum is because EDS is related to the K-shells which are not the valence shell.

Hydrogen doesn't have a K-shell, however, it has a K-shell in a covalent bonding and this electron in a covalent bonding is shared.

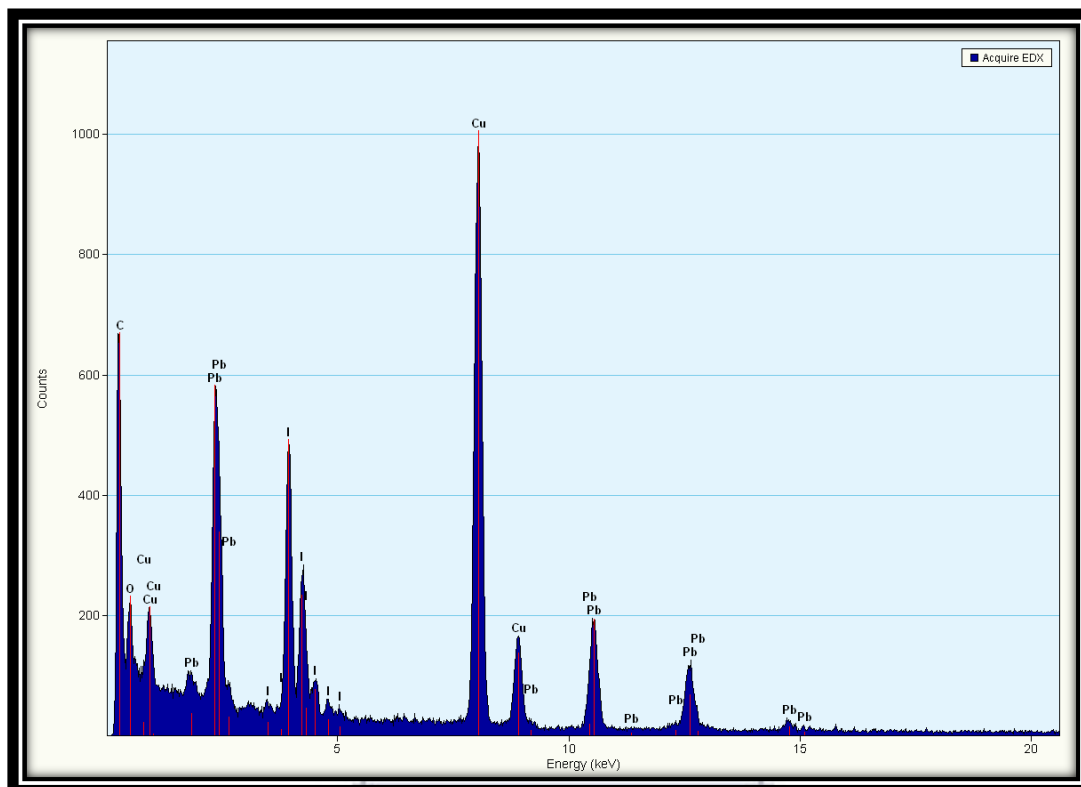


Figure 4.4: EDS spectrum for the elemental composition of triiodide perovskite $\text{CH}_3\text{NH}_3\text{PbI}_3$ materials on the Cu grid.

4.2.3 Spectroscopic studies by Ultra-violet (UV-vis) spectroscopy

The aim of these experiments was to determine the transitions that take place during absorption of electromagnetic radiation by triiodide perovskite $\text{CH}_3\text{NH}_3\text{PbI}_3$ materials and the mixed ions perovskites $\text{CH}_3\text{NH}_3\text{PbI}_2\text{S}$ & $\text{CH}_3\text{NH}_3\text{PbI}_2\text{Se}$ and to also determine the optical bandgap from the cut-off wavelengths. The spectroscopic studies were also conducted for mixed ions perovskites $\text{CH}_3\text{NH}_3\text{PbI}_2\text{S}$ and $\text{CH}_3\text{NH}_3\text{PbI}_2\text{Se}$ to investigate the resulting effects on the absorption of the triiodide perovskite. The cut-off wavelengths were determined from the absorption spectrum as shown in Figure 4.5 below.

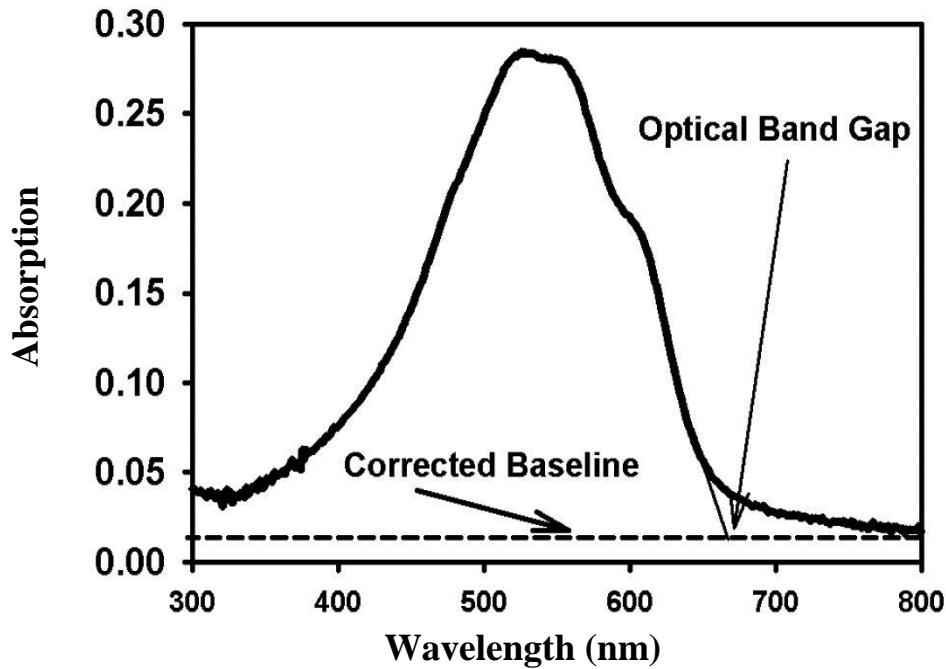


Figure 4.5: Absorption spectrum and optical bandgap of P3OT. Adapted with permission from Ref [2].

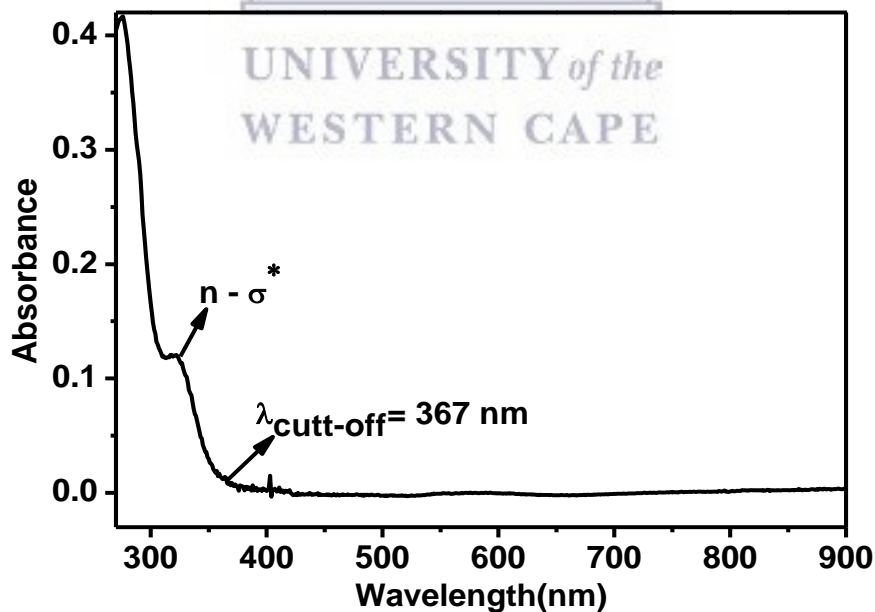


Figure 4.6: UV-vis spectra of triiodide perovskite $\text{CH}_3\text{NH}_3\text{PbI}_3$ nanomaterials.

Figure 4.6 shows an absorption spectrum of the triiodide perovskite material. This is a spectrum of a perovskite solution and corresponds well with the one reported in literature [3]. The shape of the spectrum further serves a qualitative confirmation for the triiodide

perovskite solution. An absorption transition $n - \sigma^*$ was observed at the wavelength of 322.18 nm and a cut-off wavelength of absorption was observed at 376 nm.

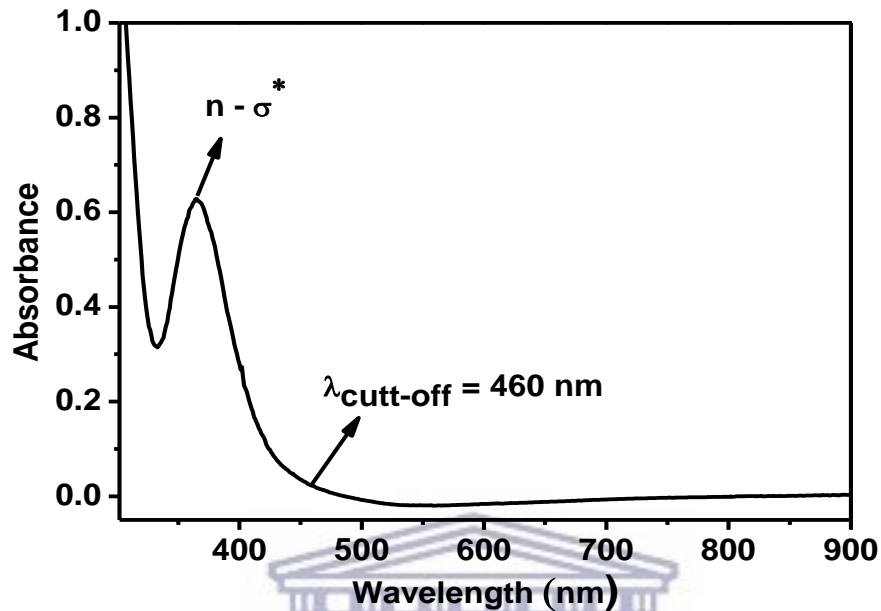


Figure 4.7: UV-vis spectra of mixed perovskite $\text{CH}_3\text{NH}_3\text{PbI}_2\text{S}$ nanomaterials.

Figure 4.7 shows an absorption spectrum of the mixed ions $\text{CH}_3\text{NH}_3\text{PbI}_2\text{S}$ perovskite nanomaterials. The shape of the spectrum retained the shape of the spectrum for triiodide perovskite $\text{CH}_3\text{NH}_3\text{PbI}_3$ in Figure 4.6, which implies that the perovskite structure was preserved after incorporation of the sulphur (S). A red-shift in wavelength was observed. An absorption transition $n - \sigma^*$ was observed at the wavelength of 365.62 nm and the cut-off wavelength of absorption was observed at 460 nm.

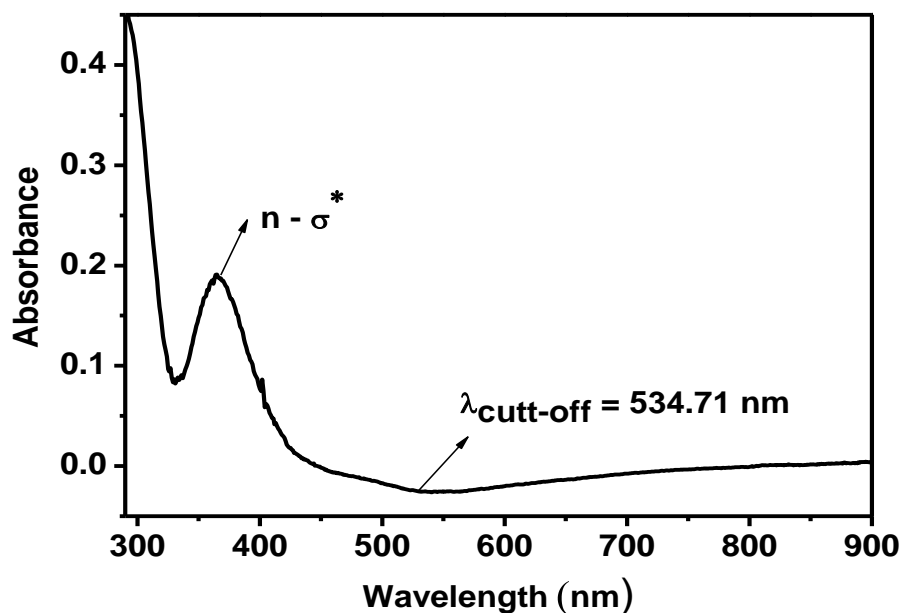


Figure 4.8: UV-vis spectra of mixed ions perovskite $\text{CH}_3\text{NH}_3\text{PbI}_2\text{Se}$ nanomaterials.

Figure 4.8 shows an absorption spectrum of the mixed ions $\text{CH}_3\text{NH}_3\text{PbI}_2\text{Se}$ perovskite materials. The shape of the spectrum also retained the shape of the spectrum for triiodide perovskite $\text{CH}_3\text{NH}_3\text{PbI}_3$ in Figure 4.6, which implies that the perovskite structure was also preserved after incorporation of the selenium (Se). A red-shift in wavelength was observed. An absorption transition $n - \sigma^*$ was observed at the wavelength of 367.30 nm and the cut-off wavelength of absorption was observed at 534.71 nm.

The optical bandgaps of the perovskite compounds, $\text{CH}_3\text{NH}_3\text{PbI}_3$, $\text{CH}_3\text{NH}_3\text{PbI}_2\text{S}$ and $\text{CH}_3\text{NH}_3\text{PbI}_2\text{Se}$ were determined using the equation 5: $E = \frac{hc}{\lambda_{\text{cut-off}}} = \frac{1240}{\lambda_{\text{cut-off}}}$ and the results are summarized in table 1 below.

Table 4.1. Calculated optical bandgaps of the perovskite materials.

Compound	Cut-off Wavelength(nm)	Optical Bandgap E_g (eV)
$\text{CH}_3\text{NH}_3\text{PbI}_3$	367.00	3.40
$\text{CH}_3\text{NH}_3\text{PbI}_2\text{S}$	460.00	2.70
$\text{CH}_3\text{NH}_3\text{PbI}_2\text{Se}$	534.71	2.30

From table 1 it was observed that the incorporation of the chalcogenide anions resulted with redshift in the absorption wavelength of the triiodide perovskite $\text{CH}_3\text{NH}_3\text{PbI}_3$ materials. The

absorption was widened from 367 nm to 460 nm for S, and from 367 nm to 534 nm for Se doped materials, respectively. This resulted in the narrowing of the optical bandgap from 3.40 eV to 2.7 eV for materials doped with S, and from 3.40 eV to 2.30 eV for materials doped with Se. It can be concluded that indeed the incorporation of the chalcogenide anions into the structure of the triiodide $\text{CH}_3\text{NH}_3\text{PbI}_3$ perovskite materials induced a redshift in the absorption spectrum. This is due to the fact that the chalcogenide anions have a lower electronegativity than iodine; S (2.58) & Se (2.55) versus I_2 (2.66). Selenium is the least electronegative anion and hence $\text{CH}_3\text{NH}_3\text{PbI}_2\text{Se}$ had the smallest bandgap, 2.30 eV. It has been reported in literature that the bandgap of organometallic halide perovskite materials can be decreased by lowering the Pauling electronegativity between the metal cation and halide anion to improve absorption (employing least electronegative anions). It has further been shown by experimental studies that the absorption of $\text{CH}_3\text{NH}_3\text{PbX}_3$ shifts to the blue region of the solar spectrum with changing anions from I^- to Br^- to Cl^- (increase in electronegativity from I^- to Cl^-) [4,5]. Therefore, the resulting trends in cut-off wavelengths for absorption and the corresponding optical bandgaps shown in table 1 were anticipated from a decreasing trend in electronegativity from I_2 (2.66) to S (2.58) to Se (2.58).

However, the obtained bandgap 3.40 eV for $\text{CH}_3\text{NH}_3\text{PbI}_3$ is bigger than the one reported in literature 1.57 eV [6-11] for $\text{CH}_3\text{NH}_3\text{PbI}_3$ due to the fact that in this project the UV-vis measurements were done with perovskite solution (perovskite precursor) and not with annealed perovskite thin films (polycrystalline perovskite nanocrystals). Therefore, thin-film samples of the prepared solutions of $\text{CH}_3\text{NH}_3\text{PbI}_3$, $\text{CH}_3\text{NH}_3\text{PbI}_2\text{S}$ and $\text{CH}_3\text{NH}_3\text{PbI}_2\text{Se}$ should be prepared to shift the absorptions onsets towards the near infrared region of the solar spectrum. Nonetheless, the obtained results indicated that the chalcogenide anions S & Se as potentials dopants for the narrowing the bandgap of organometallic halide perovskites.

4.2.4 Spectroscopic studies by photoluminescence (PL) spectroscopy

The optical properties of the perovskite materials were further probed by photoluminescence spectroscopy. The results obtained are shown in Figure 4.9, Figure 4.10 and Figure 4.11.

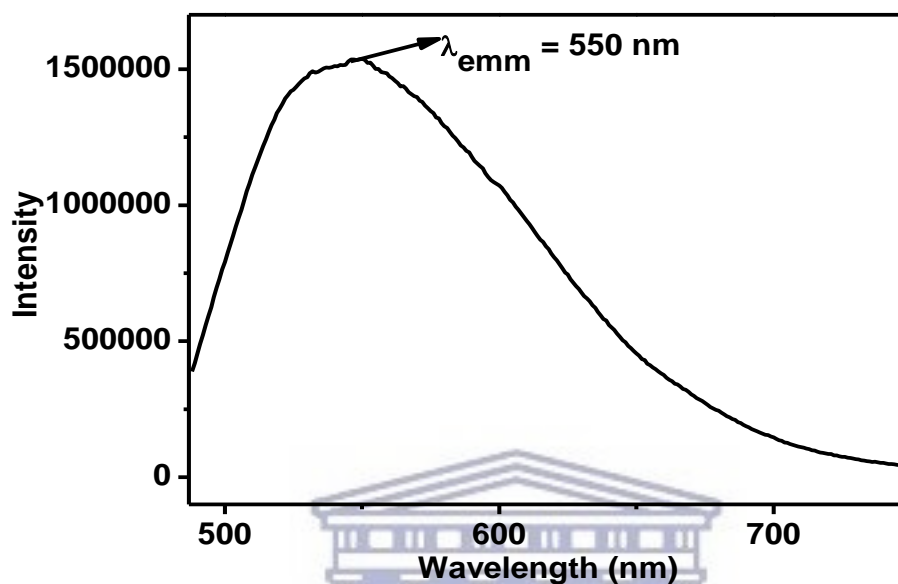


Figure 4.9: PL spectrum of triiodide perovskite CH₃NH₃PbI₃.

The triiodide perovskite CH₃NH₃PbI₃ materials exhibited luminescence at a wavelength of 550 nm.

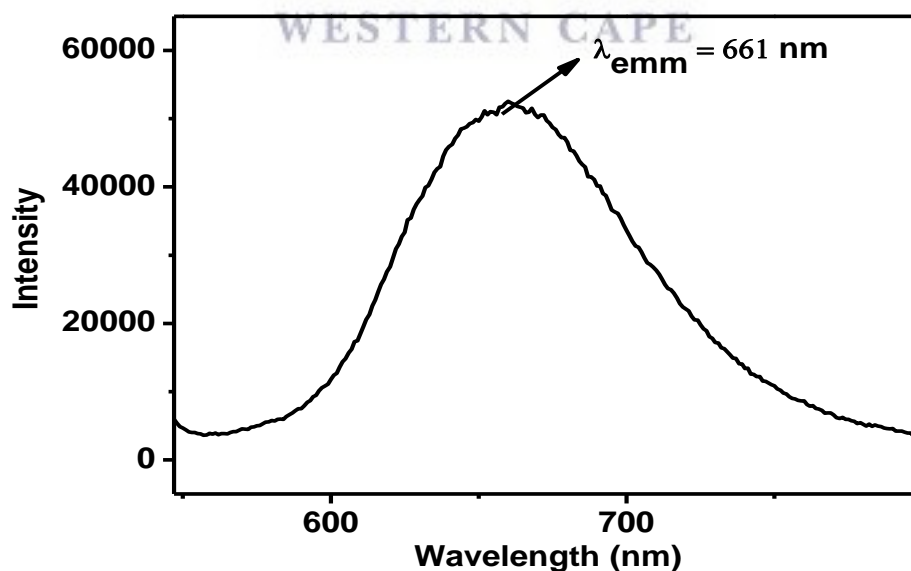


Figure 4.10: PL spectrum of mixed ions perovskite CH₃NH₃PbI₂S.

The mixed ions perovskite CH₃NH₃PbI₂S perovskite materials exhibited luminescence at a wavelength of 661 nm.

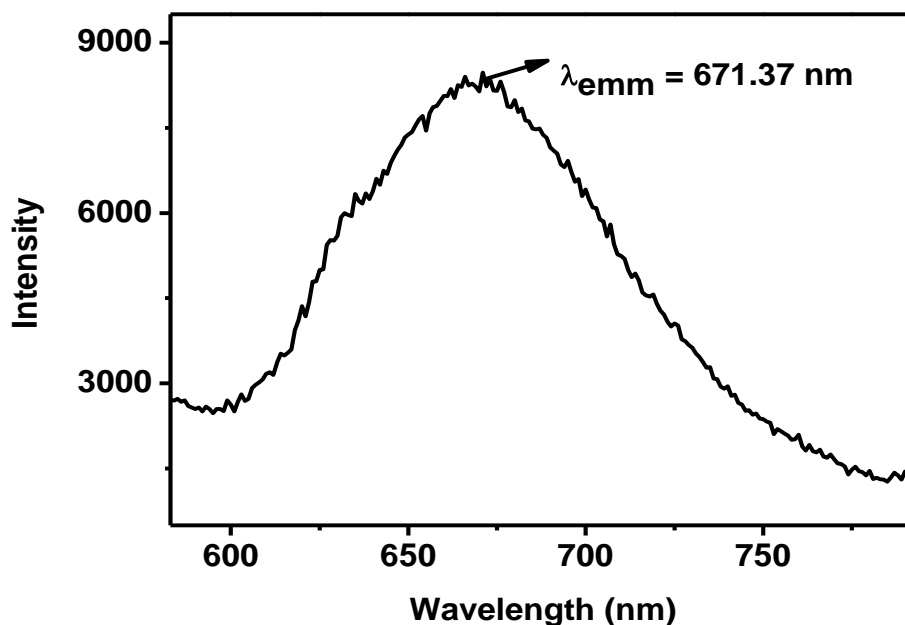


Figure 4.11: PL spectrum of the mixed ions perovskite $\text{CH}_3\text{NH}_3\text{PbI}_2\text{Se}$.

The mixed ions perovskite $\text{CH}_3\text{NH}_3\text{PbI}_2\text{S}$ perovskite materials exhibited luminescence at a wavelength of 671.37 nm. The results are summarized in table 4.2 below.

Table 4.2 Photoluminescence emissions of organometallic perovskite materials.

Compound	Emission Wavelength (nm)
$\text{CH}_3\text{NH}_3\text{PbI}_3$	550.00
$\text{CH}_3\text{NH}_3\text{PbI}_2\text{S}$	661.00
$\text{CH}_3\text{NH}_3\text{PbI}_2\text{Se}$	671.37

During photoluminescence experiment, the incident photon excites an electron from the filled valence band and promotes it to the next empty band known as the conduction band, leaving a hole behind. The electron and hole relaxes to the bottom of the conduction band and top of the valence band, respectively. The electron and hole recombine emitting a photon whose energy is equal to the bandgap of the material, i.e. $\text{CH}_3\text{NH}_3\text{PbI}_3$, $\text{CH}_3\text{NH}_3\text{PbI}_2\text{S}$ and $\text{CH}_3\text{NH}_3\text{PbI}_2\text{Se}$. The photo-emission wavelengths of the perovskite materials at different wavelengths indicate that the electron-hole pairs created by photo-excitation undergo a radiative recombination. The life-times of the electron-hole ($e^- h^+$) can be further probed by time resolve photoluminescence spectroscopy (tr-PL).

The radius of the materials is inversely related to the bandgap, i.e. the bigger the radius is the smaller the bandgap and this means the emission at a particular wavelength is dictated by

particle size of the material. From the results obtained in Figure 4.9, 4.10 and 4.11, the emission wavelengths shifted from 550 nm to 661 nm for S doped perovskite $\text{CH}_3\text{NH}_3\text{PbI}_2\text{S}$ and from 550.00 nm to 671.37 nm for Se doped perovskite $\text{CH}_3\text{NH}_3\text{PbI}_2\text{Se}$. The trend observed in the emission wavelengths complements the trend observed in the absorption wavelengths of the materials indicating that the photo-emissions were oriented by the bandgap of the materials. Therefore, the incorporation of the chalcogenide anions resulted in an increase in the radius of the triiodide perovskite material. It can be further concluded that indeed the incorporation of the chalcogenide anions S and Se into the structure of the triiodide perovskite $\text{CH}_3\text{NH}_3\text{PbI}_3$ modulated the bandgap to lower values.

4.2.5 Electrochemical characterization by Cyclic Voltammetry (CV)

Electrochemical characterization by cyclic voltammetry is one of the best methods for a wide range of applications. In this study, cyclic voltammetry was used to interrogate the electrochemical behaviour and electronic properties of the organometallic halide perovskite under investigation. The other aim of this experiment was to confirm the successful incorporation of the chalcogenide anions (S & Se) into the structure of the triiodide perovskite.

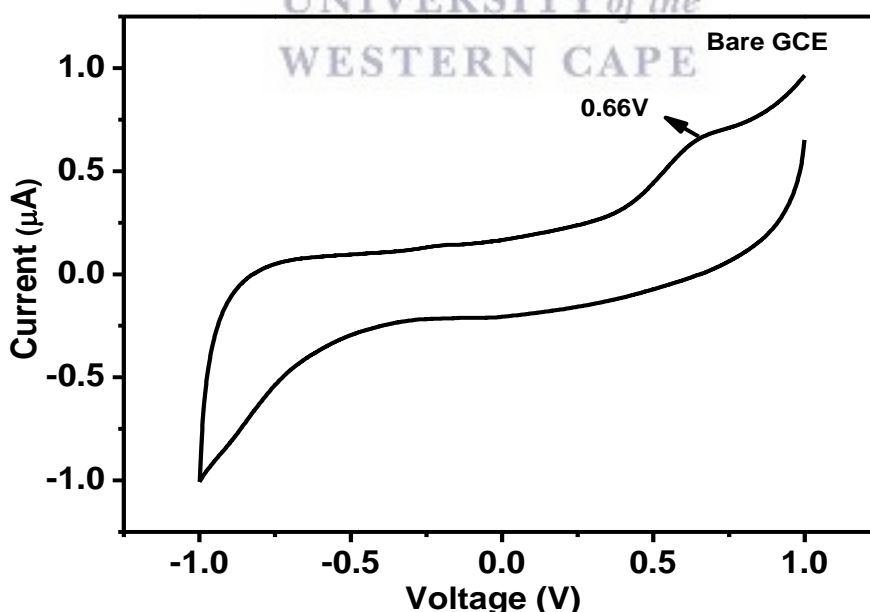


Figure 4.12: CV of Bare GCE in 0.1 M LiClO₄ at 50 mV/s.

The bare glassy carbon electrode showed an anodic peak at 0.6 V in 0.1 M LiClO₄ electrolyte solution. This peak was also considered during the interpretation of the cyclic voltammograms for all the organometallic halide perovskite materials that follows.

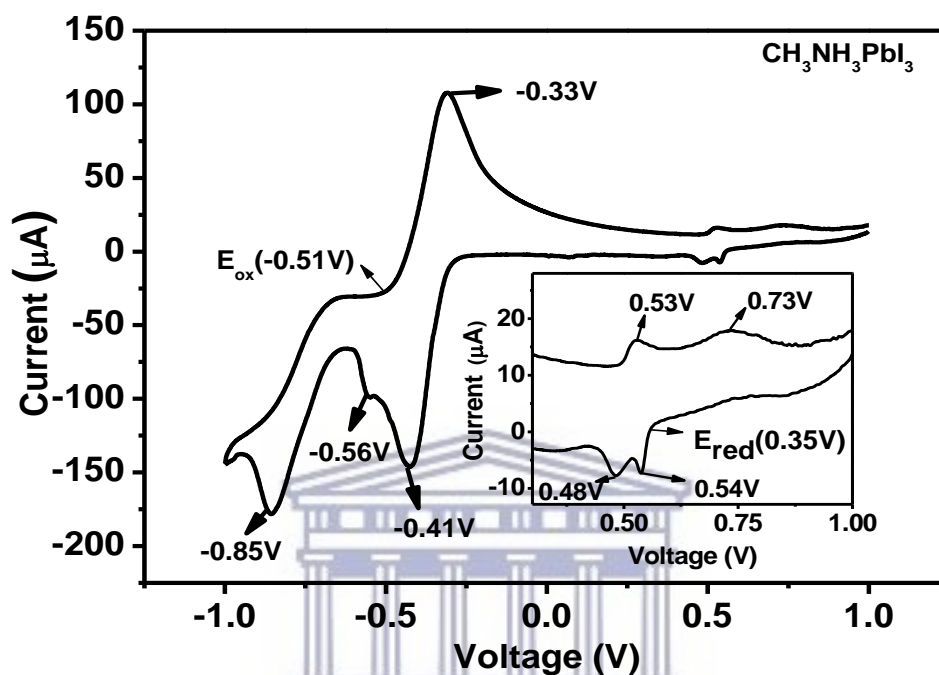
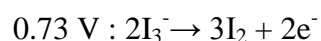


Figure 4.13: CV of triiodide perovskite CH₃NH₃PbI₃ in 0.1M LiClO₄ at 50 mv/s.

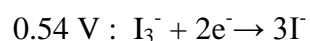
Interpretation of the cyclic voltammogram:

Anodic peak at -0.33 V is due to hydrogen adsorption. Cathodic peaks at -0.41 V and -0.85 V are attributed to hydrogen desorption with hydrogen evolution starting at -0.85 V. Cathodic peak at -0.56 V is attributed to Pb²⁺ → Pb⁰.

Inset: Anodic peaks: 0.53 V : 3I⁻ → I₂ + 2e⁻



Cathodic peaks: 0.48 V : 3I₂ + 2e⁻ → 2I₃⁻



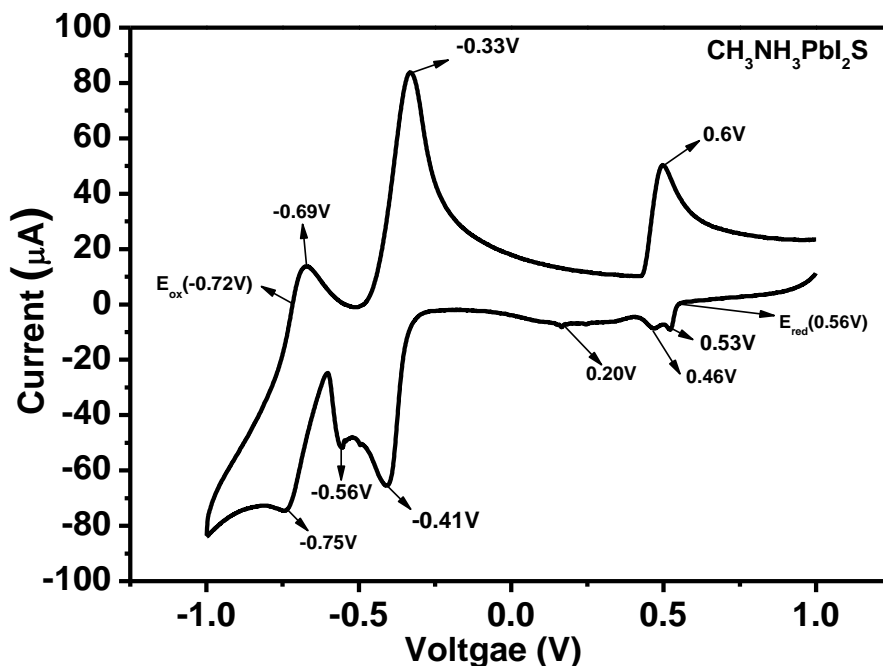


Figure 4.14: CV of mixed ions perovskite $\text{CH}_3\text{NH}_3\text{PbI}_2\text{S}$ in 0.1M LiClO_4 at 50 mv/s.

Interpretation of the cyclic voltammogram:

Anodic peaks at -0.3 V and -0.69 V corresponds to hydrogen adsorption. Anodic peak at 0.6 V is from the bare GCE. Cathodic peaks at -0.41 V and -0.75 V are attributed to hydrogen desorption with hydrogen evolution starting at -0.75 V.

Cathodic peaks; $0.46 \text{ V} : 3\text{I}_2 + 2\text{e}^- \rightarrow 2\text{I}_3^-$

$0.53 \text{ V} : \text{I}_3^- + 2\text{e}^- \rightarrow 3\text{I}^-$

$0.20 \text{ V} : \text{S}_2^{2-} + 2\text{H}^+ + 2\text{e}^- \rightarrow 2\text{HS}^-$

$-0.56 \text{ V} : \text{Pb}^{2+} \rightarrow \text{Pb}^0$

The cyclic voltammogram of mixed ions perovskite $\text{CH}_3\text{NH}_3\text{PbI}_2\text{S}$ differed significantly with the one obtained for the triiodide perovskite $\text{CH}_3\text{NH}_3\text{PbI}_3$ indicating that there was a change in the structure due to the incorporation of the S anion. The successful incorporation of S was sensed by cyclic voltammetry scan at cathodic peak of $0.20 \text{ V} : \text{S}_2^{2-} + 2\text{H}^+ + 2\text{e}^- \rightarrow 2\text{HS}^-$. There are numerous reduction reactions for S in different oxidation states taking place at different potentials and this study it was sensed at S^{2-} as expected.

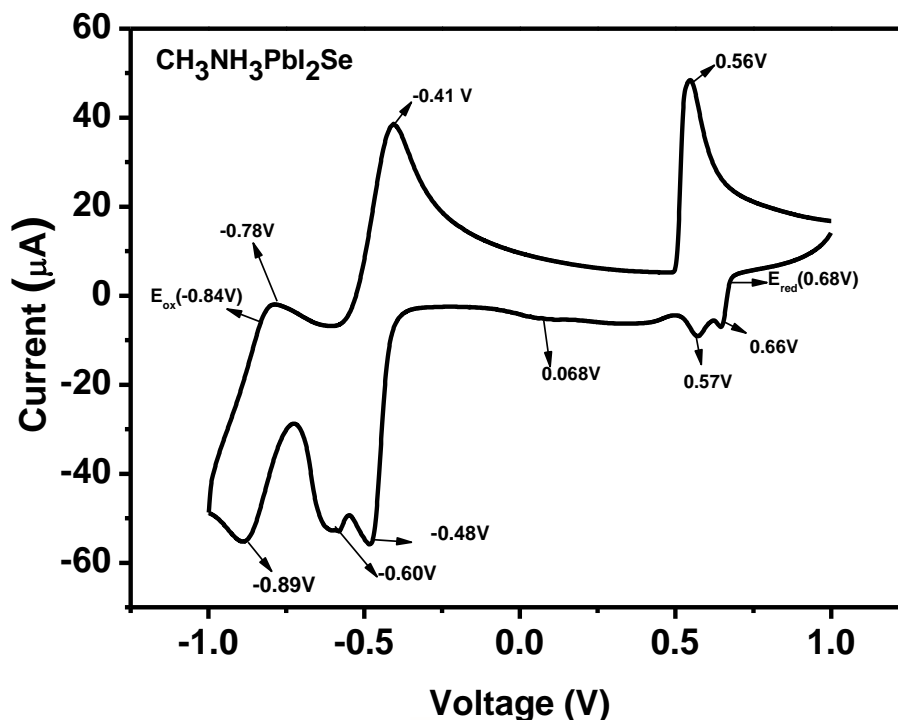


Figure 4.15: CV of mixed ions perovskite $\text{CH}_3\text{NH}_3\text{PbI}_2\text{Se}$ in 0.1M LiClO_4 at 50 mv/s.

Interpretation of the cyclic voltammogram:

Anodic peaks at -0.41 V and -0.78 V corresponds to hydrogen adsorption. Anodic peak at 0.56 V is from the bare GCE. Cathodic peaks at -0.48 V and -0.89 V are attributed to hydrogen desorption with hydrogen evolution starting at -0.89 V.

Cathodic peaks; 0.57 V : $3\text{I}_2 + 2\text{e}^- \rightarrow 2\text{I}_3^-$

0.66 V : $\text{I}_3^- + 2\text{e}^- \rightarrow 3\text{I}^-$

0.07 V : $\text{SeO}_4^{2-} + 2\text{e}^- + \text{H}_2\text{O} \rightarrow \text{SeO}_3^{2-} + 2\text{OH}^-$

-0.60 V : $\text{Pb}^{2+} \rightarrow \text{Pb}^0$

The cyclic voltammogram of mixed ions perovskite $\text{CH}_3\text{NH}_3\text{PbI}_2\text{Se}$ differed significantly with the one obtained for the triiodide perovskite $\text{CH}_3\text{NH}_3\text{PbI}_3$ indicating that there was a change in the structure due to the incorporation of the Se anion. The successful incorporation was sensed by cyclic voltammetry scan at cathodic peak of 0.068 V : $\text{SeO}_4^{2-} + 2\text{e}^- + \text{H}_2\text{O} \rightarrow \text{SeO}_3^{2-} + 2\text{OH}^-$. There are numerous reduction reactions for Se in different oxidation states taking place at different potentials and in this study it was sensed at Se^{2-} bonded to ClO_4^- from the electrolyte solution.

The electrochemical bandgaps of the perovskite compounds were determined from the oxidation and reduction onsets using the equation: $E_g = E(LUMO) - E(HOMO)$. The energies of the HOMOs and LUMOs were determined using equation 8 and 9 in chapter 3. The results are summarized in table 4.3 below.

Table 4.3 Calculated electrochemical bandgaps of the perovskite compounds.

Compound	E_{ox}^{onset} vs. Ag/AgCl(V)	HOMO (eV)	E_{red}^{onset} vs Ag/AgCl(V)	LUMO (eV)	E_g (CV)	E_g(UV)
CH ₃ NH ₃ PbI ₃	-0.51	3.89	0.35	4.75	0.86	3.40
CH ₃ NH ₃ PbI ₂ S	-0.72	3.68	0.56	4.96	1.28	2.70
CH ₃ NH ₃ PbI ₂ Se	-0.84	3.56	0.68	5.08	1.52	2.30

It was observed from table 4.3 that the incorporation of chalcogenide anions (S and Se) resulted with a decrease in the energy of HOMOs from 3.89 eV (CH₃NH₃PbI₃) to 3.68 eV for S doped perovskite (CH₃NH₃PbI₂S) and from 3.89 eV to 3.56 eV for Se doped perovskite (CH₃NH₃PbI₂Se). This trend came as no surprise since I⁻ is the highest electronegative anion and therefore more energy will be required to oxidize the triiodide perovskite CH₃NH₃PbI₃, whereas S²⁻ and Se²⁻ are the least electronegative anions and therefore lesser energy will be required to oxidise the organo-chalcogenic perovskites; CH₃NH₃PbI₂S and CH₃NH₃PbI₂Se. An increase in energy of the LUMOs was also observed from 4.75 eV (CH₃NH₃PbI₃) to 4.96 eV for S doped perovskite (CH₃NH₃PbI₂S) and from 4.75 eV to 5.08 eV for Se doped perovskite (CH₃NH₃PbI₂Se). This also came as no surprise since I⁻ is the highest electronegative anion and therefore less energy will be required to reduce the triiodide perovskite CH₃NH₃PbI₃, whereas S²⁻ and Se²⁻ the least electronegative and therefore more energy will be required to reduce the organo-chalcogenic perovskites; CH₃NH₃PbI₂S and CH₃NH₃PbI₂Se. A decrease in the energy of the HOMOs (valence band) implied that lesser energy will be required to knock out the electrons from the valence band to the conduction band (LUMOs) to create photocurrent, making organo-chalcogenic perovskites potential candidates for solar cell application.

Opposite trends in electrochemical band gaps and optical bandgaps were observed from table 4.3. These trends were the results of the same structural changes induced by the incorporation of the chalcogenide anions into the triiodide perovskite structure. The electrochemical

bandgaps obtained were lesser than the optical bandgaps and this could be attributed to fast electrochemical reactions which causes the peaks to shift to less extreme potentials. The presence of S^{2-} and Se^{2-} were confirmed at cathodic peaks 0.20V and 0.068V, respectively. Electrochemistry studies (CV) also demonstrated that all the materials under investigation are redox active, indicating that they are conductive and this makes them suitable candidates for solar cells application.



BIBLIOGRAPHY

- [1] Z. Chen, H. Li, Y. Tang, X. Huang, D. Ho, and C.-S Lee, Shape-control synthesis of organolead halide perovskite nanocrystals and their tunable optical absorption, *Materials Research Express*. **1**, 015034 (2014).
- [2] A. Shafiee, M.-M. Salleh, and M. Yahaya, Determination of HOMO and LUMO of [6,6]-Phenyl C61 – butyric Acid 3- ethylthiophene Ester and Poly (3-octyl-thiophene-2,5-diyl) through Voltammetry Characterization, *Sains Malaysiana*. **40(2)**, 173-176 (2011).
- [3] J.S. Manse, M. J. Saidaminor, J. A. Christians, O. M. Baks, and P. V. Kamat, Making and Breaking of Lead Halide Perovskites, *Accounts of Chemical Research*. **49**, 330 – 338 (2016).
- [4] S. A. Kulkarni, T. Baikie, P. P. Boix, N. Yantara, N. Mathews, S. Mhaisalkar, Band-gap tuning of lead halide perovskite using a sequential deposition process, *Journal of Materials Chemistry*. **2**, 9221–9225 (2014).
- [5] G. Xing, N. Mathews, S. Sun, S. S. Lim, Y. M. Lam, M. Grätzel, S. Mhaisalkar, T. C. Sum, Long-range balanced electron- and hole-transport lengths in organic-inorganic CH₃NH₃PbI₃, *Science*. **342**, 344–347 (2013).
- [6] A. Kojima, K. Teshima, Y. Shirai, and T. Miyasaka, Organometal Halide Perovskites as Visible-Light Sensitizers for Photovoltaic Cells, *Journal of the American Chemical Society*. **131**, 6050–6051 (2009).
- [7] L. Etgar, P. Gao, Z. Xue, Q. Peng, A. K. Chandiran, B. Liu, Nazeeruddin, K. Md, M. Gratzel, Mesoscopic CH₃NH₃PbI₃/TiO₂ Heterojunction Solar Cells, *Journal of the American Chemical Society*. **134**, 17396– 17399 (2012).
- [8] H.-S. Kim, C.-R. Lee, J.-H. Im, K.-B. Lee, T. Moehl, A. Marchioro, S.-J. Moon, R. Humphry-Baker, J.-H. Yum, Moser et al., Lead Iodide Perovskite Sensitized All-Solid-State Submicron Thin Film Mesoscopic Solar Cell with Efficiency Exceeding 9%, *Science Reports*. **2**, 591 (2012).

[9] M. M. Lee, J. Teuscher, T. Miyasaka, T. N. Murakami, H. J. Snaith, Efficient Hybrid Solar Cells Based on Meso-Superstructured Organometal Halide Perovskites, *Science*. **338**, 643–647 (2012).

[10] J. Burschka, N. Pellet, S.-J. Moon, R. Humphry-Baker, P. Gao, M. K. Nazeeruddin, M. Gratzel, Sequential Deposition as a Route to High-Performance Perovskite-Sensitized Solar Cells, *Nature*. **499**, 316–319 (2013).

[11] M. Liu, M. B. Johnston, H. J. Snaith, Efficient Planar Heterojunction Perovskite Solar Cells by Vapour Deposition, *Nature*. **501**, 395–398 (2013).



CHAPTER 5

Conclusive Summary and Recommendations

5.1 CONCLUSIVE SUMMARY

The chief aim of this study was to narrow the bandgap and widen the absorption edge of the triiodide perovskite $\text{CH}_3\text{NH}_3\text{PbI}_3$ by doping or incorporation of the chalcogenide anions S & Se into the structure of triiodide perovskite to prepare new mixed ions perovskites with lower bandgaps; $\text{CH}_3\text{NH}_3\text{PbI}_2\text{S}$ and $\text{CH}_3\text{NH}_3\text{PbI}_2\text{Se}$, for application in single-junction solar cells. The narrowing of bandgap of organometallic halide perovskite materials has been reported to result in improved open circuit voltage, photocurrent density and the efficiency of solar cells. It has been reported in literature that one of the ways to narrow the bandgap of organometallic halide perovskites is by decreasing the Pauling electronegativity difference between the metal cation Pb and the halide anions or simply by employing the anions with the least electronegativity. Pauling electronegativity differences between PbI_2 , PbS and PbSe were calculated as 0.33, 0.25, and 0.22, respectively. A decrease in Pauling electronegativity difference was observed since the electronegativities of all chalcogenide anions; S (2.58) and Se (2.55), are all lower than the electronegativity of I_2 (2.66) and hence a decrease in bandgap was anticipated for chalcogenide incorporated (doped) perovskite materials, i.e. organo-chalcogenic perovskites: $\text{CH}_3\text{NH}_3\text{PbI}_2\text{S}$ and $\text{CH}_3\text{NH}_3\text{PbI}_2\text{Se}$. The triiodide perovskite nanomaterials $\text{CH}_3\text{NH}_3\text{PbI}_3$ were synthesized and characterized by HR-TEM coupled with EDS to interrogate the morphology, crystallinity and elemental composition. The polycrystalline nanomaterials of particle size 129.7 nm with hexagonal morphology were characterized by HR-TEM. The elemental composition for $\text{CH}_3\text{NH}_3\text{PbI}_3$ was confirmed by EDS and C, Pb, and I showed up in the spectrum. Chalcogenide anions S and Se were then incorporated into the structure of the triiodide perovskite. Spectroscopic studies by UV-vis and PL were conducted to probe the electronic properties of all the perovskite nanomaterials under investigation. The incorporation of chalcogenide anions resulted in widening of the absorption from 367 nm to 460 nm for S, and from 367 nm to 534 nm for Se doped materials. These resulted in the narrowing of the optical bandgap from 3.40 eV to 2.7 eV for materials

doped with S, and from 3.40 eV to 2.30 eV for materials doped with Se, respectively. The electronic properties of the materials were further probed by photoluminescence spectroscopy. The photo-emissions of the perovskite materials at different wavelengths indicated that the electron-hole pairs created by photo-excitation undergo a radiative recombination. The trend observed in the emission wavelengths complemented the trend observed in the absorption wavelengths of the materials indicating that the photo-emissions were oriented by the bandgap of the materials. Therefore, the incorporation of the chalcogenide anions resulted in an increase in the radius of the triiodide perovskite materials since bandgap is inversely related to the particle size. It can be further concluded that indeed the incorporation of the chalcogenide anions S and Se into the structure of the triiodide perovskite $\text{CH}_3\text{NH}_3\text{PbI}_3$ modulated its bandgap. However, the obtained bandgap; 3.40 eV for $\text{CH}_3\text{NH}_3\text{PbI}_3$, is bigger than the one reported in literature 1.57 eV for $\text{CH}_3\text{NH}_3\text{PbI}_3$ due to the fact that in this project the UV-vis and PL measurements were done with perovskite solution (perovskite precursor) and not with the annealed perovskite thin films (polycrystalline perovskite nanocrystals).

Electrochemical characterization by cyclic voltammetry was further conducted to probe the electrochemical behaviour and electronic properties of all the perovskite nanomaterials under investigation. The incorporation of chalcogenide anions (S and Se) resulted with a decrease in the energy of HOMOs from 3.89 eV ($\text{CH}_3\text{NH}_3\text{PbI}_3$) to 3.68 eV for S doped perovskite ($\text{CH}_3\text{NH}_3\text{PbI}_2\text{S}$) and from 3.89 eV to 3.56 eV for Se doped perovskite ($\text{CH}_3\text{NH}_3\text{PbI}_2\text{Se}$). This trend in the energy of HOMOs was expected due to the decreasing electronegativity of the anions; $\text{I} > \text{S}^{2-} > \text{Se}^{2-}$ implying that lesser energy is required to oxidise (knock out electrons from the valence band) the organo-chalcogenic perovskites and making them good candidates for solar cell application. An increase in energy of the LUMOs was also observed from 4.75 eV ($\text{CH}_3\text{NH}_3\text{PbI}_3$) to 4.96 eV for S doped perovskite ($\text{CH}_3\text{NH}_3\text{PbI}_2\text{S}$) and from 4.75 eV to 5.08 eV for Se doped perovskite ($\text{CH}_3\text{NH}_3\text{PbI}_2\text{Se}$). This also came as no surprise since I is the highest electronegative anion and therefore less energy will be required to reduce the triiodide perovskite $\text{CH}_3\text{NH}_3\text{PbI}_3$, whereas S^{2-} and Se^{2-} are the least electronegative anions and therefore more energy will be required to reduce the organo-chalcogenic perovskites. Opposite trends in electrochemical band gaps and optical bandgaps were observed. These trends were the results of the same structural changes induced by the incorporation of the chalcogenide anions into the triiodide perovskite structure. The successful incorporation of chalcogenides S^{2-} and Se^{2-} into the structure of the triiodide

perovskite was confirmed by cyclic voltammetry scans at cathodic peaks; 0.20V and 0.068V, respectively.

5.2 RECOMMENDATIONS AND SUGGESTED FUTURE WORK

Thin film samples of $\text{CH}_3\text{NH}_3\text{PbI}_3$, $\text{CH}_3\text{NH}_3\text{PbI}_2\text{S}$ and $\text{CH}_3\text{NH}_3\text{PbI}_2\text{Se}$ perovskite materials should be prepared on glass substrates (Fluorine doped Tin Oxide, FTO) and annealed at 100°C to form polycrystalline perovskite nanocrystals that will absorb and emit towards the near-infrared region of the solar spectrum. From thin films samples, X-ray Diffraction (XRD), Ultra Violet visible (UV-vis) spectroscopy & Photoluminescence (PL), High Resolution Scanning Electron Microscope (HR-SEM), High-Resolution Scanning Electron Microscopy (HR-SEM) and Atomic Force Microscopy (AFM) studies should be conducted to interrogate the structural, electronic and microscopic properties of the perovskite nanomaterials. The electrochemical properties and electrochemical performance should further be probed by cyclic voltammetry and electrochemical impedance (EIS) to determine the conductivity of all the perovskites under investigation.

For future work, the ratio between I_2 and the chalcogenides; S and Se, can be varied to determine the range of tuning the bandgap. Since Tellurium (Te) is the least electronegative chalcogenide anion Te (2.1), it can also be incorporated into the structure of the triiodide perovskite to form another new mixed ions perovskite $\text{CH}_3\text{NH}_3\text{PbI}_2\text{Te}$ to modulate the bandgap. Lastly, single-junction solar cells employing the perovskites under investigation should be fabricated and tested under simulated solar irradiation to investigate the effect of new organo-chalcogenic perovskites: $\text{CH}_3\text{NH}_3\text{PbI}_2\text{S}$, $\text{CH}_3\text{NH}_3\text{PbI}_2\text{Se}$ and $\text{CH}_3\text{NH}_3\text{PbI}_2\text{Te}$ on the photovoltaic parameters and eventually the photovoltaic performance.



UNIVERSITY *of the*
WESTERN CAPE



UNIVERSITY *of the*
WESTERN CAPE